SCUOLA DOTTORALE

EDEMOM
*European Doctorate in Electronic Materials,
Optoelectronics and Microsystems*

XXIII CICLO DEL CORSO DI DOTTORATO

Development and Characterization of Monocrystalline CVD Diamond Linear X-Ray Dosimeters

Dottorando	Ing. Daniele Maria Trucchi

A.A. 2010/2011

Tutor	Prof. Gennaro Conte
Coordinatore	Prof. Giuseppe Schirripa Spagnolo

Contents

Introduction

Several medical applications rely on the interaction between high-energy radiation and human tissue. Radiotherapy, radiography, and mammography need a very precise measurement of the radiation dose imparted to the target volume. These techniques differ in the radiation wavelength, but all require reliable, precise, and sensitive detectors to accurately calibrate the radiation sources and/or directly monitor the dose delivered to a patient.

The aim of this thesis is to prepare radiation-sensitive dosimeters that could be finally employed especially for radiotherapy applications, a sector that is currently under strong technological development. Radiotherapy as well as all the medical applications concerning interaction between a high-energy beam and human body need strict requirements about the beam monitoring dosimeters:

a) resistance to radiation damage;

b) tissue equivalence to avoid corrections on the dose actually absorbed by human tissue;

c) signal reproducibility and stability;

d) response proportional to the absorbed radiation dose-rate over a wide range of energies;

e) response proportional to the accumulated dose;

f) response independent of the radiation quantum energy;

g) response independent of temperature;

h) radiation sensitivity as high as possible;

i) small size.

Moreover, recent radiotherapy techniques as the intensity modulated radiotherapy (IMRT) employ time-pulsed beams with small spatial size that need fast-response detectors. The additional requirement for a compliant detector for this technique is thus:

j) Response times <0.1 s.

The reference dosimeters for this kind of applications are the ionization chamber for gas-detectors and silicon photodiode for solid-state detectors. Both have advantages and disadvantages. Ionization chamber provides a stable, reproducible and linear response to radiation dose-rate and

dose, but lacks in sensitivity and in scalability: it cannot be miniaturized owing to intrinsic technological limitations. Moreover, ionization chamber is a slow-response detector that cannot be used in IMRT applications. Silicon photodiodes have a high radiation sensitivity and is compliant to miniaturization, but they lack mainly in radiation damage resistance and tissue-equivalency. In fact, the signal produced by silicon photodiodes has to be corrected with procedures that could induce errors in evaluating the actual dose absorbed by a patient.

To tackle the described requirements, a possible alternative material has to be found. Diamond is the most suitable material for intense x-ray dosimetry, since it shows properties of tissue equivalence, radiation hardness and chemical inertness. Such characteristics imply no energy corrections with respect to human tissue and long operative lifetimes. X-ray detectors based on geological diamond are commercially available, but their use is limited by high-cost selection and calibration of stones with appropriate physical properties. Synthetic diamond produced by chemical vapour deposition (CVD) has the potential to overcome such limitations, ensuring minor production costs and reproducible physical properties. Many research groups reported results on polycrystalline diamond films as a radiation sensitive material, but problems of signal stability and material homogeneity hampered the transition from a research to a production level. Recent technological advances in CVD diamond homoepitaxy allowed single-crystal films to become a standard material, with physical properties even superior than natural diamond.

The scientific and technological challenge of this thesis is focused on the development of single-crystal CVD diamond dosimeters by preparing device structures able to comply a number as high as possible of the described requirements. In order to perform this, two commercial families of single-crystal diamond films are employed to develop x-ray dosimeters: optical-grade and electronic-grade samples. They differ in the physical properties and in the so-called electronic quality. Obviously they differ very sensibly in cost. Our aim is to qualify their properties which more relevantly influence their performance by means of our characterization techniques. The comprehension of the mechanisms at the basis of their operative function is fundamental to improve their performance. An experimental setup based on x-ray photoconductivity has been completely renewed and designed to provide the most accurate and detailed analysis of their response.

The main objective is to demonstrate that the dosimeters resulting from an appropriate device design combined with low defected crystals can be even commercially competitive.

Chapter 1

X-Ray Properties and Dosimetry

Chapter 1 is structured to give fundamental information about the nature and properties of x-rays, about the generators able to produce them and the methods to detect and measure their intensity and delivered dose.

1.1   Radiation dosimetry

The study and use of ionizing radiation in medicine started from three important discoveries: X rays by Wilhelm Roentgen in 1895, natural radioactivity by Henri Becquerel in 1896, and radium by Pierre and Marie Curie in 1898. Since then, the ionizing radiation gave rise to the development of radiology and radiotherapy as medical specializations and medical physics as a specialization of the physics. Right to the beginning the potential X-ray use in medicine for imaging and treatment of cancer was recognized [1]

Fig. 1. 1. One of the first radiography taken by Röntgen of Albert von Kölliker's hand at a public lecture (1896)[1].

The main difference between diagnostic and therapeutic procedures is the energy of ionizing radiation. The former involves relatively low energy x rays (*diagnostic radiology*) and gamma rays (*nuclear medicine*), while the second one exploits high energy x rays and gamma rays or high energy electrons (radiation therapy or radiation oncology or therapeutic radiology). We can divide the medical physics in four branches:

1. Diagnostic imaging with x rays (diagnostic radiology physics),

2. Diagnostic imaging with radio-nuclides (nuclear medicine physics),

3. Treatment of cancer with ionizing radiation (radiation oncology physics),

4. Study of radiation hazards and radiation protection (health physics).

Since the early 1900s most technological advances in medical use of ionizing radiation were related to improvements in radiotherapy. During the past two decades, most improvements in radiation medicine were due to radiotherapy developments. This dramatic development is related also to the advances of radiation dosimetry and treatment planning: from development of new absolute and relative dosimetry techniques to introduction of Monte Carlo techniques in dose distribution calculations[2].

Radiotherapy has become essential in the treatment of cancer and more than half of all cancer patients are nowadays treated by radiotherapy [2]. The first type of radioteraphy that was accepted in the second half of last century is the external beam radiotherapy, *ERTB*, in which an externally irradiation beam irradiates the patient body. The ERTB is successful at 81% and 86% for low risk cancer, between 20% and 60% for medium risk disease and between 19% and 25% for high risk cancer [4]-[5].

The main aim in radiotherapy is to deliver a maximum effective dose of radiation to a individuated tumour site without interact with the surrounding tissue. Radiation dose delivered to the target and surrounding tissues is thus one of the major predictors of radiotherapy treatment outcome. It is generally assumed that the dose must be accurately delivered within ±5% of the prescribed dose to ensure the treatment aims are met, while a variation from 5 to 19% to the target volume can lead to a significant change in the local tumour control and in the toxicity [6] . This constraints require a precise knowledge of the physical and dosimetric properties of the use ionizing beam.

In this frame the dosimetry plays a key role to reach this aim. Radiation dosimetry in radiotherapy is the calculation of the absorbed dose in tissue resulting from the exposure to directly

ionizing radiation. Before to proceed the radiation quantities an Units used in radiotherapy are shown in the following:

Exposure (C/kg)- is the ionization that the radiation would produce in air. It is defined as *dQ/dm*, where *dQ* is the sum of the electrical charges on all ions of one sign produced in air when all the electrons and positrons liberated by photons in a volume of air whose mass is *dm* are completely stopped in air.

Absorbed dose (Gy) – is the energy deposited in a small volume of matter (tissue) by the radiation beam passing through the matter divided by the mass of the matter. Absorbed dose is measured in terms of energy deposited per unit mass of material (J/kg). The quantity of 1 joule/kilogram has the special unit of gray (Gy) in the International System of quantities and units.

Equivalent dose (Sv) – in radiotherapy it is necessary to distinguish between the biological impact and the physical quantity of radiation because the different radiations do not have the same potential for producing biological change, even when the dose or energy delivered to the tissue is the same. The dose equivalent takes into account the relative biological impact of the radiation by including a radiation weighting factor (w_R). The radiation weighting factor is a dimensionless constant, the value of which depends on the type of radiation . The unit for the quantity equivalent dose is the sievert (Sv).

Radiation	Energy	w_R
γ-ray, X-ray, electrons, positron, muons,		1
Neutrons	< 10 keV	5
	10 keV - 100 keV	10
	100 keV - 2 MeV	20
	2 MeV - 20 MeV	10
	> 20 MeV	5
protons	>2MeV	2
alpha particles, nuclear fission products, heavy nuclei		20

Table 1. Weighting factors W_R for equivalent dose

Effective dose (Sv) - takes into account the specific exposed organs and areas of the body, since different organs are not equally sensitive to the possible adverse effects of radiation, such as cancer induction and mutations. It is calculated by multiplying the equivalent dose multiplying for the tissue-specific weighting factor for each organ or tissue type w_T. These products of equivalent dose and tissue weighting factor are then summed over all the irradiated organs to calculate the "effective dose." (Note that effective dose is a calculated, not measured quantity.)

A radiation dosimeter is a device capable of providing a measure of the average absorbed dose deposited in its sensitive volume by ionizing radiation. Different dosimeter exist depending if they directly measure the ionizing radiation (in.line configuration) or give the reading of the radiation after beam exposure (off-line configuration). The first type are for example ionization chambers and solid-state semiconductor devices, while passive thermoluminescence dosimeters (TLDs) and radiographic X-ray are detectors work off-line. The different mechanism of detection for these different devices will be shown in the following paragraphs.

For external beam radiotherapy, the most used dosimeters are the Silicon solid-state ones. They present in fact a higher sensitivity then the ionization chamber.

The first studies on diamond dosimeter applied to radiotherapy date at the beginning of 80s [7][8][9]. It is an almost tissue-equivalent material, since its atomic number is comparable to the effective atomic number of soft tissue (Z = 6). This is an important advantage over, for instance, silicon, as the diamond response is almost energy independent for a wide energy range of photons. Thus, no energy dependent factor has to be applied to the diamond response when used with different energies. There are many other advantages of using diamond detectors: diamond is not fragile and can be heat sterilized, it is highly biocompatible and can be used both as on-line and off-line dosimeter.

1.2   X-ray properties.

The electromagnetic radiation produced by the interaction of very fast electrons with matter and characterized by a kinetic energy ranging from about 1 keV to 1.2 MeV (wavelength approximately ranging from 1 and 10^{-3} nm) is defined as X-radiation. X-rays to about 12 keV (0.10 nm wavelength) are classified as "soft" X-rays, and from about 12 to 120 keV to as "hard" X-rays, due to their penetrating abilities. A large amount of the electrons kinetic energy is dissipated into heat and X-photons energy is necessarily lesser than the impinging electrons one. The radiation thus produced is composed by a continuous spectrum, named Bremsstrahlung (from the German

"braking radiation") and discrete lines, which frequency and wavelength are characteristic of the atomic element composing the target.
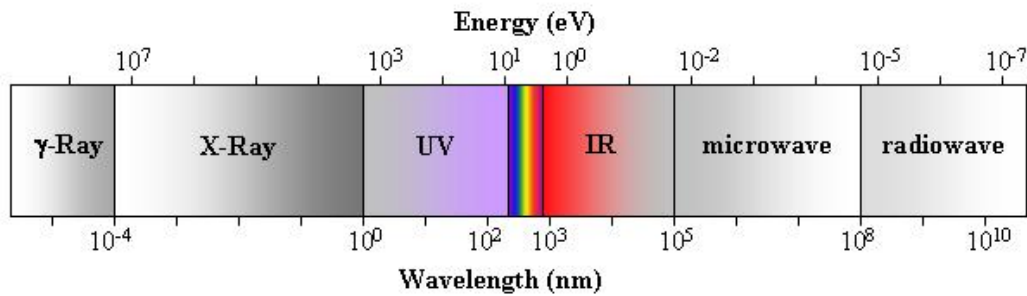

Fig. 1. 2. Electromagnetic Spectrum

X-rays were accidentally discovered by the German physicist W.C. Röntgen in 1895 during experiments on cathode beams. Although the vacuum tube in which the discharge was generated was covered by a black cloth, Röntgen observed fluorescence light coming from a barium platino-cianide plate casually situated close to the experiment. He hypothesized and verified that fluorescence was induced by a kind of unknown invisible radiation, more penetrating than UV. He named it X-radiation referring to its mysterious nature [10].

The immediate application of X-rays was correlated to the penetrating capability: radiography was developed by Röntgen himself.

At the state of the art, X- ray can be produced in different way. The main interesting sources are the following:

− A beam of electron that hits a target material causing the emission of a continuous spectrum (white spectrum) with discrete spectral lines characteristic of the target material. The X-ray tube at high vacuum, named Coolidge tube, is the most important source for crystallographic studies.

− Natural or artificial isotopes decay often produces emission of X-ray, named X-ray from radioactive source. This kind of radiation is often used to calibrate detectors.

− Synchrotron radiation source emitted by relativistic electrons travelling along curved path due to a magnetic field. The X-ray beam is the brightest source of X-ray, is highly collimated and linearly polarized.

− X-ray produced trough a plasma generated by hitting targets with high energy laser beam. This technique allows to efficiently produce soft X-rays.

For the purpose of this PhD thesis X-ray tube sources have been used with Cu and Mo targets, so only the description of the X-ray emission from a target hit by electrons will be treated in detail in the next paragraph.

1.2.1   X-ray source spectrum

The characteristic spectrum of a X-ray source depends on the radiative emissions of excited states of atomic electrons of matter Fig. 1. 4. In particular we are interesting to the effect of electrons impinging on a target that causes both the emission of spectral lines characteristic of the target material and the emission of a continuous spectrum of X-rays due to the deceleration of high velocity electrons when deflected by the atomic nucleus, Bremsstrahlung radiation. The resulting spectrum, in terms of intensity I vs. wavelength λ of the X-rays is shown in Fig. 1. 3.
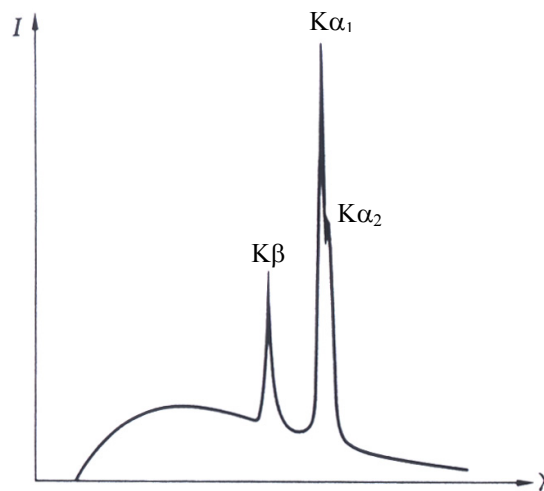
Fig. 1. 3. Generic emission spectrum of a X-ray source composed by characteristic lines superimposed on a continuous spectrum.

1.2.2   Characteristic X-ray lines

The impinging electrons can eject electrons from the inner shells of the atoms of the target. Those vacancies will be quickly filled by electrons dropping down from higher levels, emitting X-rays with sharply defined frequencies corresponding to the difference between the atomic energy levels of the target atoms.
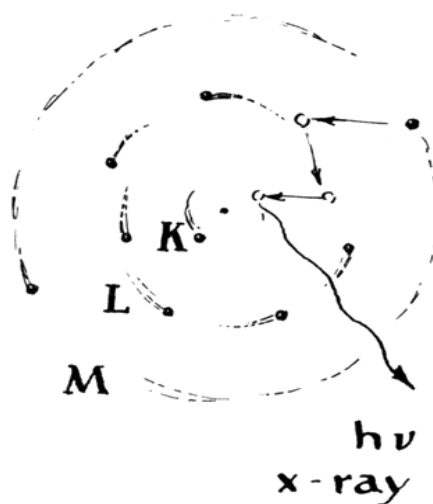
Fig. 1. 4. Scheme of a possible radiative emission mechanism from excited states of atomic electrons in material.

Two equivalent nomenclature exists to describe the lines of X-ray diagrams. The the IUPAC[1] notation, based on the initial and final states in X-ray transitions, and the Siegbahn one, based on the orbital level from which the atomic electrons is ejected and on the lines intensity [16].

X-ray levels are defined as those states which occur as initial and/or final states in X-ray transitions. Diagram levels are those which can be described by the removal of one electron from a closed-shell electron configuration. In Table 2 the relation between X-ray diagram levels and electron configurations is shown, while **Table 3** shows the correspondence between Siegbahn and IUPAC notation diagrams lines.

Table 2. Correspondence between X-ray diagram levels and electron configuration

| level	electron Configuration	level	electron Configuration	level	electron Configuration
K	$1s^{-1}$	N_1	$4s^{-1}$	O_1	$5s^{-1}$
L_1	$2s^{-1}$	N_2	$4p_{1/2}^{-1}$	O_2	$5p_{1/2}^{-1}$
L_2	$2p_{1/2}^{-1}$	N_3	$4p_{3/2}^{-1}$	O_3	$5p_{3/2}^{-1}$
L_3	$2p_{3/2}^{-1}$	N_4	$4d_{3/2}^{-1}$	O_4	$5d_{3/2}^{-1}$
M_1	$3s^{-1}$	N_5	$4d_{5/2}^{-1}$	O_5	$5d_{5/2}^{-1}$
M_2	$3p_{1/2}^{-1}$	N_6	$4f_{5/2}^{-1}$	O_6	$5f_{5/2}^{-1}$
M_3	$3p_{3/2}^{-1}$	N_7	$4f_{7/2}^{-1}$	O_7	$5f_{7/2}^{-1}$
M_4	$3d_{3/2}^{-1}$				
M_5	$3d_{5/2}^{-1}$				

The main rules to describe the X-ray emissions are the following. X-ray emission diagram lines are written with the initial and final X-ray levels separated by a hyphen. For examples:

---

[1] IUPAC is the acronym of International Union of Pure and Applied Chemistry. This IUPAC X-ray nomenclature has the advantage of being simple and easy to extend to any kind of transitions

K-L$_3$ (Kα_1 in the Siegbahn notation) denotes the filling of a 1s hole by a 2p$_{3/2}$ electron, i.e. the transition 2p $_{3/2}$ —> 1s.

In the case of unresolved lines, such as K-L$_2$ and K-L$_3$, the recommended IUPAC notation is KL$_{2,3}$

Siegbahn	IUPAC	Siegbahn	IUPAC	Siegbahn	IUPAC	Siegbahn	IUPAC
Kα_1	K-L$_3$	Lα_1	L$_3$-M$_5$	Lγ_1	L$_2$-N$_4$	Mα_1	M$_5$-N$_7$
Kα_2	K-L$_2$	Lα_2	L$_3$-M$_4$	Lγ_2	L$_1$-N$_2$	Mα_2	M$_5$-N$_6$
Kβ_1	K-M$_3$	Lβ_1	L$_2$-M$_4$	Lγ_3	L$_1$-N$_3$	Mβ	M$_4$-N$_6$
K$^{I}\beta_2$	K-N$_3$	Lβ_2	L$_3$-N$_5$	Lγ_4	L$_1$-O$_3$	Mγ	M$_3$-N$_5$
K$^{II}\beta_2$	K-N$_2$	Lβ_3	L$_1$-M$_3$	Lγ_4'	L$_1$-O$_2$	Mζ	M$_{4,5}$-N$_{2,3}$
Kβ_3	K-M$_2$	Lβ_4	L$_1$-M$_2$	Lγ_5	L$_2$-N$_1$		
K$^{I}\beta_4$	K-N$_5$	Lβ_5	L$_3$-O$_{4,5}$	Lγ_6	L$_2$-O$_4$		
K$^{II}\beta_4$	K-N$_4$	Lβ_6	L$_3$-N$_1$	Lγ_8	L$_2$-O$_1$		
Kβ_{4x}	K-N$_4$	Lβ_7	L$_3$-O$_1$	Lγ_8'	L$_2$-N$_{6(7)}$		
K$^{I}\beta_5$	K-M$_5$	Lβ_7'	L$_3$-N$_{6,7}$	Lη	L$_2$-M$_1$		
K$^{II}\beta_5$	K-M$_4$	Lβ_9	L$_1$-M$_5$	Ll	L$_3$-M$_1$		
		Lβ_{10}	L$_1$-M$_4$	Ls	L$_3$-M$_3$		
		Lβ_{15}	L$_3$-N$_4$	Lt	L$_3$-M$_2$		
		Lβ_{17}	L$_2$-M$_3$	Lu	L$_3$-N$_{6,7}$		
				Lv	L$_2$-N$_{6(7)}$		

Table 3. Correspondence between Siegbahn and IUPAC notation diagram lines

The intensity of the X-ray spectral lines depends on the fluorescence cross section (the probability of radiative decay of an excited state), on the penetration depth of the radiation into material and on the backscattered electrons number

The Bohr model of atoms [17] explains and calculates the frequency of the X-ray lines emitted from a transition from the state n_2 to n_1 for an atom Z

$$v_{1-2} = \frac{2\pi^2 m e^2}{h^3} Z^2 \left(\frac{1}{n_2^2} - \frac{1}{n_1^2} \right) \tag{1.1}$$

m is the electron mass, h the Heisenberg constant.

Following the Bohr model, Mosely empirically found a relationship between the frequency of a emission line, v_{1-2}, of a same series and the atomic number of material Z (1913):

$$\sqrt{v_{1-2}} = k_1 (Z - k_2) \tag{1.2}$$

where k$_1$ and k$_2$ are constant depending from the and k are constants depending on the type of X-ray line, K or L or M etc., Fig. 1. 5.
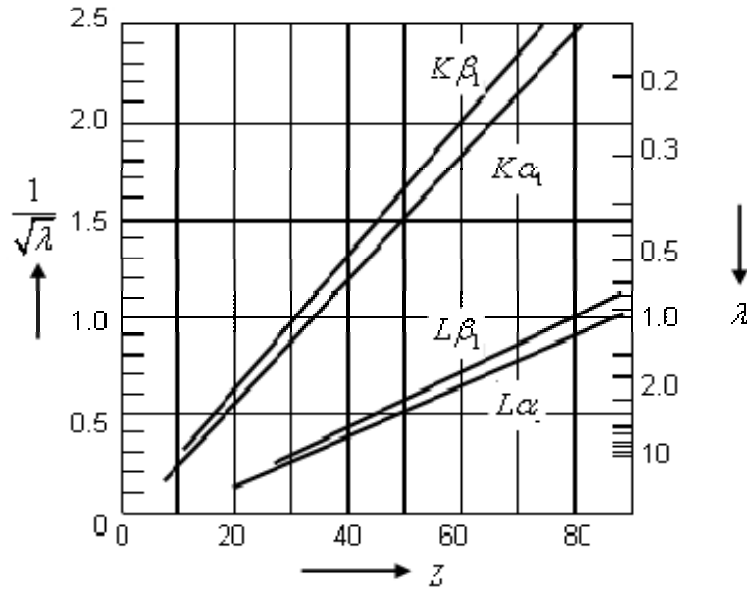
Fig. 1. 5. Empirical Mosely law showing the curve of characteristic line K and *L* as a function of the atomic number of material.

In 1968, Green and Cosslett measured the efficiency of production of characteristic X radiation for K, L and M lines using different target materials [19]. From their results the follow empirically law was found:

$$\frac{N_K}{4\pi} = \frac{N_0}{4\pi}(E_0 - E_K - 1)^{1.63} \qquad (1.3)$$

where $N_k/4\pi$ is the number of photon $K\alpha$ generated per steradiant and incident electron, N_0 depends on the target atomic number, E_0 is the electron incident energy in keV, and E_k is the excitation potential in keV. For a Cu target, that is the material used as source in this PhD thesis, Eq. (1.3) becomes:

$$\frac{N_K}{4\pi} = 1.8 \times 10^{-6}(E_0 - 8.9)^{1.63} \qquad (1.4)$$

To obtain the number of photon actually emitted from target at angle φ in respect to the surface for normal incident electrons, the used law is:

$$\frac{N_\varphi}{4\pi} = f(\chi)\frac{N}{4\pi} \quad , \quad \chi = \frac{\mu}{\rho}\frac{1}{\sin\varphi} \qquad (1.5)$$

where f(χ) is a correction terms depending on target material that decreases when the electron energy and the cosecant of φ.

1.2.3 Bremsstrahlung spectrum

The shape of the continuous spectrum produced by the deceleration of high velocity electrons when deflected by the atomic nucleus of the target can be described by the Kramers law [20]. It shows the intensity distribution as a function of the frequency of the emitted radiation:

$$I(v) = AZ(v_0 - v) + BZ^2 \qquad (1.6)$$

where Z is the atomic number of the target, A and B are constant and v_0 is the maximum frequency of the spectrum. Point out that the latter term of Eq. (1.6) can often be neglected since $B/A \sim$ 0.0025. Eq. (1.6) can be written as a function of the number of photon with a fixed energy E per incident electron dN_E:

$$dN_E = bZ(\frac{E_0}{E} - 1)dE \qquad (1.7)$$

with $b \approx 2 \times 10^{-9}$ eV^{-1} is named Kramers constant and E_0 is the maximum energy of the emitted X-ray that is equal to the energy of the electron impinging the target. From this equation the total energy of the Brehmsstrhlung spectrum and the efficiency of continuous radiation production, η_c are obtained:

$$\int_0^{E_0} EdN_E = bZ\frac{E_0^2}{2} \qquad (1.8)$$

$$\eta_c = bZ\frac{E_0}{2} \qquad (1.9)$$

1.2.4 X-ray treatment – filtering

For many application it is necessary to have a monochromatic source, therefore it is necessary the filtering of the spectrum of Fig. 1. 6a. The filtering is able to cut-off the continuous spectrum and lines, a single lines remain (usually the most energetically one) simulating a spectrum almost monochromatic and that can be represented as a Dirac Delta function. The counterpart is a decrease of the intensity. The filter is simply a layer of material with a minor absorption spectrum at wavelength higher then the lines of interest and that damps the lower ones.
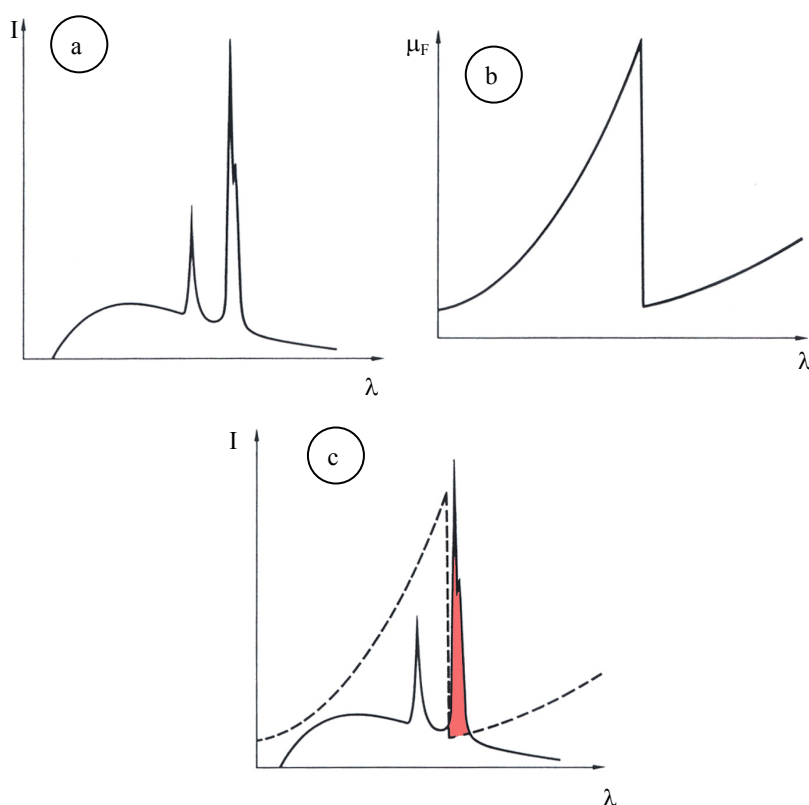
Fig. 1. 6. (a) characteristic spectrum of emission from a target hit by electrons. (b) absorption spectrum of the filter and (c) emission spectrum of the filtered X-ray source (the remaining peak is highlighted in red).

A suitable combination of two filter of different materials with different cut-off wavelengths allows o cut peak very close such as the $K\alpha_1$ and $K\alpha_1$. These filtering, named at balanced filters, does not attenuate the spectrum between the respective cut-off wavelengths very much. In Table 4, the most common materials composing the best filter for the most used targets are shown.

Target	$K\alpha$ line (nm)	Filter	Filter density (g cm^{-2})	Optimum thickness (mm)
Cr	0.22909	V	0.009	0.016
Fe	0.19373	Mn	0.012	0.016
Co	0.17902	Fe	0.014	0.018
Ni	0.16591	Co	0.014	0.013
Cu	0.15418	Ni	0.019	0.021
Mo	0.07107	Zr	0.069	0.108
Ag	0.05598	Pd	0.030	0.030

Table 4. Examples of the most common filters for typical target emitting X-rays.

1.3   X-ray sources

1.3.1   X-ray Tubes

The first prototype was a gas tube, the Crookes tube, that Roentgen used for his X-ray experiments in early 1900. It is a glass bulb filled with a gas at low pressure (10^{-1} - 10^{-2} Pa). A negatively charged cathode and a positively charged anode were located at opposite ends of tube. A third lobe hosts a third electrode, anticathode, that is connected to the anode, Fig. 1. 7. Applying an electric filed, the negative charged electrons travel toward the anode generating X-rays, by either *Bremsstrahlung* (continuous spectrum) or *fluorescence* (discrete lines), while few positive gas ions are attracted by the cathode at the opposite site. Usually the cathode is made of Al due to its low atomic number, to avoid damage from collision of positive ion; the anode is usually made of Pt or W [12] . The third anode is used to collect the positive ion and improve the vacuum. The electrons, or cathodic rays, during their travel can scatter gas atom not yet ionized and produce charged pair that contribute to the bombardment both anodes.
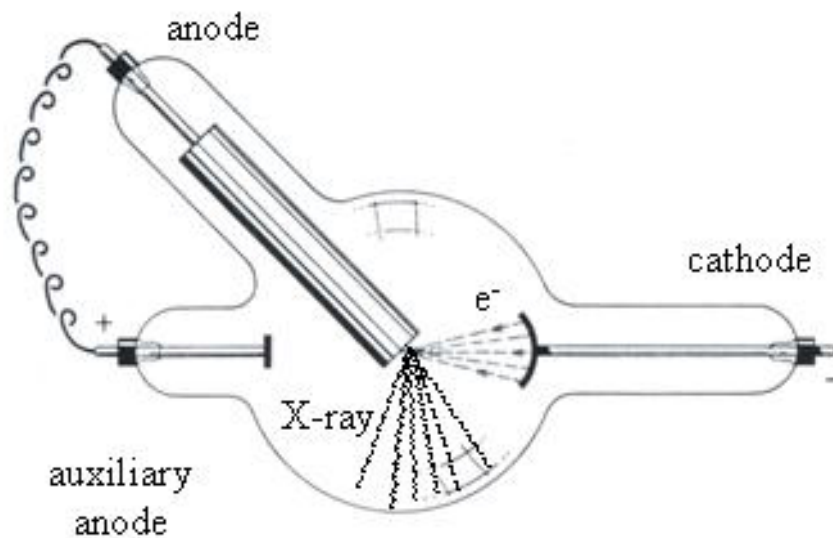
Fig. 1. 7. Scheme of the first gas tube for X-ray production.

Roentgen observed that higher atomic number of anode material produced higher X-ray intensity. The applied voltage difference determines the kinetics energy of cathodic rays that have to be able to ionize the larger fraction of noble gas. For this purpose also the pressure of gas is important. In fact if the pressure decrease, a lower number of collision occurs and the production of radiation is neither constant nor controllable; however if the pressure is too high, there is the possibility of damage of electrodes. Suitable values of gas pressure and DC voltage range between 10^{-1} e 10^{-2} Pa and between 5 e 50 kV respectively. The main inconvenience of the gas tubes is the difficulty to

obtain a constant value of production and to modulate it; the main advantages is its economical realization and use.

The evolution of the gas tube is the Coolidge tube, an high vacuum tube that is now the most common X-ray source (Fig. 1. 8). The improvement is a tungsten filament, heated by electrical current, used as cathode. The heating of filament enable the thermionic emission of electrons and control theirs kinetic energy. The emitted electron are accelerated toward the anode such as the gas tubes, but now their motion is controlled by the filament current instead of the gas collisions and eventual collisions harm the control of X ray production for this reason the vacuum inside the tube have to be at least 10^{-3} Pa. The filament temperature, depending almost only on the current flowing inside the filament, is the most important parameter for the process: at a certain temperature the maximum number of emitted electrons is fixed, so the voltage applied between anodes only increases the velocity of electrons as shown in Fig. 1. 9. This is a remarkable advantage of the Coolidge tube: the unique control parameter is the filament temperature, once it reaches the saturated zone of the current.
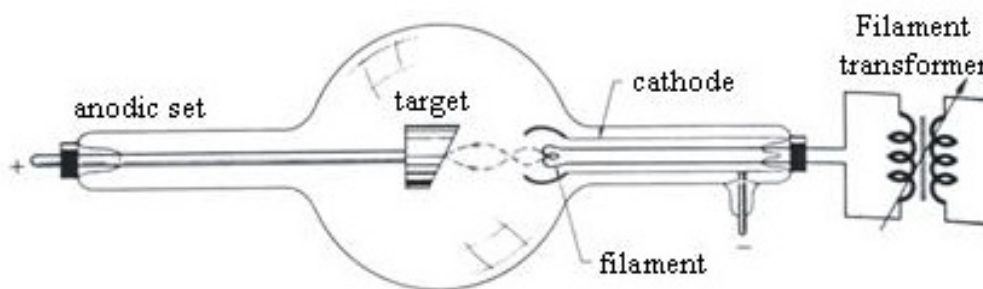
Fig. 1. 8. Scheme of the original Coolidge tube
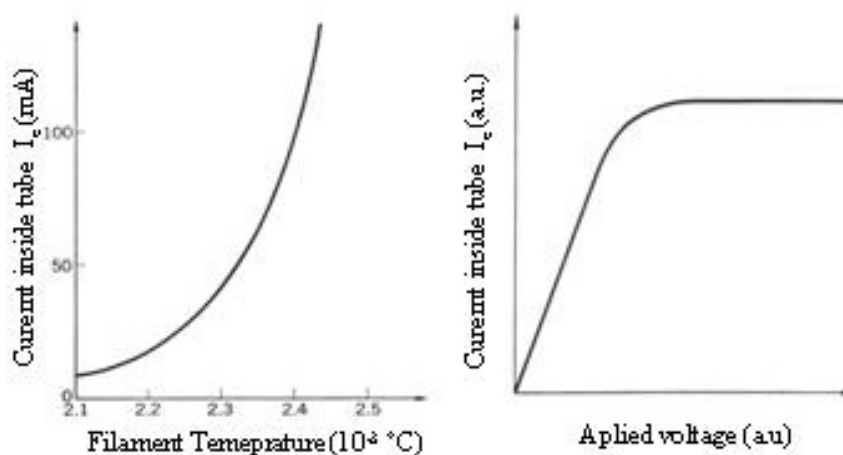
Fig. 1. 9. On the left, the electronic current inside the Coolidge tube I_e as a function of the filament temperature; on the right, I_e as a function of the voltage applied between the anodes. It is evident that the only parameter to control the process is the filament temperature.

The X-ray generation efficiency η at applied voltage ΔV, defined as the ratio between the X-ray energy and the electrons absorbed by target of Z atomic number, follow the empirical law :

$$\eta = 1.4 \times 10^{-9} Z \Delta V . \qquad\qquad (1.10)$$

The efficiency at standard operative condition is equal to few unit percentage and this implies that the remaining energy contributes to heat the target and to degrade it. For this reason in the modern tubes a cooling system for the target is foreseen.

In the modern commercial Coolidge tube the take-off angle is another important parameter because it influence the intensity of the X-ray (Fig. 1. 10). The aim of a Coolidge tube is the minimization of X-ray spot size (between 25 μm and 1 mm) and the maximization of its intensity and both this parameter are dependent on the take-off angle.
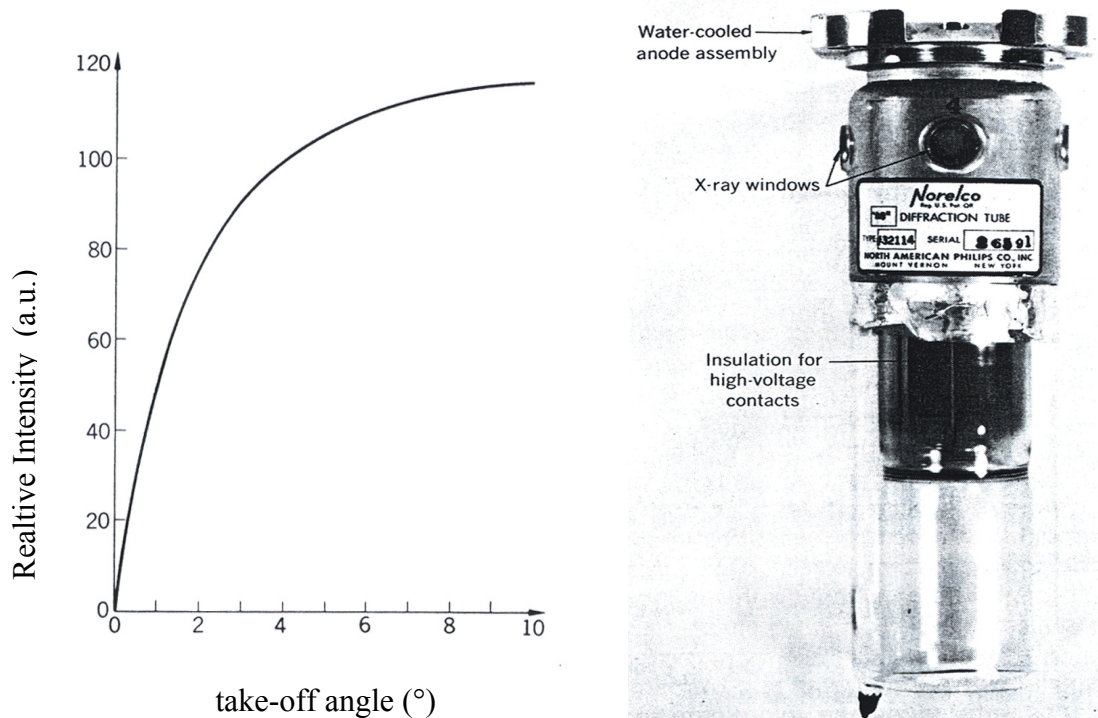
Fig. 1. 10. X-ray intensity curve as a function of the take-off angle. On the right an example of a commercial Coolidge tube.

The take-off angle is the angle at which he normal to anode is off perpendicular to the electron current so as to allow escape of some of the X-ray photons which are emitted essentially perpendicular to the direction of the electron current. the between the direction of cathodic ray and the normal to target surface. axis of the maximum intensity distribution of X-ray emitted from the

anode surface. The target surface is normal to the impinging electron beam, so that the take-off angle has to range between 2° e 10° to make the emitted radiation beam focused orthogonally.

The shape of the incident beam depends on the focal projection of the filament onto and the anode material. X-Ray beams that are parallel with wide projection of the filament have a focal shape of a line. X-Ray beams that are parallel with the narrow projection of the filament have an approximate focal shape of a square, which is usually labelled as a spot. These two focal projections are necessarily about 90 deg apart in the plane normal to the filament-anode axis. The X-ray beams emitted from the anode travel in a variety of angular directions from the anode surface. As the angle from the anode surface is increased, the intensity of the beam increases, but the spot also becomes less focused Fig. 1. 10. Thus take-off angles are typically selected in the 3 - 6 ° range on the bases of the need.

The X-ray generators based on Coolidge tube can be designed based on the necessity to have a time-constant or sinusoidal time-variable source. The semi-wave rectification uses the same tube as an ordinary diode; it is used for applications in which the source have to be intermittent, but it has the disadvantages of generating a heat surplus for long operative time and of having a reverse current that could damage the tube.

With a full-wave rectification a current with a frequency twice the semi-wave one is obtained, but the maximum current is decreased of a factor $\sqrt{2}$. A ripple circuit transforms the output into time-constant signal by introducing two capacities.

Fig. 1. 11. Different scheme of X-ray generators and relative coupled schemes: (a) semi-wave rectifying configuration, (b) full-wave, (c) at constant potential, and (d) relative current vs time trends.
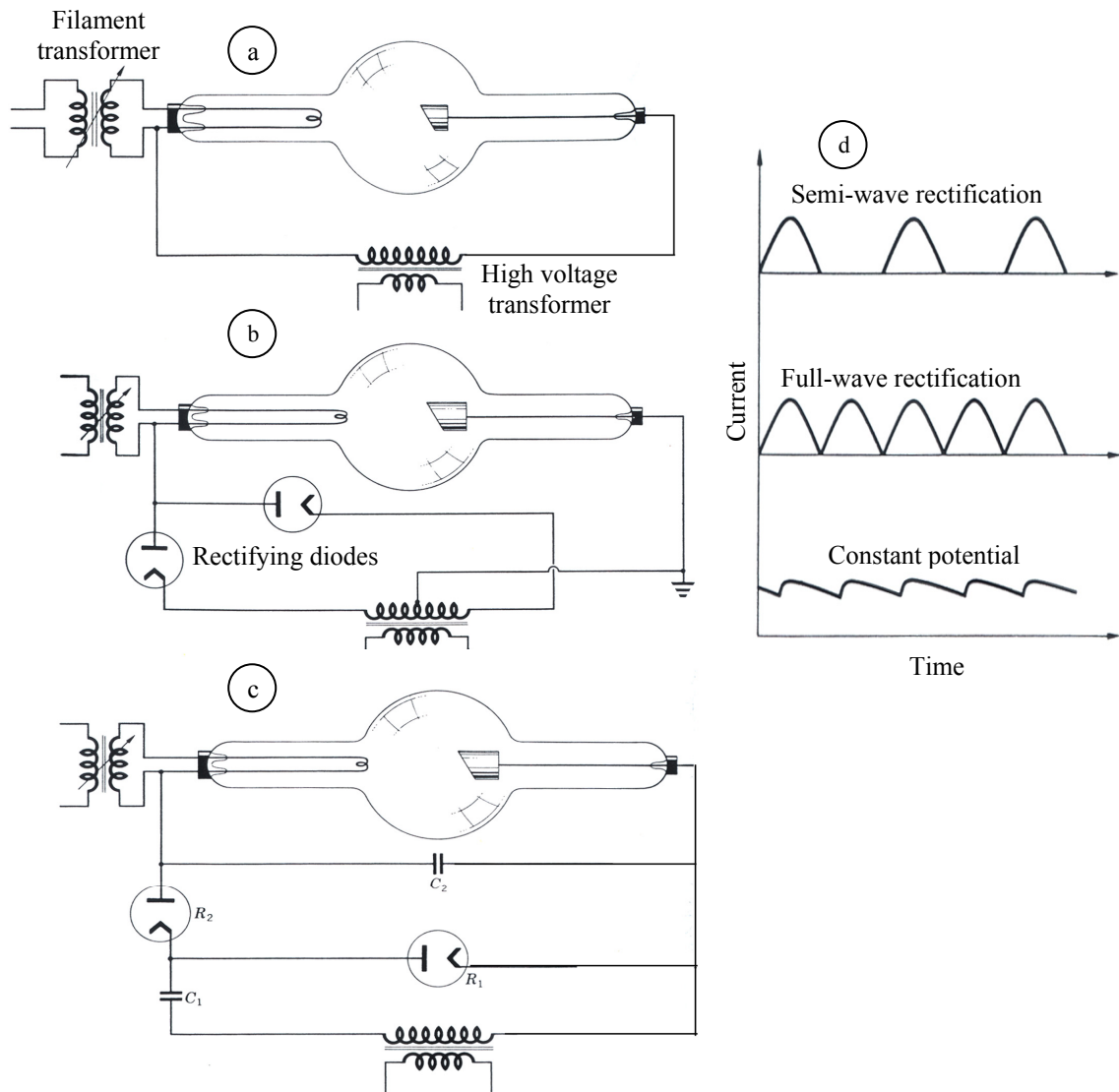
1.3.2 Radioactive sources

  The radioactive sources are excited nuclei, i.e. unstable atomic nuclei, that emit radiation when they attempt to become to reach a more stable state. Let's note that currently the difference between X and γ radiation derives from their origin: the first one is generated by external interactions to the atomic nucleus, the second ones are nuclear[2]. For these kind of sources we should talk about γ-rays, but for the purpose of this thesis we will continue to talk about X-ray for the emitted radiation up to 120 keV. The radioactive sources are used in diffractometry to calibrate X-ray detectors due to the fact that they are very time stable and in any case they have a well known decay velocity. An advantage of this source is the spectral purity of the emission. The radioactive nuclides, that completely decay own to an electron capture, are particularly useful because the emitted radiation almost monochromatic. In this kind of decay, the atomic number of the generated nucleus is of a unit less then the initial isotope and the emitted radiation is characteristic of the generated nucleus. Most of the emitted photons are characteristic of transition in 1s orbital, because the probability to capture an electron in different orbitals is very low. Table 5 shows the main radioactive isotopes, the species generated by the decay and the energy of the produced radiation.

Table 5. Main radioactive isotopes, the element generated by the decay and the energy of the produced radiation corresponding to the transition $2p_{3/2} \longrightarrow 1s$.

	X-rays	
Radioactive nuclide	Element	$K\alpha_1$ (keV)
^{37}Ar	Cl	2.622
^{51}Cr	V	4.952
^{55}Fe	Mn	5.898
^{71}Ge	Ga	9.251
^{103}Pd	Rh	20.214
^{109}Cd	Ag	22.16
^{125}I	Te	27.47
^{131}Cs	Xe	29.80

---

[2] In the past the definition of X and γ radiation was based on the wavelength, with the γ rays having the shorter wavelength. As shorter wavelength continuous spectrum "X-ray" sources such as linear accelerators and longer wavelength "γ ray" emitters were discovered, the wavelength bands largely overlapped

A useful source is composed by different radioactive isotopes and a target material to produce a continuous emitted spectrum that superimposes to the discrete lines of radioactive sources.

1.3.3 Synchrotron radiation

When a charged particle q of energy E and mass m is accelerated in a curving path or circular orbit of radius R at constant velocity v, emits radiation. When the charged particles are accelerated at very high speed by accelerators as synchrotron, the radiation is referred as synchroton radiation Fig. 1. 12.
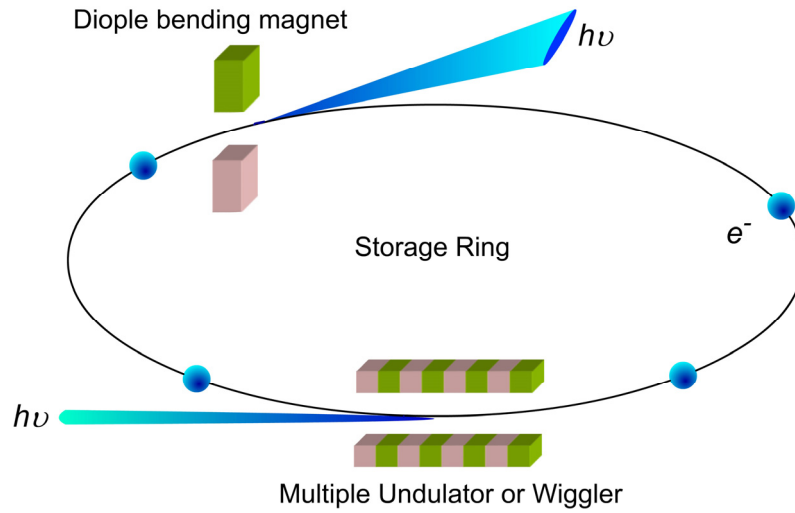
Fig. 1. 12. Schematic picture of a synchrotron radiation accelerator, hv indicates the emitted radiation and e− the charged particles (electrons).

The relativistic formula for radiated power P on the solid angle 4π is:

$$P = \frac{2q^2c(\frac{v}{c})^4(\frac{E}{mc^2})^4}{3R^2} \qquad (1.11)$$

where c is the light speed; replacing with the constant value, the irradiated power is:

$$P = \frac{0.0885E^4I}{R} \qquad (1.12)$$

where E is in GeV, I is the current in mA due to the charge particles and R is measured in meters.

The electromagnetic radiation is confined in a beam that is tangent to orbit with an aperture angle $\psi \approx (mc^2/E)$ (for energy of some GeV the aperture angle is about some tenth of a mrad), The

orbit of particle can be maintained only if the electromagnetic energy loss is balanced, usually by the application of a magnetic field.

The spectral distribution of the synchrotron radiation ranges from the infrared to X-rays. The parameter characteristic of a spectral distribution is the critical wavelength λ_c: half of the synchrotron radiation power is radiated by photons below the critical wavelength (Fig. 1. 13). The expression of critical wavelengths is:

$$\lambda_c = \frac{4}{3}\pi R\left(\frac{E}{mc^2}\right)^3 \qquad (1.13)$$

where E is in GeV, I is the current in mA due to the charge particles and R is in meter.
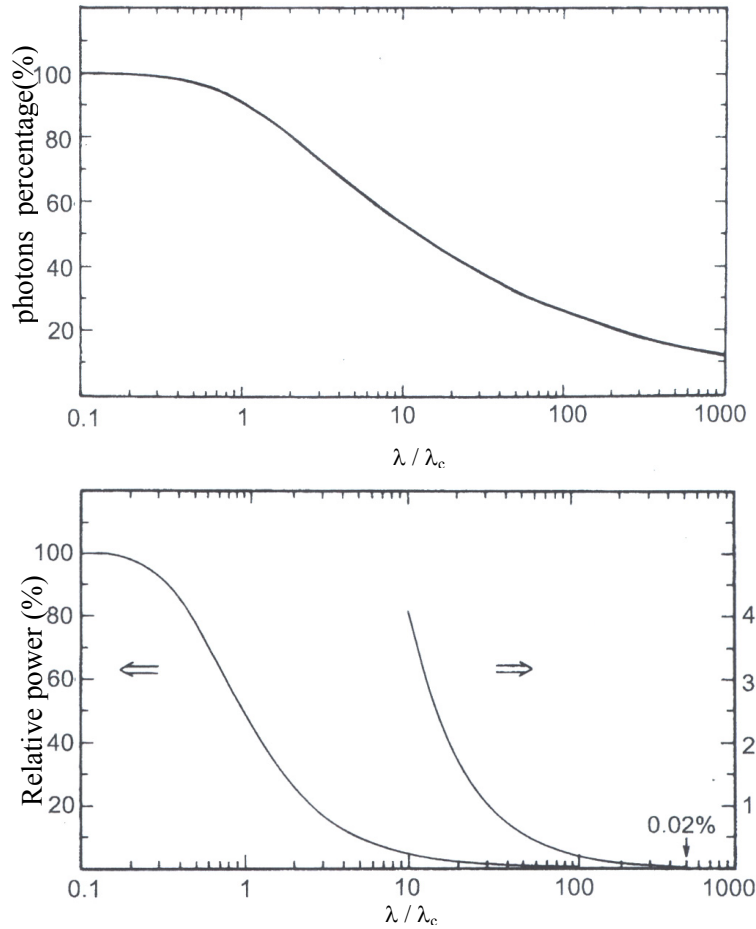
Fig. 1. 13. percentage of (a) emitted photon number and (b) radiated power as functions of λ/λ_c. Let's notice that the 50% of Power and only the 9% of photons are irradiated for wavelength less λ_c.

The unchallenged advantages of synchrotron radiation, that make it an ideal tool of matter properties investigation (from atoms to solid material to biology), are:

- very high density;
- a wide continuous spectral range;
- sharp angular collimation;
- limited transversal size of beam;
- high polarization;
- highly regular pulse;
- easy calculation of its properties.

1.3.4 Plasma Sources

The wavelength of the emission peak from a radiant black body falls in the ultraviolet range at about 10^5 K and in the X-ray region between 10^6 K e 10^7 K. At this temperature the matter is in its plasma phase, i.e. a gas made of highly ionized atoms and electrons at high energy. For the plasma to reach these temperatures a laser beam is used with an intensity at least of 10^{12} W mm^{-2}. The pulse duration has to be less then 1 ns to avoid the plasma to go off the beam. The emission spectrum shows lines group below the absorption energy characteristic of the 1s level and the intensity increases with the atomic number of the target Fig. 1. 14.
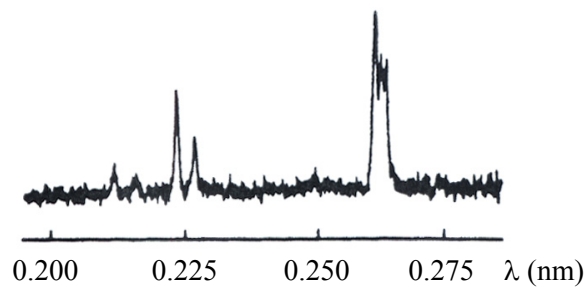
Fig. 1. 14. Spectrum of X-ray emission from a plasma obtained by a laser impinging on a Ti target.

1.4 X-ray detectors

In the X-ray history, the first detector was a screen covered by barium and platinum cyanide put close the Roentgen tube, that was the precursor of the X radiation photographic detector, used in crystallographic diffractometry up to day, but that show the disadvantage to be not stable. A different type of detector for this kind of radiation are gas detector, among which the ionization chamber, the proportional counter and the Geiger-Muller counter. At the opposite site there are crystal scintillators and solid-state detectors usually made of silicon.

1.4.1 Gas Detectors

When a X-ray beam pass though a gas, the photon can scatter the atoms of gas ionizing the gas and producing electron-ion couples. This kind of detectors are realized with a cylinder containing the gas and a metallic filament: between the filament and the cylinder a voltage difference is applied. Thus the charges of the generated couples are attracted by the opposite electrodes, with the difference that the ions having an higher mass are slower then electrons. The detection is based on the collection of the charges generated by the ionizing radiation. Three different type of gas detector exist differing for the voltage difference between the electrodes that gives rise to different phenomena inside the gas.

1.4.1.1 Ionization chamber

To understand the behavior of the ionization chamber, we highlight that the absorption efficiency increases with the atomic number Z of the gas. Moreover, increasing the atom density by controlling the pressure inside the chamber, the probability of interaction increases. Another fundamental parameter is the voltage difference applied between the metallic cylindrical cathode and the anodic filament: if it is zero or very low, the charges generated by a ionizing event can be recombine before reach the electrodes. If the voltage is sufficient high (100V), the charges are accelerating towards the respective electrode and produce a current that is proportional to the number of incident photons.

If the frequency of X photons is low, the detector is able measure the intensity of the X radiation and also to reveal the exciting signal in time. We notice that a X photon has energy more high then the energy necessary to generate a charged couple, thus if it is completely absorbed it

will produce *n* couple, where *n* is the ratio between its energy and the ionization energy of the gas. The intensity of the measured current strictly depends on the energy of the incident radiation.

1.4.1.2 Proportional counter

They can have different size and can contain different gases. A typical counter is made of a metallic cylinder, of diameter 2cm and length ranging between 8 to 10 cm, a central anodic filament and a lateral Berillium window of 0.13 mm thickness (Fig. 1. 15).
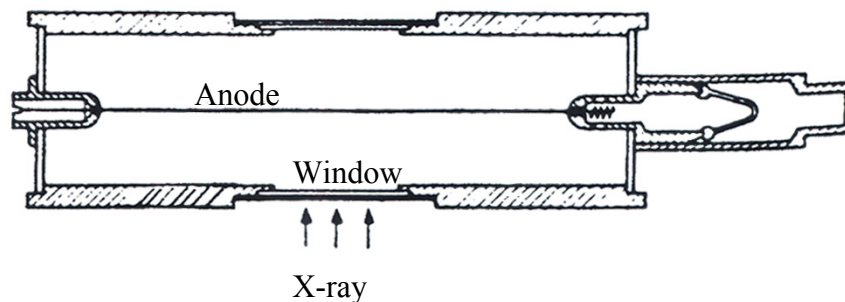
Fig. 1. 15. Schematic picture of a proportional counter.

The tube can be filled with Xenon at atmospheric pressure and with a small quantity of carbon dioxide or methane to avoid the discharges. When a X photon is absorbed, it generates an electron-hole pair that are accelerated by a voltage difference. If this voltage is high (> 300eV) the charge can create other couples giving rise to an avalanche phenomena. Thus the current is the sum of the charges created by photo-ionization amplified by a factor depending on gas and that is about 10^4 (for Xenon).

The number of charges reaching the anodes are equal to *A·n*, *A* is the amplification gas factor and *n* the number of generated couple per absorbed photon, from which the name of *proportional counter*. To increase the amplification factor some counters are filled at higher gas pressure.

1.4.1.3   Geiger-Muller counter

The Geiger-Muller counter is obsolete to detect the radiation, but it is useful like portable detector. In Fig. 1. 16 the scheme of the counter is shown: the cathode is a metallic cylinder usually made of chrome or iron of about 2 cm of diameter and 10cm of length; the anode is made of a tungsten filament of 0.7 diameter coaxial to the cylinder. The X-ray entry by the window whose material is not much absorbing, usually mica, with a thickness of about 0.013mm; the filling gas is usually Ar at 73 kPa or krypton at lwer pressure, with a little quantity of halogen species (0.4% of Cl or Br) to avoid damaging discharges. Between the anode and the window a space exist where the radiation is absorbed without contribute to detection.
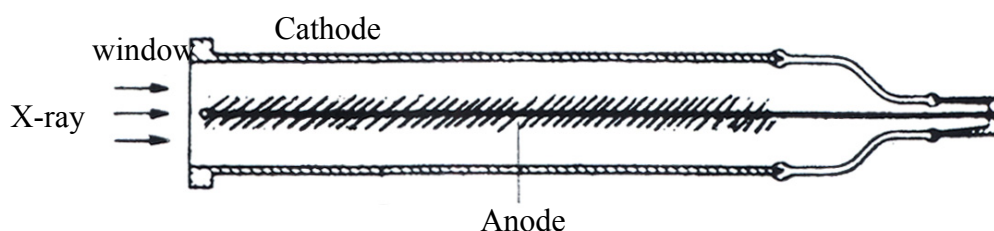
Fig. 1. 16. Schematic picture of a Geiger-Muller counter

The tube is not uniformly sensitive to radiation, but a radial distance from the filament dependence exists. The part of volume that is most sensible to radiation is close to the filament length ad shown in Fig. 1. 16, thus to have the maximum efficiency the photon should hit very close to the filament but not onto it.

The detection efficiency varies with the wavelength of incident radiation: for the Cu K line it is of about 50%, while for the Mo K line it is of 10%.

An advantage of the Geiger counters is that they do not critically depend on temperature, because the linear response is limited by the time between a ionizing phenomenon and the collection of carriers. Another positive characteristic is the simplicity of its use and the low degrade also after a long operation time.

The voltage difference between the electrode is about 1.6 kV, that allows only very speed collection transition: for this reason the width of the output pulse is almost constant varying the energy of the incident photon beam. Finally the Geiger counters are able to make a qualitative measure of radiation, without any quantitative information.

1.4.2   Solid-state Detectors

1.4.2.1   Scintillators

A scintillator counter is composed by two elements: a fluorescent crystal and a photomultiplier tube.
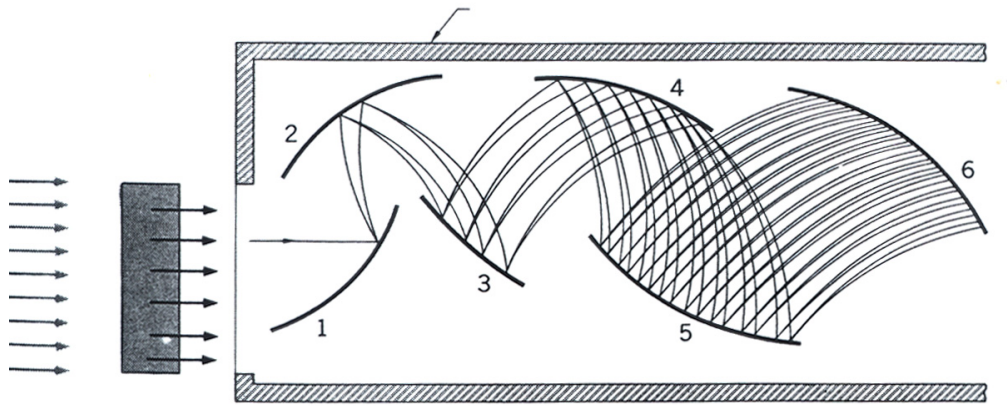
Fig. 1. 17. Schematic picture of a scintillator counter composed by a fluorescent crystal and a photomultiplier.

The crystal is usually a sodium iodide (NaI) and it is activated by a 1% of Thallium (Tl) concentration in solid phase. A beryllium window allows the passage of X-ray onto the sealed crystal; the back of crystal enclosure is made of glass to allow the visible light to pass, while a fluid with refraction index similar to the window glass separates the crystal from the photomultiplier to reduce reflection effect. To amplify the signal a classical photomultiplier with dynodes of high secondary emission coefficient is used. The crystal is the medium to transform the incident radiation in visible light [13].

1.4.2.2   Semiconductor based detectors

The solid-state detector exploit the increase of electrical conductivity of semiconductor or semi-insulator due to the irradiation: measuring the photocurrent is equivalent to estimate the incident beam intensity. The most used solid are cadmium sulfur or silicon, but with the great drawbacks of undergoing to radiation damage for energetically high beams and low sensitivity for X-ray. Dosimeter based on single crystal diamond is not affected by these defect own to its high radiation resistance and high optical band-gap that make it sensitive to wavelength less then UV. The intrinsic germanium detectors have an absorption higher then silicon, but they show a lower energy resolution and an higher interference among output peak.
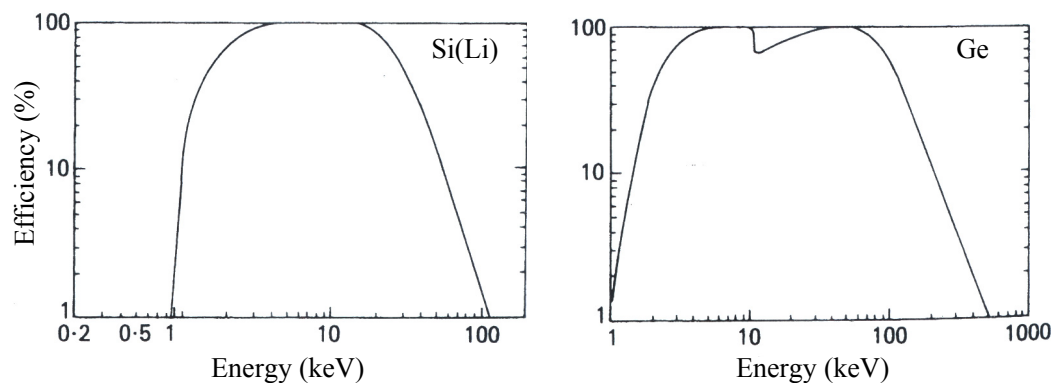
Fig. 1. 18. Efficiency of two common dosimeter based on semiconductor, Si on left and Ge on right.

1.4.2.3   Photodiodes.

The p-n silicon detectors have a wide application in dosimetry and they are well known to measure high energy electrons and photon beam. A lot of work has been performed to study their behaviour when exposed at different irradiation conditions. The main advantages in respect to the ionization chamber are:

-   high efficiency, due to the low ionization energy (for silicon W = 3.6 eV);

-   there is not necessary a bias;

-   good mechanical stability;

-   small variation of the ratio between the stopping force of silicon in respect to that of water in the required energy range;

-   High sensitivity for unit volume due to the high material density (for silicon: $\rho = 5 \times 10^{22}$ cm^{-3})

The high atomic sensitivity and the low ionization energy make the semiconductor about 18000 times more sensitive than an ionization chamber of the same volume filled with air. The disadvantage of the silicon detector are.

-   they are not tissue-equivalent, due its different atomic number, In particular the ionization sensitivity is different in respect to the water one when it is exposed at radiation $<10^2$ keV. In dosimetric application, this implies an alteration of the actual trend of the dose distribution in respect to depth.

-    The damages due to high energy radiation, such as proton, inside the detector induce a reduction of the effective ionization volume related to a sensitivity decrease.

31

1.5 Photon Energy Loss in Matter

A photon passing through the matter can interact with energy loss by different physical processes depending on the radiation energy $h\nu$ and on atomic number Z of material (Fig. 1. 19). At low energy ($h\nu$ < 100keV) and high Z the *photoelectric effect* prevails (Fig. 1. 20) and all the energy of the photon supplies the binding energy of an atomic electron to escapes from atom with a kinetics energy that, if it is larger then the work function, allow to escape from the material itself. Below 5 to 10 MeV the photon energy is larger then the binding energy of atomic electrons, the incident photon is deflected from its original path by an interaction with an atomic electron and this incoherent scattering process is dominant. This scattering of photons from charged particles was first observed by the physicist Arthur Compton in 1922, from which it takes its name *Compton scattering* [14]. When the incoming photon gives part of its energy to the electron, then the scattered photon has lower energy and according to the Planck relationship has lower frequency and longer wavelength. The wavelength change depends only upon the angle of scattering for a given target particle. Besides the Compton scattering, a coherent scattering occurs, the *Rayleigh scattering* due to the oscillation induced by the electromagnetic field of radiation (Fig. 1. 20).
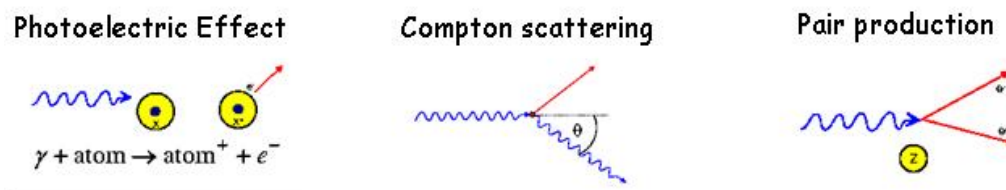
Fig. 1. 19. The different mechanisms of Photon Energy Loss in matter.

At higher photon energy a third process occurs: when the photon passes in the neighborough of an atomic nucleo an electron and a positron, the electron antiparticle of the same mass but opposite electrostatic charge, are created from the energy of the original photon. Due to the Einstein mass-energy equivalence (1905) the minimum energy for the pair production is 1.02MeV. The pair production is the dominant process for hν>>5MeV
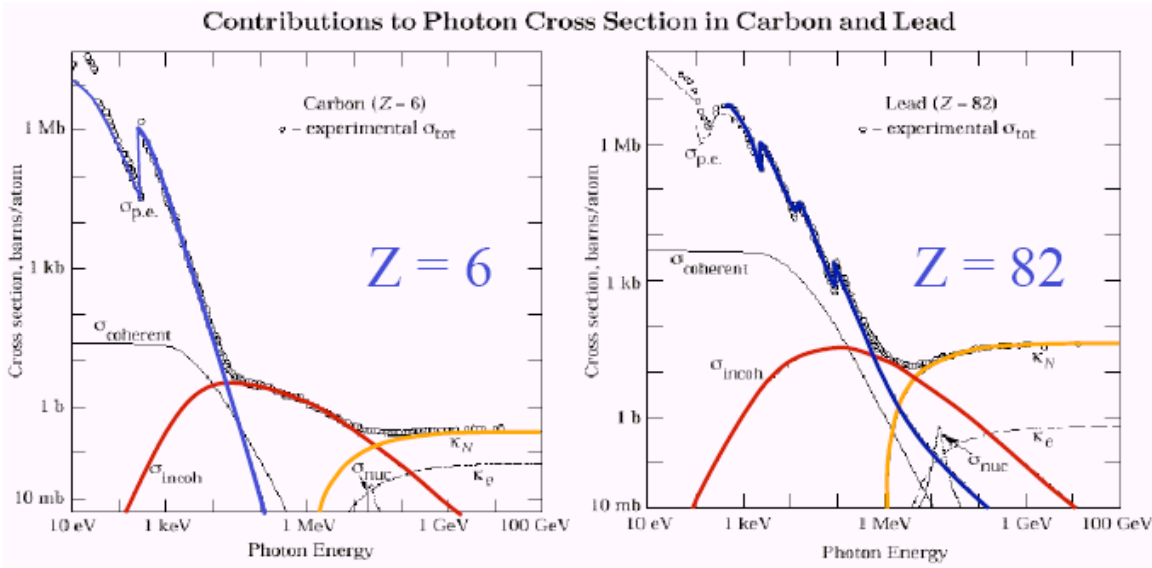
Fig. 1. 20. Total photon cross section in carbon, as a function of energy, showing the contributions of different processes: $\sigma_{p.e.}$, atomic photo-effect (electron ejection, photon absorption); $\sigma_{coherent}$, coherent scattering (Rayleigh scattering atom neither ionized nor excited); σ_{incoh}, incoherent scattering (Compton scattering off an electron); κ_n pair production, nuclear field; κ_e, pair production, electron field; σ_{nuc}, photonuclear absorption (nuclear absorption, usually followed by emission of a neutron or other particle). The explanation of the last two processes are omitted in the discussion.

Notwithstanding the complexity and the heterogeneity of the processes occurring when the radiation pass trough the matter, it is possible to describe the interection radiation-matter by the Classical Theory of the Electromagnetic radiation.

The intensity I of a monochromatic X-rays flux passing trough a material decreases by absorption and diffusion as a function of the material thickness, d, following the Lambert's law:

$$I = I_0 e^{-\mu_l d} \tag{1.14}$$

where I_0 is the initial intensity of radiation and μ_l is the absorption linear coefficient, which depends on the atomic number of material and on the incident radiation energy.

In fact, let's consider a section of infinitesimal thickness, dx, and unit surface (Fig. 1.21) of a material whose density is ρ and electron density is n so that the total number of electrons in the section of unit surface able to interact with radiation are $n\rho\, dx$. The intensity decrease dI due to the electrons interaction is:

$$dI = -I\sigma_e n\rho dV \tag{1.15}$$

where σ_e is the scattering coefficient; the negative sign imply the decrease of intensity as the radiation goes forward
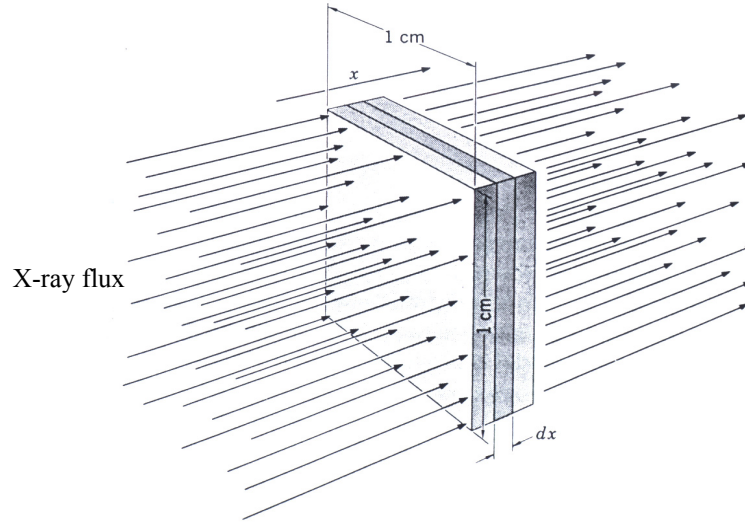
Fig. 1. 21

The radiation intensity at depth x will be obtained by integrating the (1.15):

$$I(x) = I_0 e^{-\sigma_m \rho x} = I_0 e^{-\mu_m x} \tag{1.16}$$

where I_0 is the initial intensity of the flux at the entry of material $(x=0)$, $\sigma_m = \sigma_e n$ is the mass scattering coefficient and $\mu_m = \sigma_m \rho$ the absorption coefficient due to the scattering. As described above, the energy loss in material is due to different processes so we can assume that the total absorption coefficient is the linear sum of different contributions:

$$\mu_l = \mu_m + \mu_C + \tau + \kappa \tag{1.17}$$

where μ_m is the contribution of coherent scattering, μ_C is due to the Compton scattering, τ the photoelectric one and finally κ is the contribution due to the pair production.

To obtain the Lambert law, Eq.s (1.14) and (1.17), we have made the fundament hypothesis of monochromatic radiation. For a polychromatic X-ray flux, Eq. (1.17) becomes an integral function on all the spectrum with a suitable weight for the different spectrum components.

References

[1] Landwehr, Gottfried (1997). Hasse, A. ed., *"Röntgen centennial: X-rays in Natural and Life Sciences"*. Singapore: World Scientific. pp. 7–8

[2] D. Sheikh-Bagheri and D. W. Rogers, Med. Phys. 29, 379 (2002)

[3] S. Webb S, P.M. Evans, Semin. Radiat. Oncol. 16, 193 (2006).

[4] A.A. Martinez, J.A. Gonzalez, A.K. Chung, et al, Cancer 88 425 (2000).

[5] G.K. Zagars, A. Pollack, A.C. von Eschenbach, Cancer 79 1370 (1997).

[6] Mijnheer BJ. *The clinical basis for dosimetric accuracy in radiotherapy. In: Radiation incidents.* British Institute of Radiology, 1996; London, UK. pp. 16-20.

[7] B. Planskoy, Phys. Med. Biol., 25, 519 (1980).

[8] E.A. Burgemeister Phys. Med. Biol., 26, 269 (1981).

[9] E.A. Burgemeister, W. Schouten, Radiat. Prot. Dosim., 6, 145 (1984).

[10] Röntgen, W. "Eine neue Art von Strahlen." Sitzungberichte der Physikalischen-medizinishen Gesellschaft zu Würzburg, 1985. - Translated, "On a New Kind of Rays" Nature 53, 274, 1896

[11] A. Eisntein, Annalen der Physik 17, 132–148, P. Lenard, Annalen der Physik 4, 149 (1902)

[12] W.Parrish, *X-Ray Analysis Papers,* Centrex Publishing Co.(The Netherlands, 1965)

[13] N.G.Alexandropoulos, Y.Amemiya, U.W.Arndt, B.Buras, Measurement of Intensities

[14] A. H. Compton, Phys. Rev. 21, 483; 22, 409 (1923)

[15] W.T.Sproull, *X-Rays in practice*, McGraw-Hill Book Company (New York, 1946)

[16] *Compendium of Analytical Nomenclature, Definitive Rules*, 1997 3rd ed., J. Inczedy, T. Lengyel, A. M. Ure, A. Gelencser, A. Hulanicki (Eds.), Blackwell Science, Oxford (1998).

[17] Niels Bohr, Philosophical Magazine 26 1 (1913)

[18] H. G. J. Moseley, M. A. Phil. Mag. (1913), p. 1024

[19] M Green and V E Cosslett J. Phys. D 1 425 (1968)

[20] H.A. Kramers, Phil. Mag. 46 836 (1923)

Chapter 2.

Physical Properties of CVD Diamond

2.1 Physical properties of diamond.

Diamond has been known for over two thousand years since its exceptional properties have been capturing the imagination of people since ancient times. Only in the 1950s it began to play an important role in the progress of technology in developed countries. It was diamond that brought a radically new level of performance to the mining industry and metallurgy. Attempts to use diamond in other areas had limited success. It was, however, generally recognized even at that time that diamond was among the most important strategic materials. With the rapid increase in the control of its synthesis, new possibilities have arisen to exploit its electrical and optical properties. Diamond has the widest electronic energy bandgap among the elemental semiconductors (5.47 eV), and one of the largest known energy gaps of all semiconductors. It has high diffusion energies for impurities and defects, and stable surfaces. The combination of light atomic mass and strong chemical bonding results in diamond having relatively high vibrational frequencies compared with other semiconductors.

Related to this, at room temperature and above, the capacity of diamond to conduct heat from an active area is unusually high. These properties should allow diamond to be used increasingly in a range of applications, from surface-mediated processes to high-power devices. Developments of the use of diamond require knowledge of a very wide range of properties. Some have been known for many years, such as the thermal expansion of diamond, which is required to make a heterogeneous structure of diamond and another material. Other properties have only been mapped out recently. For example, to obtain complete control of the lattice we need to know the effects not only of

impurities but also of the disorder from the isotope content of the lattice. In yet other areas, exploiting high speed (terahertz) or small dimensions (nanometre), there is still much to learn.

X-ray diffraction measurements on natural diamonds indicate that of tetrahedrally bonded carbon atoms (sp3) that crystallizes into the diamond lattice which is a variation of the face centered cubic structure the cube edge length a_0 of pure diamond, measured at room temperature with natural isotope content, is equal to 0.35671 nm. The actual value for a particular diamond will depend on its impurity level, its isotope content and its temperature.
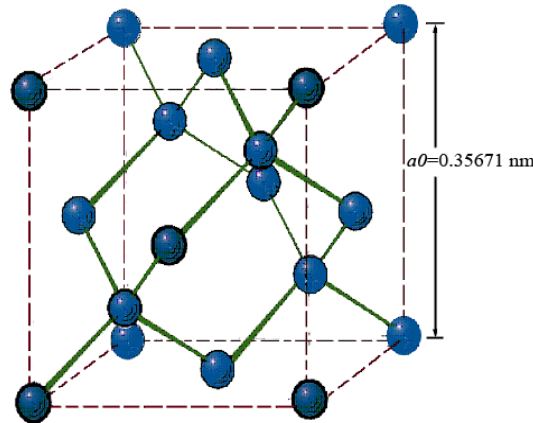
Fig. 2. 1. Diamond lattice structure.

Diamond is the appropriate material for electronics, optoelectronics, thermal management and mechanical applications owing to excellent physical and chemical properties as:

- Highest mechanical resistance among the solids.
- Highest thermal conductivity among the materials (about 2000 $W \cdot m^{-1} \cdot K^{-1}$, four and five times higher than silver and copper, respectively).
- Electrical insulator (resistivity for intrinsic diamond $>10^{14}$ $\Omega \cdot cm$ at room temperature) with wide-bandgap semiconducting properties.
- Broadband optical transparency covering the UV (up to the wavelength of 225 nm, corresponding to its bandgap of 5.47 eV), visible, infrared, terahertz and microwave spectral ranges.
- High chemical inertness even at high temperature (up to 700 °C in oxidizing atmosphere, > 1000 °C under vacuum, under inert and reducing atmospheres).
- The wide band gap of diamond combined with its radiation hardness and high break-down field is used to realize detectors for UV radiation (being 'solar blind'), nuclear radiation (n, α, β and γ) and high-energy elementary particles. The former are of particular importance for radiation dosimetry in medical applications since biological species, like diamond, contain mostly carbon

and other light elements; hence, the response of a diamond detector to radiation will resemble that of human tissue. The latter takes advantage of diamond's high radiation hardness, hence its resistance to high radiation fields as encountered in nuclear and particle physics experiments.

- Biocompatibility and human tissue-equivalent behaviour (atomic number 6 respect to 6.5).

- Negative electron affinity χ (down to -1.3 eV [1]) if hydrogen surface terminated, related to the capability of emitting electrons.

- The diamond surface when hydrogen-terminated exhibits low or negative electron affinity (NEA) leads to the possible emission of low-energy (cold) electrons and hence find application as material for cold cathodes and electron field emitters. When the H-terminated diamond surface is exposed to H2O (and some other specific molecules) 'transfer doping' may take place and a two-dimensional p-type layer is formed under the sample surface (few nanometers) [2]-[3] that can be exploited to develop surface devices (e.g. MESFETs and diodes).

- Capability to be designed as a function that diamond has to play. The morphological, electronic and chemical properties can be tailored, depending on the application, by controlling the deposition parameters.
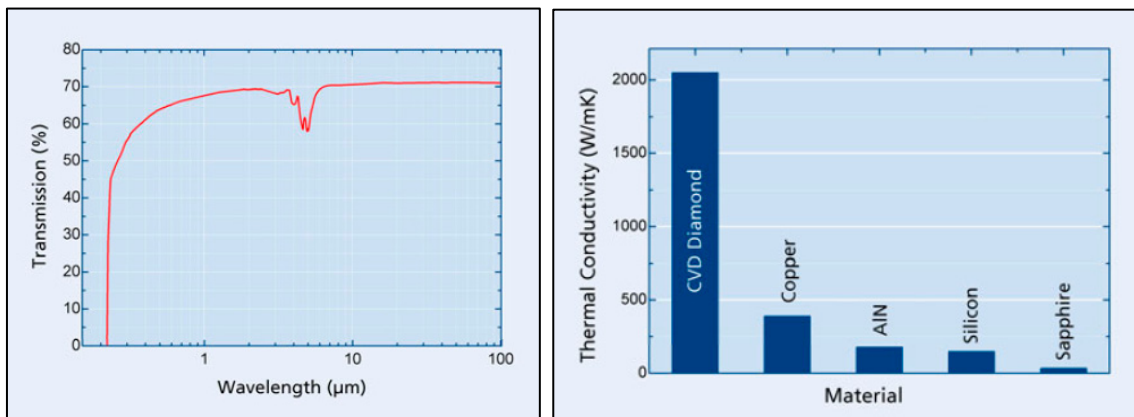
Fig. 2. 2. Transmission spectrum and thermal conductivity of diamond compared to other materials of interest.

Charge carriers exhibit very high mobilities in the single-crystal diamond. Diamond can be doped p-type (with boron, $E_a = 0.37$ eV) and n-type (with nitrogen, $E_a = 1.7$ eV and phosphor, $E_a = 0.56$ eV). All these donor and acceptor levels are rather deep; hence, the RT conductivities of doped diamond are low. Native defects in diamond such as vacancies, interstitials, extended defects and combinations of different chemical dopants (co-doping effects) as well as combinations of dopants and defects may also give rise to electronic levels in the diamond band gap. Even though doping with both acceptor and donor impurities has been achieved, the doping of diamond is still problematic.

Property	Diamond	Silicon Carbide			Silicon
		3C	4H	6H	
Atomic Number	6	~10	~10	~10	14
Lattice structure	fcc	fcc	hex	hex	Fcc
Atomic density (cm^{-3}) ***	1.77×10^{23}				
Density (g·cm^{-3})	3.52	3.21	3.21	3.21	2.33
Debye Temperature (K) ***	1860	1300	1200	1300	645
Vickers Hardness (kg·mm^{-2}) ***	10000				1100
Young's Modulus (GPa) ***	1050				150
Thermal Conductivity (W·m^{-1}·K^{-1}) ***	2200	360	370	490	112
Sound Velocity (m/s) ***	17500				8430
Band-Gap Energy (eV)	5.47	2.36	3.26	3.03	1.12
Intrinsic Electric Resistivity (Ω·cm)	10^{13}-10^{16}				3.2×10^5
Dielectric Constant (ε_r)	5.7	9.7	9.7	9.7	11.9
Breakdown Electric Field (V·cm^{-1})	10^7	4×10^6	4×10^6	4×10^6	3×10^5
Saturation Velocity (cm·s^{-1})	2.7×10^7	2.0×10^7	2.0×10^7	2.0×10^7	0.8×10^7
Electron Mobility (cm^2·V^{-1}·s^{-1})	2150	600	1000	500	1500
Hole Mobility (cm^2·V^{-1}·s^{-1})	1700	400	115	100	600
Ionization Energy (eV)	13	8.4	8.4	8.4	3.6
Energy to remove an atom from lattice (eV) ***	80	47	47	47	28
Relative lifetime under strong irradiation (a.u.) ***	~10^2	10	10	10	1

Table 2. I. Some physical parameters describing structural, phonon-related, electric and radiation-related properties for diamond, SiC and silicon. The symbol * indicates the highest value among all the solids.**

Table 2.I reports a comparison of the main physical properties among diamond and its strict relatives silicon carbide (in all its polymorph forms) and silicon, the reference material in electronics. Besides the highest Debye temperature, mechanical hardness among all the solid materials, diamond presents the peculiarity of being the most efficient thermal conductor and, if intrinsic or weakly doped, an electrical insulator at RT. This property rises a large amount of applications for thermal management, since, apart other ceramic materials (BN, AlN), which, in any case, are less efficient, is rare. This is due to the fact that thermal conductivity is always described by an electronic transport component a phonon transport component. The Fermi electron gas in metals makes predominant the electronic transport both for electrical and for thermal conduction, while phonon one is negligible. In diamond, the amount of free electrons is very low, whereas the phonon transport is the most efficient, resulting in the property described. Related to the phonon transport is the fastest propagation of sound in diamond, which makes it suitable for developing surface and bulk acoustic wave devices working at some GHz [4].

The wide bandgap of diamond causes a very high electric resistivity and allows very low leakage currents (in the order of pA or less depending on specific device structure). For detectors, this is a very important parameter that enables the possibility to develop simpler structures than p-n and Schottky junctions (i.e. development of photodiodes), as it occurs for silicon.

For application in high energy and intensity radiation beam monitoring, although it is less sensitive than silicon and silicon carbide (the energy to create an electron-hole couple is 13 eV against 8.4 and 3.6, respectively), it has a very high resistance to radiation damage, since the energy

2.2 Growth and doping.

The chemical vapour deposition (CVD) processes are the far cheaper production technique for synthetic diamond, allowing to grow it by activation of hydrogen and methane gases. Once activated, these gases provide the free radicals that chemically react among them and with the substrate. CVD allows the production of diamond in structure of films, a form compatible with electronic and opto-electronic applications. The only drawback of CVD production of diamond was that the resulting films had a polycrystalline structure (

Fig. 2. 3) if the deposition was performed on substrates made by other materials (e.g. silicon, silicon carbide, silicon nitride).
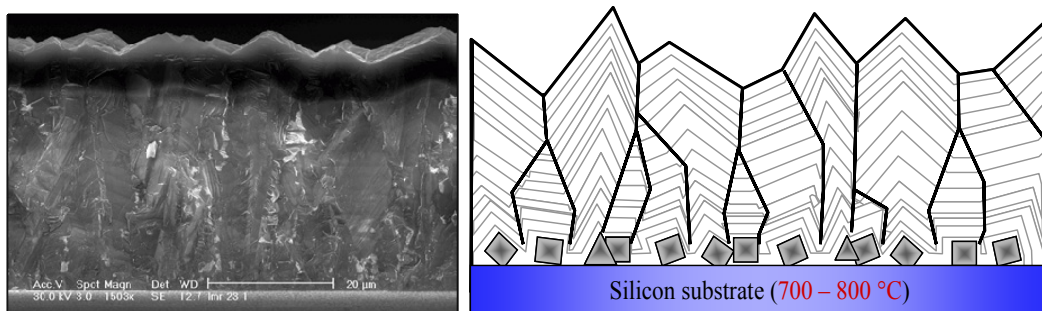
Fig. 2. 3

The polycrystalline structure takes rise from the film deposition dynamics: some nano-size diamond nuclei initially grow on the substrate becoming larger grains during the deposition (many of them are monocrystalline) [5]. When the grains are in contact, they are obliged to develop themselves along only one direction, perpendicular to substrate face [6]. Some grains are disfavoured with respect to others according to a preferential direction ruled by the flow direction of free radicals. The surviving grains become larger with increasing thickness (their lateral size is about twice the thickness), but the regions among them has included graphitic phases. These regions

are the grain-boundaries, which present very different electrical properties with respect to the high-quality diamond grains (graphitic behaviour against electrically insulating one). A control of the overall electrical properties has been developed [7] and is operated by the control of deposition properties, but, although it is statistically satisfying enough, the resulting material has not the desirable reproducibility and homogeneity, especially if compared to single-crystal standard semiconductors as silicon. However the advantage of polycrystalline diamond films can be deposited on very large areas to form for example optical windows (Fig. 2. 4).
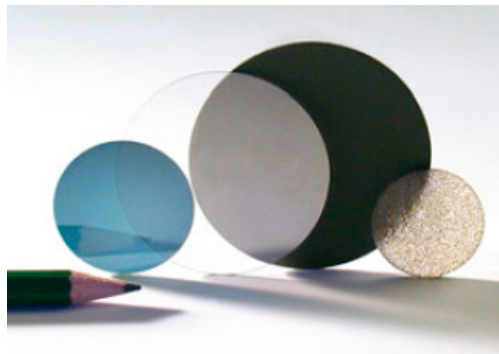
Fig. 2. 4

In this thesis, our attention will be uniquely focused on single-crystal diamond. In fact, during the early 2000s, a method for depositing single-crystal diamond films on high-pressure high-temperature (HPHT) substrates has been developed. It has allowed the development of single-crystals with very high quality, characterized by physical properties better than natural ones. Once finished the deposition process, the HPHT substrate can be separated chemically and/or by laser treatment and can be even reused for further depositions [8]. The unique drawback in single-crystal films is represented by a limited lateral size (1x1 cm^2 at maximum) caused by the small size of the substrate. The homoepitaxy by chemical vapour deposition is not different from heteroepitaxy, since the substrate, held at a temperature of 600 - 800 °C, is exposed to an ionized mixture of roughly 1% hydrocarbon and 99% hydrogen gases at pressures ranging from 40 to 80 Torr.

The role of mono-atomic hydrogen, derived from the activation of molecular hydrogen, is fundamental for diamond deposition, both in its polycrystalline and monocrystalline structure. Mono-atomic hydrogen has the function of etching the thermodynamically favoured graphitic phases and prevent the closure of surface bonding of the growing film in sp2 correlation, typical of graphite. The CVD diamond growth occurs under conditions of non-equilibrium that is usually described as the super-equilibrium operated by hydrogen.

The techniques to obtain CVD diamond under these metastable conditions are:

- Hot-filament assisted CVD (HF-CVD);

- Plasma assisted CVD (PA-CVD) at low (RF) or high (microwave) frequency;

- DC plasma jet (DC-PJ);

- Torch or flame technique;

- CVD assisted by laser or ion bombardment.

HF-CVD and PA-CVD induced by microwaves (MW-CVD) are the commonly used techniques, whereas the other cover a small niche only inside the research sector. HF-CVD is the technique more versatile and consists in activating the process gases by refractory metal filaments at temperatures of 2200 – 2400 °C. Its advantage is the process scalability, since it allows the deposition of homogeneous thickness films on large areas (even on wafers up to 12 inches). For this reason, it is mainly used for depositing polycrystalline diamond films.

MW-CVD is the standard technique to deposit industrially and at R&D level single-crystal diamond films because, although the deposition areas are limited, it is the most "clean" and most efficient technique. It is clean since it does not need other materials inside the reactor expect from process gases and, owing to the high power density, can reach deposition rates up to 100 μm/h.
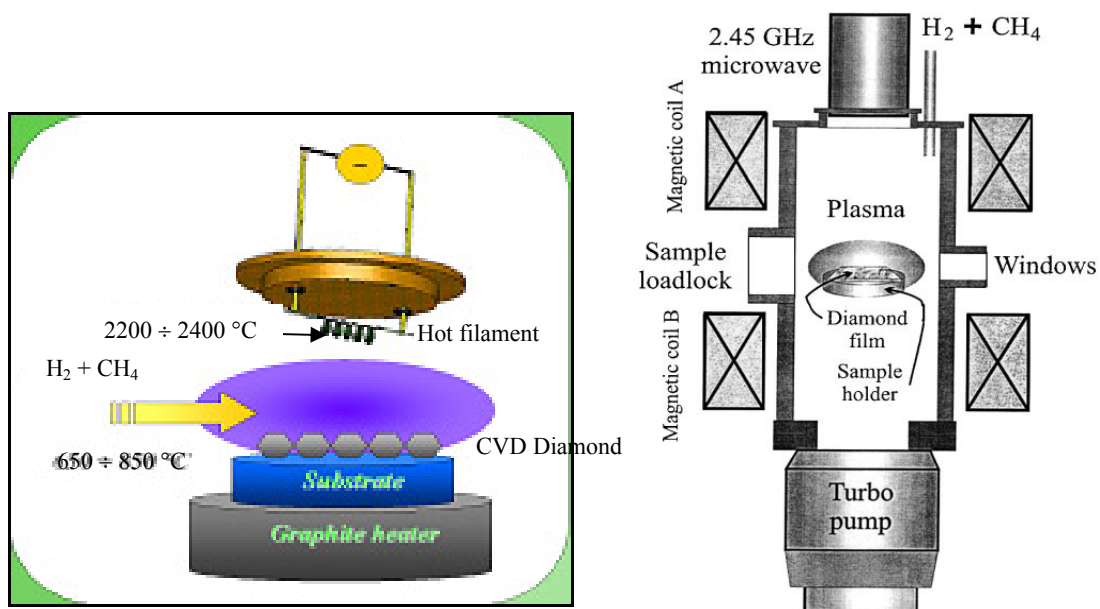

Fig. 2. 5. Left: HF-CVD reactor schematic drawing. Right: MW-CVD reactor schematic drawing.

2.3 Conductivity and carrier concentration

Diamond is a wide bandgap semiconductor, in which electrons in the conduction band and holes in the valence band are free to move under the influence of an applied electric field. Free charge carriers can be supplied by injection through a junction, produced by the radiation or induced through doping. The concentration and motion of charge carriers in diamond under an externally applied electric field determines the electrical conductivity.

The motion of carriers is not completely free, since they are constantly scattered by lattice vibrations and defects. The wide bandgap E_G of diamond (5.47 eV) induces a very low intrinsic carrier concentration at room temperature and consequently pure diamond is an excellent electrical insulator (the resistivity of intrinsic diamond may exceed 10^{16} Ω·cm [9]). In fact, in semiconductors the intrinsic carrier concentration n_i is an exponentially decreasing function of energy bandgap that can be described by:

$$n_i = (N_C N_V)^{1/2} e^{-\frac{E_G}{2kT}},\qquad\qquad(2.1)$$

where N_V and N_C are the effective density of states of valence and conduction band, respectively.

Diamond extrinsic semiconductivity can be obtained by doping. Boron is a small atom that well fits as a substitutional defect in the diamond lattice, made of small carbon atoms, and can successfully be introduced into the diamond lattice during the deposition processes. Boron is thus the most studied dopant in diamond and induces an extrinsic p-type conduction with an ionisation energy of 0.36 eV that can be observed at doping concentrations below 3 and 10^{19} atoms/cm^3. At very high boron concentrations the activation energy approaches zero and electric conduction becomes metallic. A room temperature resistivity of about 10^{-3} Ω·cm can be achieved for B concentrations above 10^{21} cm^{-3}.

Diamond extrinsic n-type conductivity can be obtained by doping with phosphorus and nitrogen. Dopants in wide-band-gap semiconductors have a tendency to have higher ionisation energies than in narrow-band-gap semiconductors. In diamond this results in low activation with respect to thermal energy at room temperature (~26 meV). Phosphorus has an ionisation energy of about 0.57 eV whereas nitrogen of 1.7 eV [10]. In literature, it was reported a possible shallow n-dopant consisting in boron coupled with deuterium [11], but this attempt was not followed by other confirmations.

The lack of known shallow donors for diamond has led some researchers to conclude that its prospects for use in electronics are limited. Although this is partially true but, on the other hand, the extreme physical properties of diamond expand the capability in other directions. Conventional device structures cannot automatically be exported to diamond technology. A more creative approach and the necessity of developing new structures of devices that exploit the material

advantages of diamond are required. Generally in these kinds of devices the charge carriers are provided from highly doped regions, whereas the active regions consist of intrinsic diamond.
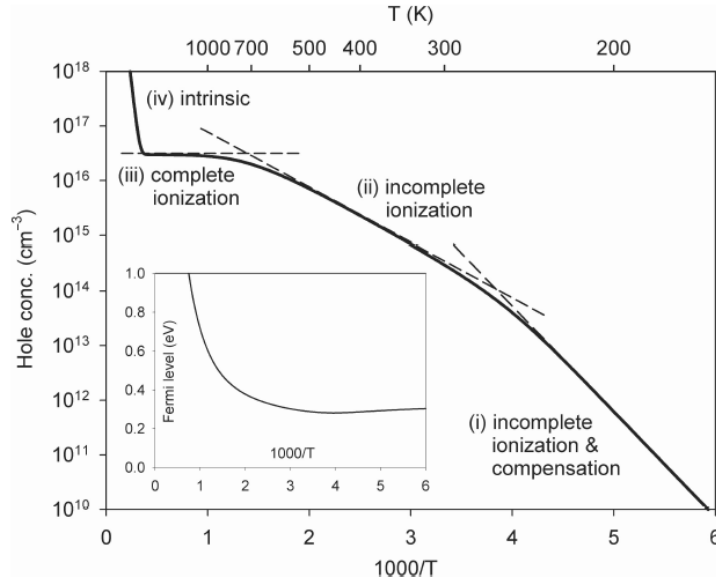
Fig. 2. 6. Hole concentration as a function of temperature [9].

At low electric fields the conductivity σ is proportional to the hole concentration p in a p-type semiconductor:

$$\sigma = q\mu_p p \,, \tag{2.2}$$

where q is the elementary charge and μ_p is the drift mobility for holes. Diamond is a crystal with cubic symmetry, therefore conductivity and mobility are always isotropic. Conductivity is consequently a scalar value. If both acceptors and compensating donors are present with concentrations N_A and N_D, respectively, and with $N_A > N_D$, then, in a non-degenerate semiconductor, the hole concentration p can be calculated from:

$$\frac{p(p+N_D)-n_i^2}{N_A-N_D-p-n_i^2/p} = \frac{N_V}{g_a} e^{-\frac{E_A}{kT}} \tag{2.3}$$

where E_A is the acceptor ionisation energy, k the Boltzmann constant, T the absolute temperature, and g_a the spin degeneracy factor equal to $4+2\exp(-\Delta/kT)$, with Δ=13 meV [12]. In Fig. 2.1 the curve describing the hole concentration in boron-doped diamond with a deep compensating donor (e.g. nitrogen) is shown, that is a specific characteristic of each semiconductor material. The carrier concentration exhibits four qualitatively different behaviours as a function of temperature:

i.   At very low temperatures when $p \ll N_D$, $p \ll N_A - N_D$ and $p \gg n_i$, the acceptor is incompletely ionised and the compensating donor is only partially ionised. Eq. (2.3) reduces to:

$$p = \frac{N_A-N_D}{N_D} \cdot \frac{N_V}{g_a} e^{-\frac{E_A}{kT}} \,. \tag{2.4}$$

44

ii.   From room temperature up to 600 K, $>> p >> N_D$ and $p >> n_i$, the acceptor is still incompletely ionised but the donor is fully ionised. In this case Eq. (2.3) yields to:

$$p = \left[(N_A - N_D) \frac{N_V}{g_a} \right]^{1/2} e^{-\frac{E_A}{2kT}} \qquad (2.5)$$

This is the case involving most of the applications, which work at room temperature.

iii.   For higher temperatures, above 1000 K, where $E_A >> kT$ and $p >> n_i$, a complete ionisation of the acceptor occurs. In this region the carrier concentration is independent of temperature:

$$p = N_A - N_D \qquad (2.6)$$

This operative region is shifted around room temperature for devices made from standard semiconductors (Si, GaAs, etc.).

iv.   The intrinsic carrier concentration is predominant so that $p \approx n_i$, thus

$$p = (N_C N_V)^{1/2} e^{-\frac{E_G}{2kT}} . \qquad (2.7)$$

It is evident that standard device technology can be exported to diamond only for high temperature applications. The amount of boron activation at room temperature is plotted in Fig. 2. 7, which shows the hole concentration for different acceptor and compensating donor concentrations. If the boron concentration is increased above 10^{19} cm^{-3} the insulator–metal transition is approached, consequently the activation increases rapidly almost to completion.
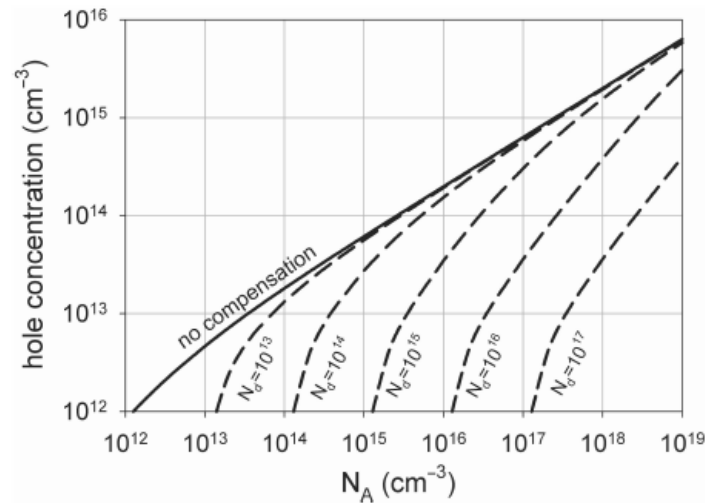

Fig. 2. 7. Hole concentration as a function of doping level [9].

2.4 Charge carriers mobility and lifetime.

Important performance parameters for active semiconductor materials in detectors are the carrier mobility μ and lifetime τ. At low electric fields, μ is a constant. For natural diamond, this value is equal to (2150 ± 200) and (1700 ± 280) $cm^2 \cdot V^{-1} \cdot s^{-1}$ for electrons and hole, respectively (see Table 2. I). In single-crystal CVD diamond films that in this thesis will be named optical-grade samples, these values were found to be equal to 1714 and 2064 $cm^2 \cdot V^{-1} \cdot s^{-1}$, with hole mobility larger than electron one [13]. A work in literature [14] suggests the values of 4800 and 3800 for electrons and holes, respectively, but such values have not been confirmed during successive measurements. Recently, on most recent electronic-grade single-crystal diamond films hole mobility was found to be (2430 ± 45) against (2145 ± 30) $cm^2 \cdot V^{-1} \cdot s^{-1}$ of electrons [15, 16].

We have to remember that the mobility is equal to the ratio between carriers drift velocity v_{drift} and electric field E. In diamond, at electric fields $> 10^4$ V/cm, the mobility becomes a function of electric field due to interaction with phonons and the carriers drift velocity tend to saturate to a defined value. Its dependence on electric field can be described as:

$$v_{drift} = \frac{\mu_0 E}{1 + \dfrac{\mu_0 E}{v_s}}, \qquad (2.8)$$

where μ_0 is the low-field mobility and v_s the carriers saturation velocity, equal to about 10^7 cm/s both fro electrons and holes.

Apart from the mobility temperature dependence, less interesting for applications involving detectors operative at room-temperature, it is interesting to observe that the mobility can be also a function of the charge carriers density produced by photo-excitation. This dependence is due to the electron-hole scattering, that becomes not negligible if charge density is high. It can be described as

$$\mu \propto \frac{T^{3/2}}{(np)^{1/2} \ln \left(1 + \dfrac{\alpha T^2}{(np)^{1/3}}\right)}, \qquad (2.9)$$

where n and p are the produced electrons and hole photogenerated, respectively. T is the temperature and α a constant. The charge injection has to be $> 10^{16}$ cm^{-3}, typical of very high radiation intensities, to induce a decrease of mobility by electron-hole scattering Fig. 2. 8.
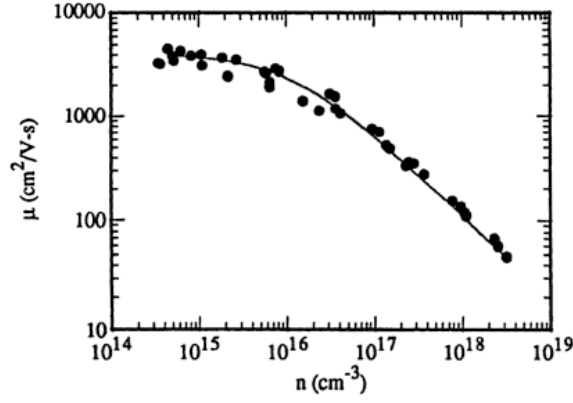
Fig. 2. 8

The other important parameter is the carriers lifetime τ, which ranges from 10^{-11} to 10^{-8} s and is governed by the nitrogen concentration if it exceeds 10^{19} cm^{-3}. In detectors, to achieve full charge collection and high counting efficiency for pulsed radiation sources, the condition $d \geq \delta = \mu E \tau$ should be fulfilled [17], where d is the distance between the detector contacts (usually it coincides to film thickness for thin-films) and δ the carriers mean free path due to the applied electric field. The charge collection efficiency η can be defined as:

$$\eta = \frac{\delta}{d} = \frac{\mu \tau E}{d}, \eta \leq 1. \tag{2.10}$$

If μ is equal to about 2×10^3 cm$^2 \cdot$V$^{-1} \cdot$s^{-1}, τ is equal to 10^{-8} s and the electric field before drift velocity saturation is about 10^4 V/cm, the optimal distance between the contacts is minor than 2 mm for obtaining a charge collection efficiency close to 100%. In this thesis, all the samples are designed according to a sandwich structure, thus d is the film thickness. Samples' thickness is about 500 μm, consequently, if there are not other effects not considered here, we should be able to approach this condition.

2.5 Surface conductivity. Hydrogenation.

Since Bandis and Pate [18] discovered the surface conductivity of hydrogen-terminated diamond and a related negative electron affinity (NEA) behaviour, a lot of attention was focused on the applicability of these effects in electronics [10], [19, 20]. Many experiments have been performed to optimize the hydrogen surface coverage mainly on diamond natural crystals or homoepitaxial grown CVD crystals; however, the origin of this conductivity is still debated and the process still to be optimized. However, hydrogen termination of diamond surfaces opened new perspectives because it mainly induces:

47

- NEA property. It means that electrons located at the bottom of the conduction band, and sufficiently close to the surface, have no potential barrier for their escape into vacuum. Consequently, NEA diamond surface is related to an efficient electron emission, giving rise to applications of diamond as a cold cathode.

- A surface conductivity orders of magnitude higher than the one of oxidized surface even for intrinsic diamond (resistivity may reach values down up to 10^{-6} Ω·cm against 10^{16} Ω·cm of diamond bulk). Such conductivity is induced by the formation of a bi-dimensional hole gas, that can be exploited to realize surface electronic devices as Metal-Semiconductor Field Effect Transistors (MESFETs) [21, 22].

- A work function matching, that can be employed for fabricating ohmic contacts with metals that on oxidized diamond produced a rectifying junction.
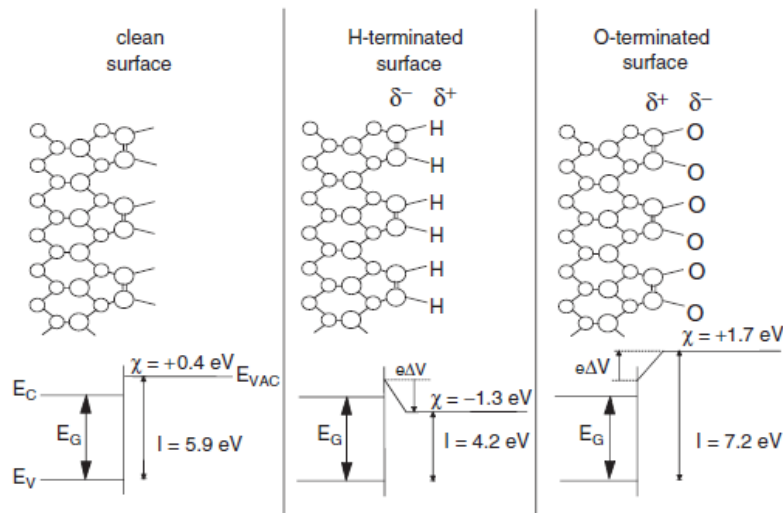
Fig. 2. 9. Electron affinity variation as a function of diamond surface termination [23].

As described, NEA means that the vacuum level E_{VAC} is energetically below the conduction band minimum E_C and thus the electron affinity $\chi = E_{VAC} - E_C < 0$, which is an opposite behaviour to almost all other semiconductors for which > 0. In Fig. 2. 9 a brief sketch of how surface chemical termination induces a different electron affinity value on diamond clean, hydrogen-terminated and oxygen-terminated surface. NEA behaviour becomes PEA (positive electron affinity) in all the other cases than hydrogenation. In **Fig. 2. 10**, the effect of NEA is denoted by the photoelectron yield onset at 5.5 eV. It means that photons with an energy just equal to the diamond bandgap are able to excite electrons that can escape towards the vacuum. This enlarges the energy spectrum of a possible photo-induced cold cathode and allows to achieve very high values of photo-emission yield.
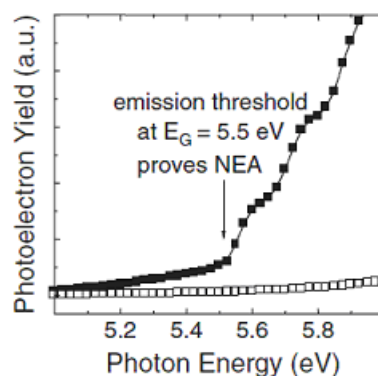
Fig. 2. 10. Photo-emission yield of diamond with NEA property [23].

Diamond work function can then be engineered. This can be performed not only according to the three discussed cases which give a discrete number of possible electron affinity value, but a tunable work function engineering is possible if a different hydrogen coverage is obtained. In other words, the χ value can be controlled if a control of the number of chemically bonded hydrogen atoms on diamond is performed. **Fig. 2. 11** shows the dependence of electron affinity on hydrogen coverage. This variation in the experiment [24] is obtained, on the contrary, by inducing a progressive hydrogen desorption caused by temperature. The minimum achievable value for χ actually is around -1.5 eV.
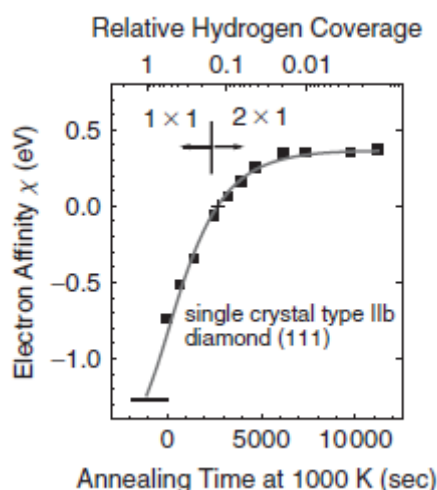
Fig. 2. 11. Electron affinity variation as a function of surface hydrogen coverage [23].

Hydrogen termination is generally and more efficiently performed in a MW-CVD reactor, in which the molecular hydrogen is made monoatomic and thus highly reactive. The process occurs at high substrate temperatures (600 – 800 °C), at pressure ranging from 20 to 80 Torr, and at high hydrogen fluxes (200 – 500 sccm). The singularity is that the surface conductivity cannot be explicitly measured since the mechanism needs the presence of hydroxyl adsorbates on diamond

surface. Until this does not occur, there is not the formation of a dipole that induce the bi-dimensional hole gas under the surface. In literature the currently accepted model for this surface conductivity is the so-called "transfer doping mechanism", in which ions on the diamond surface play the role of effective acceptors [25]. The surface conductivity sensibly changes after 1 hour in air and reaches its saturation value after 3 days (**Fig. 2. 12**).
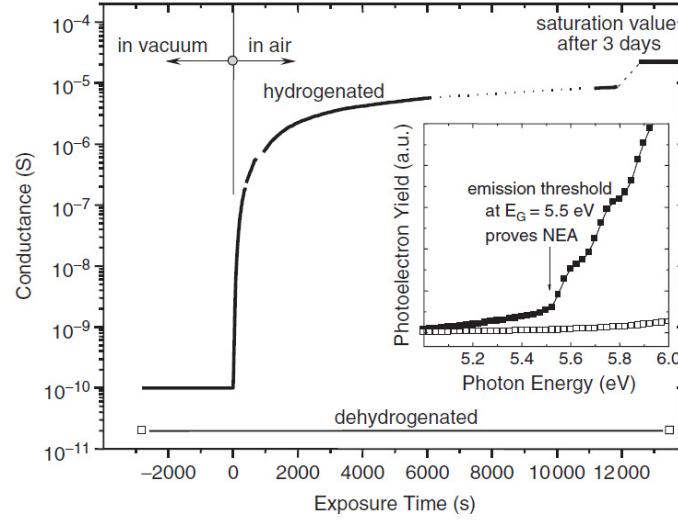
Fig. 2. 12

As discussed, the hole gas is confined just under the surface. Its depth in the diamond bulk is a function of carriers density, but it was estimated to few nanometres (see **Fig. 2. 13** [2]). The mobility μ shows a variation among different samples from 30 to 70 cm$^2\cdot$V$^{-1}\cdot$s^{-1}. But it is well-known that the mobility is not only a function of sample electronic quality but also of carrier concentration: the lower the concentration the higher is μ. The highest room-temperature mobility measured is for homoepitaxial C layers oriented along the (100) direction and amounts to 335 cm$^2\cdot$V$^{-1}\cdot$s^{-1} for a carrier surface concentration of 7×10^{11} cm^{-2} [20].
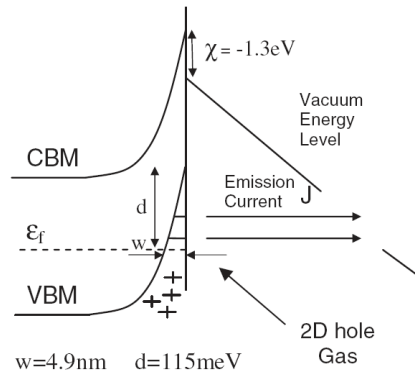
Fig. 2. 13

References.

1. Maier, F., J. Ristein, and L. Ley, *Electron affinity of plasma-hydrogenated and chemically oxidized diamond (100) surfaces.* Physical Review B, 2001. **64**(16).
2. Gan, L., et al., *Quantization of 2D Hole Gas in Conductive Hydrogenated Diamond Surfaces Observed by Electron Field Emission.* Physical Review Letters, 2006. **96**(19).
3. Strobel, P., et al., *Surface transfer doping of diamond.* Nature, 2004. **430**(6998): p. 439-441.
4. Benetti, M., et al., *Gigahertz-range electro-acoustic devices based on pseudo- surface-acoustic waves in AlN/diamond/Si structures.* Applied Physics Letters, 2005. **87**(3): p. 033504.
5. Zhang, J., *Modeling and visualization of polycrystalline thin film growth.* Computational Materials Science, 2004.
6. P., A., E. Cappelli, and F. Pinzari, *Nearest-neighbor distance distribution of diamond nuclei on substrate surfaces.* Applied Physics Letters, 1997. **70**(13): p. 1697-1699.
7. Trucchi, D., et al., *The influence of grain-boundaries on the electronic performance of CVD diamond films.* Diamond and Related Materials, 2005. **14**(3-7): p. 575-579.
8. Lee, S.T. and Y. Lifshitz, *The road to diamond wafers.* Nature, 2003. **424**: p. 500-501.
9. Isberg, J., *Transport Properties of Electrons and Holes in Diamond*, in *CVD Diamond for Electronic Devices and Sensors*, R.S. Sussman, Editor 2009, John Wiley & Sons Ltd.: London. p. 29-48.
10. Kalish, R., *Diamond as a unique high-tech electronic material: difficulties and prospects.* Journal of Physics D: Applied Physics, 2007. **40**(20): p. 6467-6478.
11. Teukam, Z., et al., *Shallow donors with high n-type electrical conductivity in homoepitaxial deuterated boron-doped diamond layers.* Nature Materials, 2003. **2**(7): p. 482-486.
12. Willatzen, M., M. Cardona, and N.E. Christensen, *Linear muffin-tin-orbital and k*p calculations of effective masses and band structure of semiconducting diamond.* Physical Review B, 1994. **50**: p. 18054-18059.
13. Pernegger, H., et al., *Charge-carrier properties in synthetic single-crystal diamond measured with the transient-current technique.* Journal of Applied Physics, 2005. **97**(7): p. 073704.
14. Isberg, J., et al., *High Carrier Mobility in Single-Crystal Plasma-Deposited Diamond.* Science, 2002. **297**(5587): p. 1670-1672.
15. Galbiati, A., et al., *Performance of Monocrystalline Diamond Radiation Detectors Fabricated Using TiW, Cr/Au and a Novel Ohmic DLC/Pt/Au Electrical Contact.* IEEE Transactions on Nuclear Science, 2009. **56**(4): p. 1863-1864.
16. Duenas, J.A. and I. Martel, *Timing properties of thin SC-CVD diamond detectors*, 2009.
17. Altukhov, A.A., et al., *Application of Diamond in High Technology.* Inorganic Materials, 2004. **40**(Suppl. 1): p. S50-S70.
18. Bandis, C. and B.B. Pate, *Simultaneous field emission and photoemission from diamond.* Applied Physics Letters, 1996. **69**(3): p. 366-368.
19. Kawarada, H., *Hydrogen-terminated diamond surfaces and interfaces.* Surface Science Reports, 1996. **26**: p. 205-259.
20. Rezek, B., H. Watanabe, and C.E. Nebel, *High carrier mobility on hydrogen terminated (100) diamond surfaces.* Applied Physics Letters, 2006. **88**(4): p. 042110.
21. Ueda, K., et al., *Diamond FET Using High-Quality Polycrystalline Diamond With f_T of 45 GHz and f_{max} of 120 GHz.* IEEE Electron Device Letters, 2006. **27**(7): p. 570-572.
22. Calvani, P., et al., *DC and RF performance of surface channel MESFETs on H-terminated polycrystalline diamond.* Diamond and Related Materials, 2009. **18**(5-8): p. 786-788.
23. Ley, L., *Surface Conductivity of Diamond*, in *CVD Diamond for Electronic Devices and Sensors*, R.S. Sussman, Editor 2009, John Wiley & Sons Ltd.: London. p. 69-102.

24.   Baumann, P.K. and R.J. Nemanich, *Electron affinity and Schottky barrier height of metal–diamond (100), (111), and (110) interfaces.* Journal of Applied Physics, 1998. **83**(4): p. 2072-2082.

25.   Riedel, M., J. Ristein, and L. Ley, *Recovery of surface conductivity of H-terminated diamond after thermal annealing in vacuum.* Physical Review B, 2004. **69**(12).

Chapter 3.

Technology and Development
of CVD Diamond Dosimeters

This Chapter deals with all the aspects concerning the fabrication of CVD diamond dosimeters starting from a description of the physical properties of the radiation-sensitive samples employed, passing through a short digression about the characteristics of metal-diamond contacts and finally with a detailed discussion of how the devices have been developed, bonded and encapsulated according to specific recipes that maximize their performance.

3.1 CVD Diamond samples.

The aim of this thesis is the development of x-ray detectors and dosimeters based on single-crystal CVD diamond films which represent today a reference material under the point of view of homogeneity and reproducibility of their electronic properties. This is not obvious for diamond technology, since polycrystalline films, although resulted good materials for radiation detection, presented the main lacks exactly in inhomogeneous physical properties.

Dosimeters have been developed starting from two different families of diamond films produced by Element Six Ltd. Element Six Ltd is the reference company for diamond deposition, controlled by the historically known De Beers group for use of diamond in gemmology. By exploiting the technological advances performed in the CVD homoepitaxy [1], Element Six in the recent past allowed diamond single-crystal films to have physical properties even superior than natural diamond. This induced monocrystalline CVD diamond to become a commodity product. Consequently, the research and development to be performed on diamond detectors is not anymore

focused only on the material, but it is shifted towards the device structures and metallization technology.
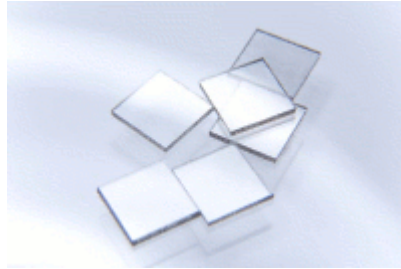

Fig. 3. 1. Electronic-grade samples employed in this thesis.

The sample families employed to develop x-ray detectors in this thesis activity can be divided into optical and electronic grade diamond films. They differ in the defect concentration and thus in the electronic properties, while they have comparable lateral size (about 4.5×4.5 mm^2) and thickness (about 500 μm).

Table 3.I reports a synthetic comparison among the two sets. The surface crystallographic orientation is along the {100} direction with a roughness that changes from a value <10 nm for the optical grade samples to a value <5 nm for the electronic-grade ones. As discussed, the main difference among the samples is the electrically active defect concentration (not considering that possible diamond lattice defects, such as vacancies or dislocations, are not declared and their influence on material performance has to be analyzed with our characterization techniques).

	Optical-grade Samples	*Electronic-grade Samples*
Lateral size	$(4.6\pm0.1) \times (4.6\pm0.1)$ mm^2	$(4.6\pm0.1) \times (4.6\pm0.1)$ mm^2
Thickness	500 ± 50 μm	500 ± 50 μm
Crystallographic Orientation of Surfaces	{100} ± 3 deg	{100} ± 3 deg
Surface roughness	<10 nm	<5 nm
Nitrogen concentration	<1 ppm	<5 ppb
Boron concentration	<0.05 ppm	<1 ppb
RT Electrons Mobility	1714 [2]	2145 ± 30 cm$^2 \cdot$V$^{-1} \cdot$s^{-1} [3, 4]
RT Holes Mobility	2064 cm$^2 \cdot$V$^{-1} \cdot$s^{-1} [2]	2430 ± 45 cm$^2 \cdot$V$^{-1} \cdot$s^{-1} [3, 4]
Electrons Lifetime	40 ns [2]	45 ns [3, 4]
Holes Lifetime	40 ns [2]	200 ns [3, 4]
Electrons Saturation Velocity	0.96×10^7 cm/s [2]	0.98×10^7 cm/s [3, 4]
Holes Saturation Velocity	1.41×10^7 cm/s [2]	1.54×10^7 cm/s [3, 4]
Customer Cost	190 €/film	~1000 €/film

Table 3. I.

Optical-grade samples have a nitrogen and boron concentration smaller than 1 and 0.05 part-per-million (ppm), respectively. Electronic-grade films show values minor than 5 and 1 part-per-billion (ppb) for N and B, 200 and 50 times lower than optical-grade diamond. This difference induces a sensible increase (about 25%) of charge-carrier mobility at room-temperature (RT), both for electrons (2145 versus 1714 $cm^2 \cdot V^{-1} \cdot s^{-1}$) and for holes (2430 versus 2064 $cm^2 \cdot V^{-1} \cdot s^{-1}$) [3, 4]. Larger values as 4500 and 3800 $cm^2 \cdot V^{-1} \cdot s^{-1}$ for electrons and holes have been reported in literature [5], but only under conditions of very low electric fields. Carriers saturation velocities among the samples sets are not so different, with an increase of about 2% and 10% for electrons and holes, respectively.

Finally the cost at the customer, which can be considered approximately proportional to the production cost. Electronic-grade diamond films are at least five times more expensive than optical-grade ones. A non secondary objective of this thesis is to verify if this cost difference is valuable with respect to a possible enhancement of resulting detector performance.

3.2 Metal-diamond contacts.

Metal–diamond contacts are the fundamental way to extract signal for almost any kind of device. The requirements on the typology of contacts varies from application to application. The ohmic or rectifying behaviour of metal-semiconductor junctions depends considerably on the surface termination. From an industrial point of view, for diamond oxygen-terminated surfaces guarantee reproducible properties and are the most easy to achieve.

Diamond is a wide bandgap semiconductor and, as in all the semiconductors, the contact resistivity, and consequently its behaviour, depends strongly on the concentration of doping level. In the p-type diamond, doping levels larger than 10^{20} cm^{-3} can be achieved, therefore in such conditions ohmic contacts are relatively simple to obtain [6]. On the other hand, it has been demonstrated that a thermal annealing of contacts fabricated by carbide-forming metals induces the arrangement of carbides at the metal–diamond interfaces, resulting in a reduction of the contact resistivity. Contact resistivities as low as 10^{-7} $\Omega \cdot cm^2$ can be achieved after annealing. The use of metal that allow the formation of a carbide is a practical alternative if doping technique cannot/should not be used.

Production of good ohmic contacts on n-type diamond is a controversy topic. The carbide formation has not the same effect compared with the p-type material, resulting in high contact resistivities ($>10^3$ $\Omega \cdot cm^2$) that are not useful for practical applications.

3.2.1 Specific contact resistivity.

Contacts on common semiconductors employ depletion regions which result mainly from the action of surface states. They show ohmic behaviour with a linear current–voltage characteristic on degenerated doped semiconductors [7]. In the case of a depletion contact, its resistivity depends exponentially on the Schottky barrier height formed by the specific metal on the semiconductor. An ohmic behaviour can be achieved if

1. the barrier height is small, so that the charge carriers can easily overcome the barrier (thermionic emission),
2. the charge carriers are able to pass through the depletion region by quantum-mechanical tunnelling,
3. tunnelling mainly takes place between the top of the barrier and the Fermi level, namely by field emission.

The specific contact resistivity ρ_c, which is a figure of merit independent of the contact size and geometry, is defined as the derivative function of the voltage drop over the junction of current density at the fixed voltage of 0 V. The asymptotic analytical expressions for the contact resistivity can be obtained [6] as a function of the three-current transport mechanisms:

$$\rho_c \propto \begin{cases} e^{\frac{q\phi_B}{kT}} & 1. \\ e^{\frac{q\phi_B}{E_{00}\coth(E_{00}/(kT))}} & 2. \\ e^{\frac{q\phi_B}{E_{00}}} & 3. \end{cases} \tag{1.1}$$

where k is the Boltzmann constant, T the temperature, q the elementary charge, ϕ_B the Schottky barrier height, E_{00} the characteristic tunnelling energy depending on the square root of the doping concentration N:

$$E_{00} = \frac{q\,h}{4\pi}\sqrt{\frac{N}{m\,\varepsilon_0\varepsilon_s}} \tag{1.2}$$

being h the Planck constant, m the effective charge mass in diamond, ε_0 and ε_s the vacuum permittivity and the diamond dielectric constant (equal to about 5.7), respectively. Eq. (1.2) dependence derives from the depletion layer width of a metal-semiconductor contact which is proportionally dependent on the square root of the reciprocal doping concentration. Consequently, the depletion layer width reduces with the increase of doping concentration and the tunnelling

probability increases. When the doping concentration is increased, charge transport is dominated by tunnelling through a narrowed barrier rather than by thermionic emission over a lowered barrier. In the first two transport mechanisms, the specific contact resistivity decreases with temperature and increases exponentially with the barrier height. For field-emission transport, the contact resistivity is not a function of temperature.

We could distinguish the three transport mechanisms by considering the predominance of characteristic tunnelling energy with respect to the thermal energy kT. In fact, if

1. $kT >> E_{00}$, the transport is ruled by thermionic emission,

2. $kT \approx E_{00}$ the quantum-mechanical tunnelling is dominant,

3. $kT << E_{00}$ field-emission dominates the conduction.

3.2.2 Schottky junctions.

The diamond wide bandgap and its strongly covalently bonded lattice can induce the assumption that the Schottky barrier height is independent of the work function of the metal and of the electron affinity. Following the empirical Mead and Spitzer rule [8], the Schottky barrier height of a covalent p-type semiconductor is one-third of the energy bandgap. Therefore, barrier heights in the range of 1.8 eV for diamond are expected.
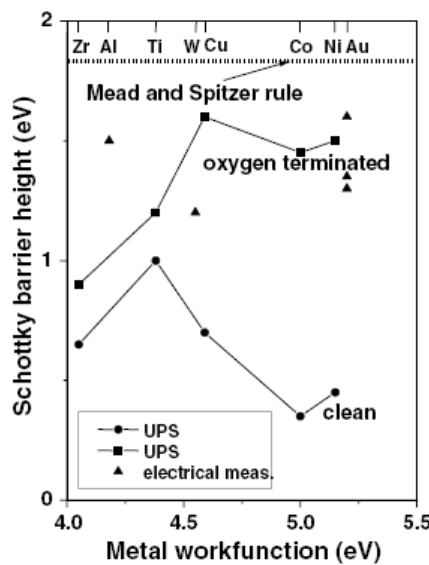

Fig. 3. 2. Measured Schottky barrier height for clean and oxygen-terminated diamond surface.
The dashed line refers to the Mead and Spitzer rule [6].

Experimental studies of Schottky barriers of nickel on diamond clean surface [9] measured a Schottky barrier height of 0.5 eV, whereas the one formed by copper was investigated Cu–diamond interfaces by means of UV photoemission spectroscopy (UPS), finding that the Schottky barrier heights were the lowest for clean surfaces and the highest for oxygen-terminated surfaces. The values for hydrogenated surfaces are in the middle. According to these results, the surface termination and therefore the cleaning procedure prior to metal deposition have a significant effect on the Schottky barrier height. Fig. 3. 2 compares measured Schottky barrier heights on clean and oxygen-terminated surfaces [10, 11]. However, oxygenated surfaces, which generally induce larger Schottky barrier heights, can be obtained in a much more simple way compared to clean diamond surfaces. In fact, for clean surface it is intended a surface on which the adsorbates and chemical terminations are removed under ultra-high-vacuum conditions, and all the successive treatments, comprehending metallization, occur under the same conditions.

The interaction of diamond with hydrogen has received much attention recently. Hydrogen can be present in the bulk and at the surface of the as-grown material and induces an electron affinity variation. The standard Schottky contact on diamond with hydrogen-terminated surface is aluminium, not for its barrier height of about 0.8 eV [12], but because after its deposition it reacts to form a aluminium-oxide layer of 5 - 10 nm thickness at the interface [13].

3.2.3 Ohmic junctions.

The conventional metallization method for obtaining metal-diamond ohmic junctions consists of the deposition of a thin adhesion layer, typically titanium, on the very diamond surface coated by a thicker interconnect metal layer, typically gold. In general the requirements for achieving ohmic contacts can be summarized by the following properties [6]:

- low contact resistivity,
- good adhesion,
- high thermal stability,
- high corrosion resistance,
- bondable top-layer,
- compatibility with micro-patterning.

For semiconductors, the standard way to obtain low contact resistivities is heavily doping of the contact area. Boron-doped diamond can reach doping concentrations up to about 10^{22} cm^{-3} have been reported [14]. Due to the high doping concentration, the depletion layer width is spatially reduced so that quantum-mechanical tunnelling becomes predominant. On the one hand, large barrier heights lead to high contact resistivities.

In our study, we start from non-intentionally doped crystals, which are more close to an intrinsic behaviour. According to the described trends, we should expect high contact resistivities in the development of ohmic contacts with standard techniques. On the other hand, we would like to avoid doping since diffusion techniques are not controllable owing to the small lateral size of films. Moreover, ion implantation is an expensive technique that is in contrast with our strategy of fabricating diamond devices characterized by developing structures as simple as possible, which could represent an advantage of diamond technology compared to silicon one.
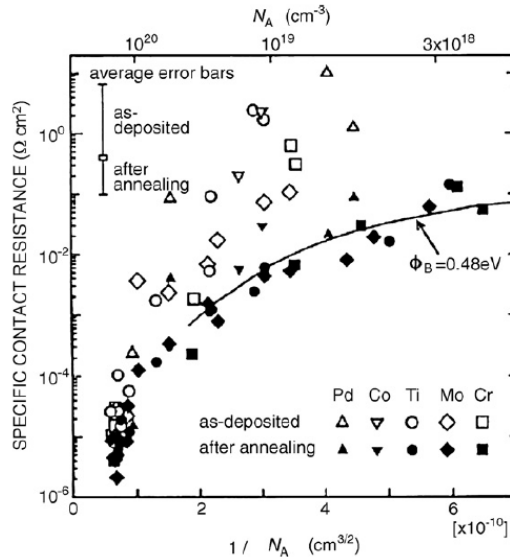
Fig. 3. 3

Metals that form carbides on diamond surface could represent an alternative solution. Carbide formation takes place at annealing temperatures up to 450 °C [14]. Molybdenum [15] and titanium [16] were reported to produce a carbide layer on diamond surface. Two models were suggested in order to explain the thermally-driven drop in the contact resistance and the consequent transition in current–to-voltage characteristics from rectifying to ohmic behaviour. One model is based on the assumption that the carbide acts as a defect layer which decreases the metal–diamond barrier height or favours tunnelling, or both. Another model proposes an average decreasing amount of local disorder caused by the annealing [17]. If a sufficiently large density of bandgap states have been induced near the Fermi level, then some type of carrier transport can take place with the help of these states. The two models are equally reasonable since the contact resistance cannot be explained only by tunnelling, but by a concomitant effect of the gap states. Experimental results shown in Fig.

3. 3 do not fit any of the relations described in (1.1). But, only in qualitative agreement with the theory, the contact resistivity ρ_C drops with increased doping concentration as $\rho_C \propto N_A^{-n}$, where n depends on the metal type (Fig. 3. 4). Therefore, transport through the contact is surely by tunnelling, with a component to be better understood.
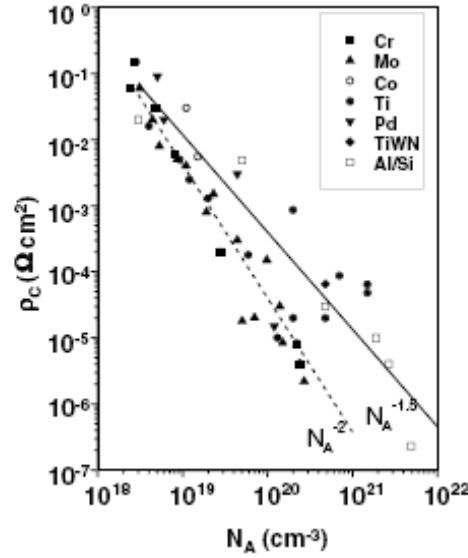
Fig. 3. 4

Other metals capable of forming carbide are tungsten and silicon/aluminium, palladium, cobalt and chrome. All discussed metals satisfy conditions of good adhesion on diamond surface, thermal and mechanical stability, corrosion resistance and possibility to be bonded. Moreover, they are compatible for patterned depositions by using photolithographic methods. Therefore, the development of ohmic contacts by carbide formation represents the simplest method used to fabricate our radiation dosimeters discussed. As a confirmation of this method efficacy, in Fig. 3. 5 the low Schottky barrier heights (about 0.5 eV) for Ti, Mo, Cr, Pd and Co after annealing are shown.
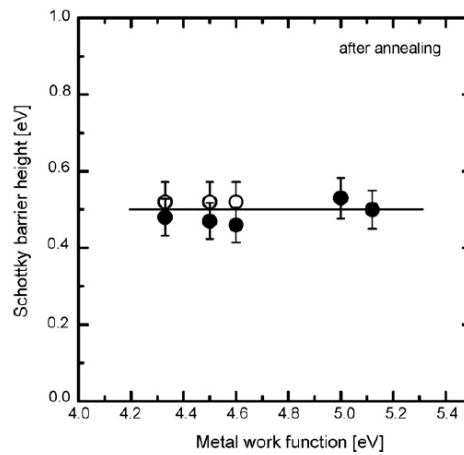
Fig. 3. 5. Schottky barrier heights of the (from left to right) Ti, Mo, Cr, Pd, and Co contacts at the diamond-contact interface as a function of metal work functions [18].

Another way to produce injecting contacts was recently developed by Diamond Detectors Ltd, that had a strict collaboration with us during this thesis activity. This collaboration allowed us to characterize electronic-grade diamond films, since this British society owned the exclusivity of use of such material from Element Six Ltd until 2010, after that it has become a product sold freely. Diamond Detectors Ltd prepared metal contacts on electronic-grade diamond films according to a proprietary technique [19], consisting in the formation of a diamond-like-carbon (DLC)/Pt/Au multilayer, where the very thin DLC layer (1 – 3 nm) is obtained by a soft damage of the diamond first surface layers without annealing. It has been demonstrated that such layer works by charge carrier tunnelling with the aim to avoid space-charge effects caused by charge accumulation near the metal-diamond junctions [3, 20].

On the other hands, for hydrogen-terminated diamond surfaces the standard metal is gold, that although has a high barrier height on oxygen-terminated surfaces, thanks to the diamond electron affinity variation (see Paragraph 2.5) is able to form ohmic junctions characterized by a contact resistivity of about 10^{-5} $\Omega \cdot cm^2$ without post-annealing [21].

Concluding, we agree and apply the synthetic recipe about the contacts behaviour of oxygen-terminated diamond surfaces from Koide [18] who states that *a guideline for preparing the ohmic contact is to select the contact metal which produces a carbide or a solid solution at elevated temperatures and (for preparing) the Schottky contact consists in selecting the contact metal which does not produce the reaction between the diamond and the metal at elevated temperatures. This is the important guideline for selecting thermally stable ohmic and Schottky contacts.*

3.3 Development of the dosimeters.

By treasuring up the activity that the Solid State and Diamond Electronic Lab (S2DEL) already performed on polycrystalline diamond dosimeters [22-25], the diamond films were encapsulated according to a specific design with the aim to negligibly perturb the incident radiation dose. The overall strategy in developing the device is focused on the use of low absorption coefficient materials: Rexolite® for the plastic container and by bonding the device contacts with small-size wires (99% Al-1% Si, 25μm cross-section to connect them to a 2.5m long triaxial low-noise cable) to minimize the cable interaction volume.

A particular attention was paid to the choice of low atomic number metals for electrical contacts of the optical-grade samples: titanium was used to form squared ohmic junctions on film surface

according to a sandwich structure. A guard ring realized on the front film side with respect to the incident radiation direction, surrounds the 3.5×3.5 mm^2 Ti front contact, while the back contact has an approximate size of 4.5×4.5 mm^2.

Electronic-grade films have two DLC/Pt/Au contacts developed by Diamond Detectors Ltd, with a sandwich device structure. After a primary characterization, they were encapsulated as well as optical-grade ones.

3.3.1 Substrate cleaning procedure.

Each diamond sample has to be cleaned before proceeding the successive device development phases. Chemical pre-treatment is aimed to provide an oxygen-terminated surface with the removal of non-diamond contaminants on surface and to induce initial reproducible chemical conditions.

Surface cleaning is performed by using a boiling solution composed by perchloric, nitric and sulphuric acids mixed in equal volumes (1:1:1), followed by a rinsing in de-ionized water and dry air and a final rinsing in isopropyl alcohol. The resulting diamond surfaces are oxygen-terminated. The described solution has been preferred to sulphochromic mixture (sulphuric acid, chromic trioxide, dichromate) since it is a cleaner process, not polluting the surfaces with chrome and sulphur as sulphochromic mixture does.

3.3.2 Preparation of photolitographic masks.

The necessary masks for the lithographic process have been prepared by direct writing by using a HeCd laser beam (wavelength of 442 nm and output power of 50 mW). The direct writing system is composed by a neutral attenuation filter able to reduce the power down to 100 µW, an electromechanical shutter, a 9X microscopy ocular and an x-y motorized system that holds the quartz. The quartz presents a thermal evaporation of chrome successively covered by photoresist.

A PC controls the shutter to deliver the appropriate radiation dose to expose the resist and the motion system according to the mask design bitmaps, while the beam position is fixed. The photoresist is then directly and selectively exposed to the radiation. After photoresist development, the chrome is removed by wet etching (Microposit® Chrome Etch 18). The maximum resolution of the system is limited by the laser spot diameter on the mask holder. It is, in our case, equal to about 4 µm, a value sufficient for macro-structures, typical of detectors' contacts.

In Fig. 3. 6 the simple mask designs for realization of back contact, front contact and guard-ring are shown. Specific signs for optimal alignment are visible in the patterns.
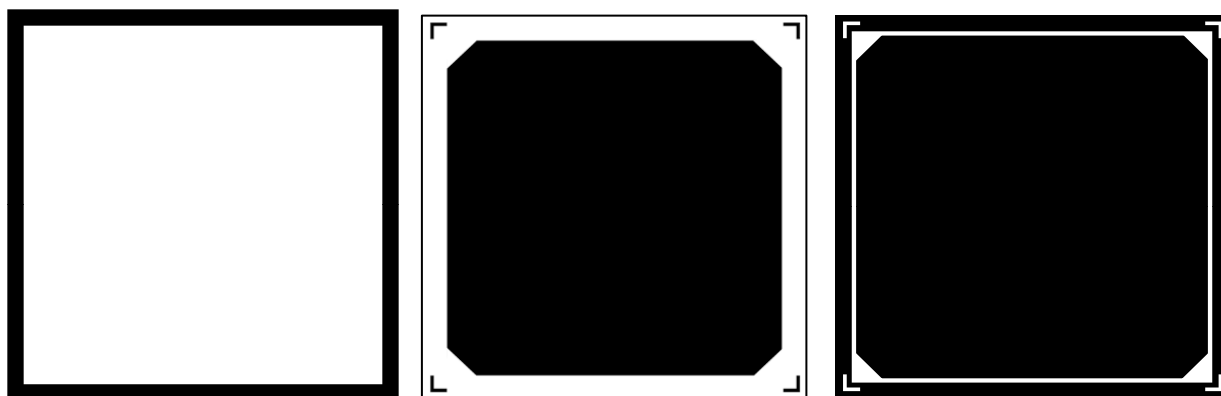

Fig. 3. 6. Designs of the masks necessary for metal contacts development.
From left to right: the mask for back contact, the inverted mask for front contact and the one for guard-ring

3.3.3 Metallization.

The metal contacts have been realized on diamond films by using photolithographic techniques. Each photolithographic process has been performed by using the positive resist Novolac®, based on diazonaphthoquinone molecule. Resist thickness has been optimized to the value of 1.4 μm by acting on the spin-coating rotation speed. The deposition has been followed by a soft-bake process performed at 80 °C for 30 minutes in order to reduce resist solubility, whereas the development has been preceded by a hard-bake at 130 °C for 30 minutes in order to make resist more chemically resistant to the action of acids for metal wet-etching. For the development, Microposit EC-Solvent has been used.

Resist exposure has been performed with the mask at contact with the sample, with a 1:1 scale proportion between mask dimension and projected pattern. The mask-aligner used is a Karl Suss MA6 with a 275 W mercury UV lamp able to precisely work at constant intensity. The system is equipped with optics able to block IR letting UV to pass towards the mask and a 9X microscopy to visualize the mask-sample alignment, whose control is obtained by acting on micrometer screws. Remembering that the maximum resolution for such a system is proportional to $\sqrt{\lambda g}$ (λ is the radiation wavelength and g the distance between mask and sample), we can assume that the exposure system does not limit the mask initial resolution.

The technological steps for optical-grade diamond films are (Fig. 3. 8):

1. Deposition of resist by spin-coating over a diamond film surface.
2. Exposure of resist to back contact mask and successive resist development.
3. Deposition of back-contact metal by RF sputter technique (in our case titanium with 150 nm thickness).
4. Removal of photoresist and odd titanium by lift-off.
5. Deposition of front contact on the whole opposite film surface by RF sputter (in our case titanium with 150 nm thickness).
6. Deposition of resist by spin-coating.
7. Exposure of resist to front contact mask and successive resist development.
8. Wet etching of not masked metal (for Ti by using a diluted solution of nitric acid).
9. Photoresist removal.
10. Thermal annealing at 450 °C under vacuum conditions to make the contact ohmic (see paragraph 3.2).
11. Deposition of resist by spin-coating over the front contact film surface.
12. Exposure of resist to guard-ring contact mask and successive resist development.
13. Deposition of guard-ring metal by RF sputter (in our case aluminium with 150 nm thickness).
14. Removal of resist and aluminium by lift-off.

The steps 1-4 deals with the back contact fabrication, the 5-9 steps with the front contact fabrication. After the thermal annealing (step 10) the dosimeter could be considered ready to be used. Fabrication of guard-ring is connected to the steps 11-14.
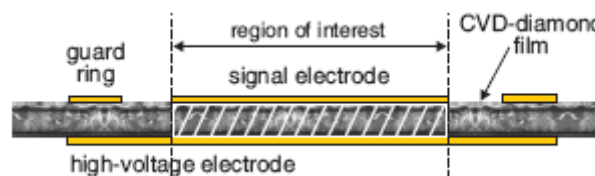
Fig. 3. 7. Dosimeter structure with the presence of a guard-ring [26].

The presence of the guard is taken from the technology of parallel plate ionization chambers, where the charge-collecting electrode is surrounded by an annular ring. The annular ring represents the guard-ring and is separated from the collecting electrode by a narrow insulating gap, and the applied voltage to the guard ring is the same as that to the collecting electrode. The other parallel

plate electrode has a diameter at least as great as the outer diameter of the guard electrode (Fig. 3. 7). With this geometry and voltage arrangement the guard electrode serves two major purposes, although they are directly linked. First, it ensures that the electric field lines near the edge of the collecting electrode remain straight, perpendicular to both the collecting electrode and the second electrode so that the collecting volume is accurately defined by the area of the collecting electrode and the electrode separation. In fact, if no guard electrode is used, the field lines near the edge of the collecting electrode will tend to bow out, resulting in a poorly defined charge collecting volume. Secondly, maintaining the same voltage on the collecting electrode and the guard ring minimizes the extent of charge leakage from the volume outside of the collecting volume because there is no significant driving potential to promote this additional charge collection by the collecting electrode in preference to collection by the guard electrode.

For optical-grade samples the back and front contact metal is titanium, that was chosen since it is the lowest atomic-number metal (Z = 22) able to form a carbide and thus an ohmic junction after a thermal annealing. For guard-ring, the metal selected is aluminium since it produces a relatively high barrier height that forms an inverse diode with the aim of blocking any possible shunt currents. Moreover, aluminium is a low atomic-number metal (Z = 13). We have taken a particular care in selecting low atomic-number materials since they present a small absorption coefficient to x-rays that induces a negligible perturbation to the radiation beam to monitor.

Back-contact fabrication

CVD diamond film
($4.5 \times 4.5 \times 0.5$ mm^3)

Positive photoresist deposition by spin-coating

Exposure and development

150 nm thick Ti deposition by RF sputtering

Photoresist removal

Front-contact fabrication

150 nm thick Ti deposition by RF sputtering

Positive photoresist deposition by spin-coating

Exposure and development

Wet etching of not masked Ti

Photoresist removal

Thermal annealing at 450 °C in vacuum

Positive photoresist deposition by spin-coating

Guard-ring fabrication

Exposure and development

150 nm thick Al deposition by RF sputtering
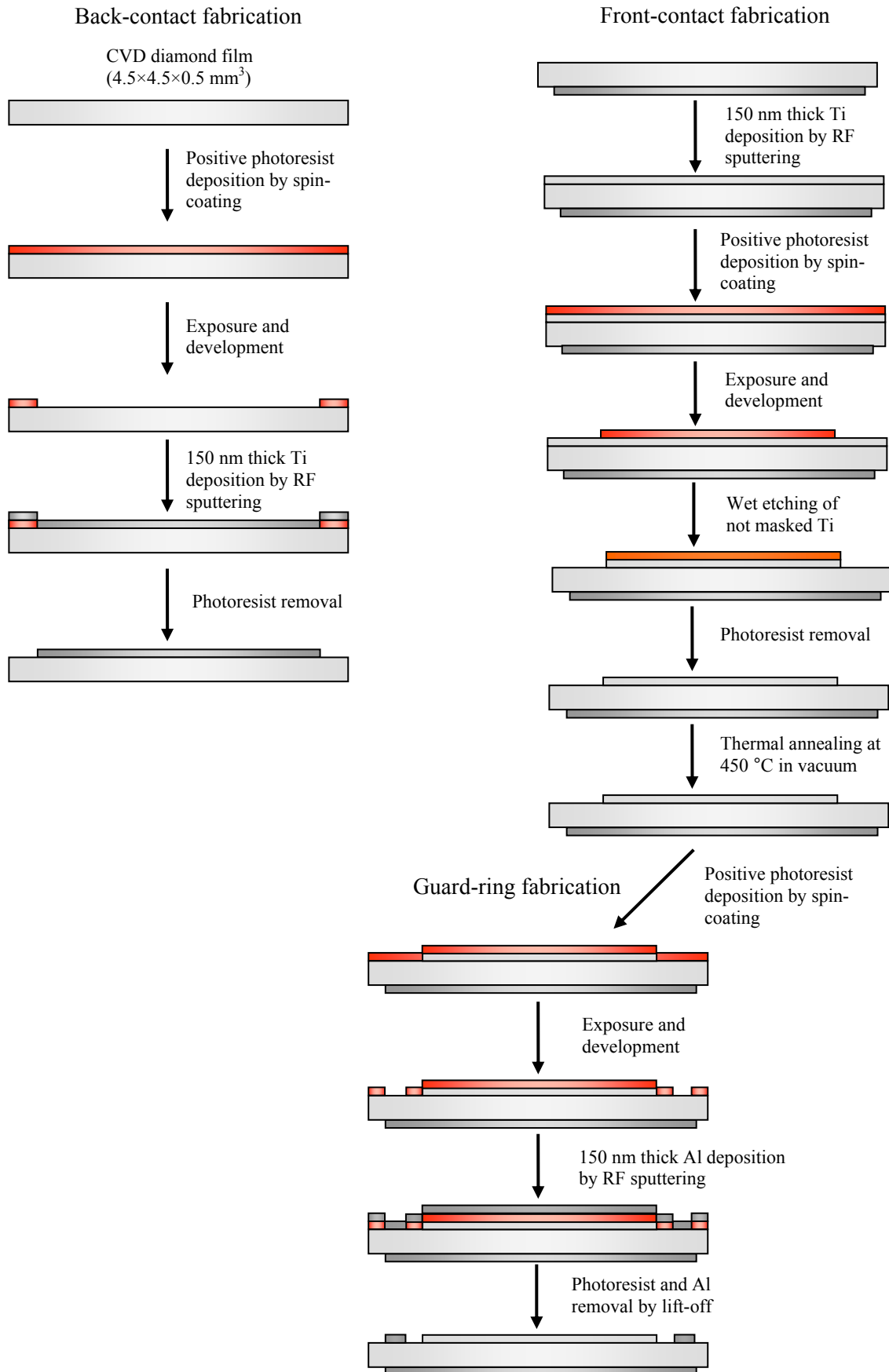
Photoresist and Al removal by lift-off

Fig. 3. 8

66

Titanium contacts define the device active area and thus are always impinged by the beam. Aluminium guard-ring could introduce perturbation for example in oblique beam incidence. Metal thickness is about 150 nm since it was observed that values smaller than the 200 nm threshold are acceptable in terms of absorption [25, 26] even for higher Z metals as gold and platinum. A typical resulting structure for optical-grade diamond based detectors is shown in Fig. 3. 9.
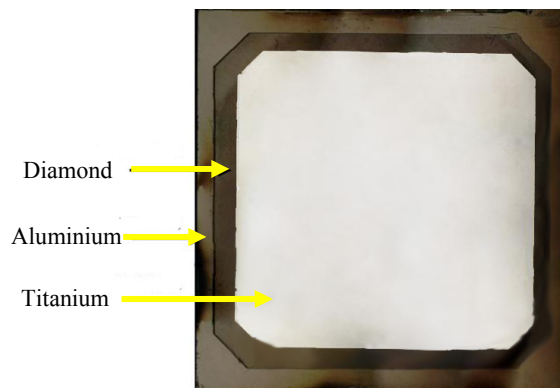

Fig. 3. 9

Electronic-grade samples have been completely metalized by Diamond Detectors Ltd according to their patented technique [19]. Samples have no guard-ring, but only a front (homogeneously covered or according to a grid structure) and a back contact. The fabrication steps for each contact is similar to steps 1-4 performed by us on optical-grade films. The difference is that the RF sputter deposition foresees two successive depositions: one performed with Pt atoms, the second with gold. Platinum is a large atom compared to carbon. If Pt ions are accelerated by a high voltage, the first ions heavily bombard the diamond surface, inducing for diamond a soft structural damage. A very thin layer (from 1 to 3 nm) of diamond-like-carbon can be formed. Diamond-like-carbon (DLC) is a kind of carbon material that maintains the predominance of sp3 bonds like in diamond, but the lattice atoms are disposed only under a local order. The long range lattice order is lost. Although it is a defected region, DLC layer is very well structurally compatible with diamond and, due to its limited thickness, charge carriers can easily pass it through by tunnelling mechanisms. After a defined time, the Pt ions' acceleration voltage is decreased and a standard platinum layer with thickness of about 100 nm is deposited. After that, the gold deposition (100 nm thick) on platinum layer makes the contact more easy to be bonded. The total thickness of the contact is about 200 nm, which is complaint with the requirements previously described [25].

3.3.4 Limited-size technological issues.

Owing to the limited size of diamond films, special cunnings have been adopted in fabricating the contacts. Issues have been faced especially in developing structures at the edges of the films: in this case, resist spinning did not provide a constant thickness over the film surface, but thickness increased at the angles. This induced non perfect development of the contacts, resulting in resist imperfect removal and/or damaged and interrupted structures, as shown in Fig. 3. 10.

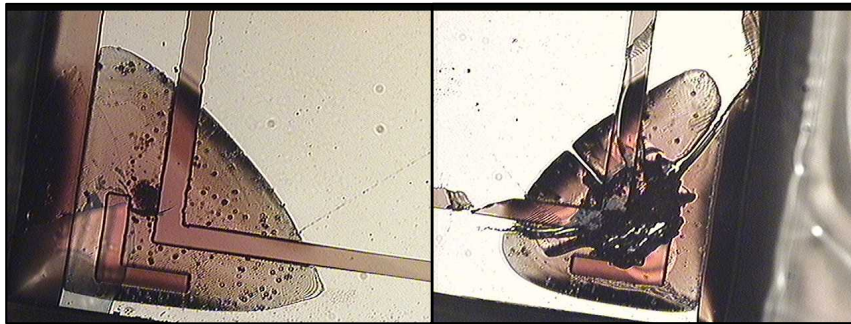Fig. 3. 10. Examples of imperfections caused by limited size of diamond films.

The way to reduce this unavoidable effect has been found by adapting masks that avoid important structures exactly at the films' angles. Fig. 3. 11 shows an example of the guard-ring mask evolution with the aim to avoid the described unwanted effects.
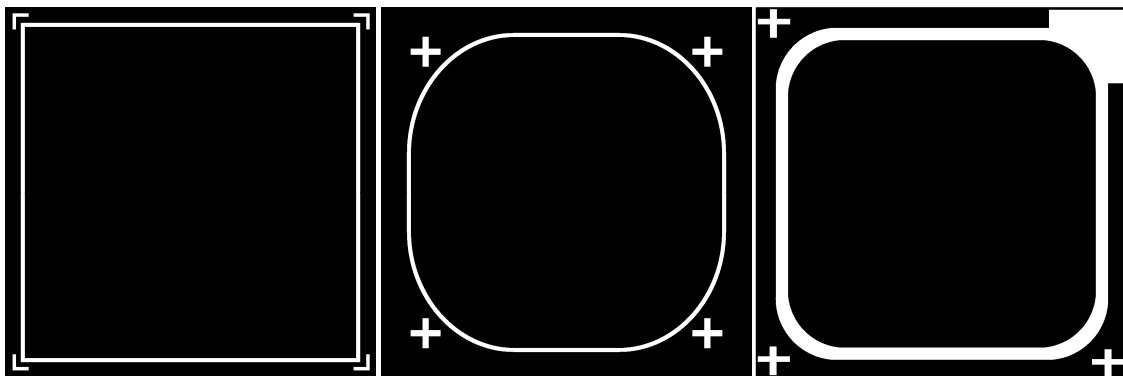

Fig. 3. 11. From left to right: evolution in time of the guard-ring mask.

3.4 Encapsulation.

The dosimeters have to be placed in a case able to provide airtight and watertight closure. The reasons are mainly related to

- prevention of mechanical damages,
- minimization of external noise,
- minimization of air-ionization caused by the high-energy radiation,
- waterproof characteristic in order to be placed in water phantoms, normally used in radiation therapy.

With all these aims, a plastic enclosure has been designed to properly and firmly contain the detector and to be filled by biphasic epoxy resin. The enclosure design has been evolved during the activity, with continuous improvements in its geometry and size. One of the first examples of enclosure design is shown in Fig. 3. 12. Technical issues have been faced for sample positioning and for obtaining a cavity for epoxy resin injection. This has been solved by designing two reciprocally fitting parts, one for the detector housing and related metal pads, the other to perform the final enclosure. The latter is characterized by a hole sufficiently large to allow the contemporary epoxy resin injection and air escape towards the external ambient. Some successive designs have two distinct smaller holes for the two functions.

The selection of the enclosure material has been carried out among materials with the lowest possible absorption coefficients to x-rays, considering an electrical resistivity larger than diamond to avoid lower impedance parallel paths and taking into account the stability under irradiation. The material enclosure chosen is Rexolite® 1422, a waterproof cross-linked polystyrene plastic with stable electrical properties (bulk resistivity $>10^{17}$ Ω·cm) up to GHz frequency range, often used in microwave, radar, and other high-frequency applications. The resin is made of polystyrene, a long polymeric chain of styrene molecules ($C_6H_5CH=CH_2$) shown in

Fig. 3. 13, and its density is equal to the low value of 1.05 g·cm^{-3}. Polystyrene is composed only by carbon and hydrogen atoms, two very low-atomic-number elements. The combination of a low Z material and a low density make polystyrene the optimal tissue-equivalent material that can minimize perturbations to the incident radiation beam.
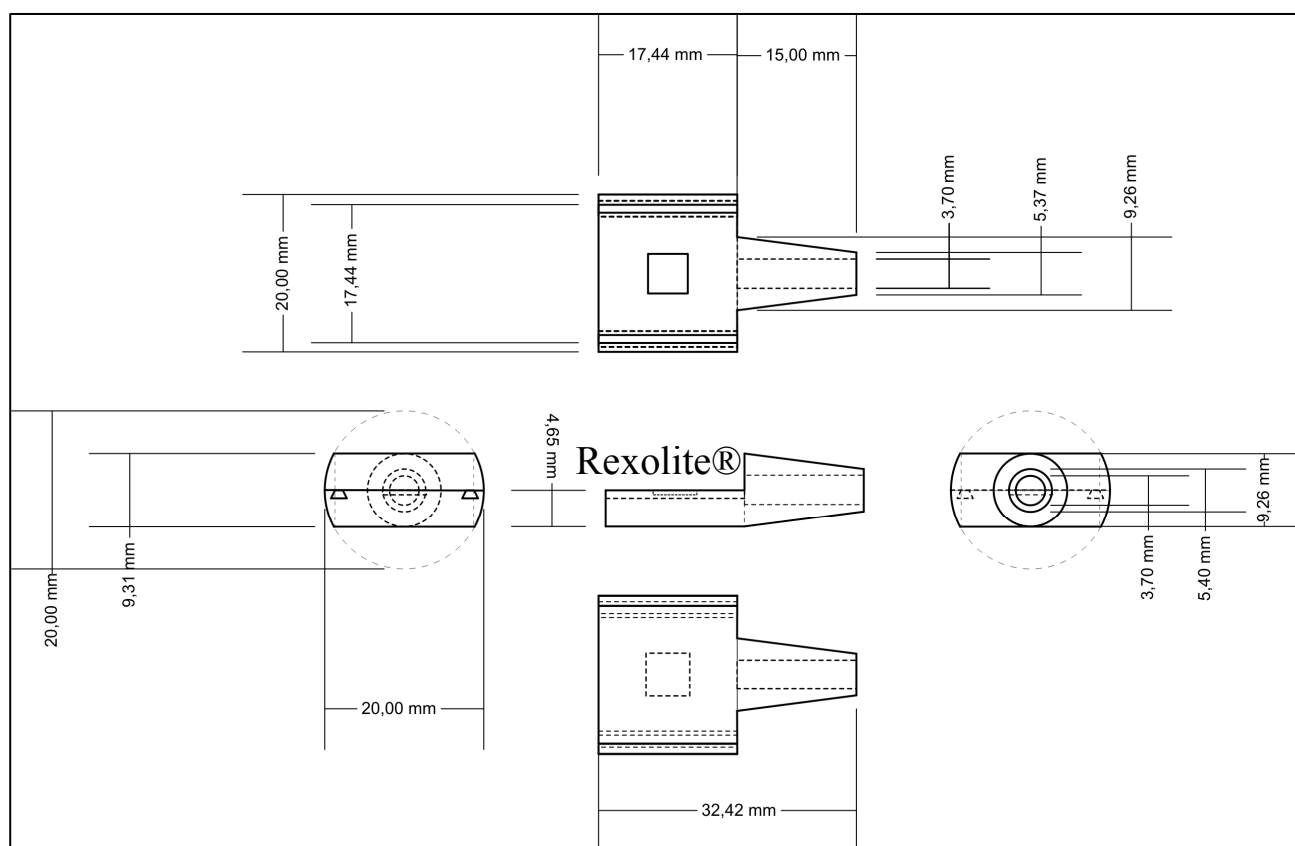
Fig. 3. 12. One of the first enclosure designs.
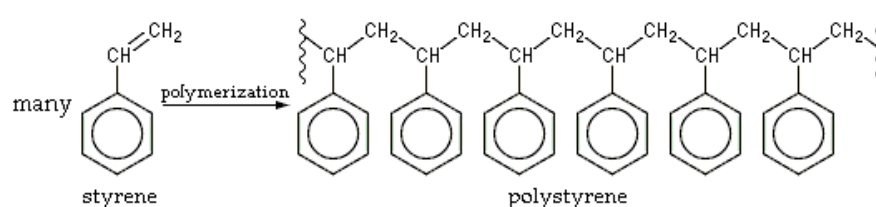
Fig. 3. 13. The polymeric chain of polystyrene.

A deposition of a very thin (50 nm) titanium pad has been executed on the square shaped housing for the sample in order to have electrical continuity for the dosimeter back contact. The square shaped housing in successive versions has become a rectangular one to allow a small part of the pad to be directly bonded. Once placed the detector inside the enclosure, its contacts have to be ultrasonically bonded to external metal pads, which are in turn connected to a triaxial cable by tin soldering. Pads provide a mechanical uncoupling between detector and cable. The bonding wires used are 25 μm section diameter wires made of 99% aluminium and 1% silicon, with the aim to reduce further possible undesired absorptions.

Fig. 3. 14. Encapsulation sketch showing the signal, bias voltage and guard-ring connections to the triaxial cable.

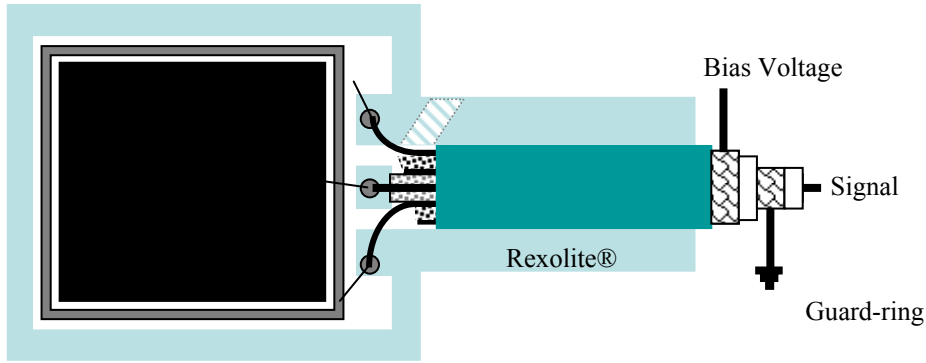The metal pads are positioned 3 mm far from the dosimeter active area. They are connected as shown in Fig. 3. 14 to a low-noise high-interference-rejection triaxial cable characterized by a contact resistance <0.5 Ω and an insulation between the core and outer shield is >10^{17} Ω·cm. The cable can be long up to 6 m and its characteristic impedance is 50 Ω, with a capacity core/outer shield of about 50 pF/m. Although this capacity per unit length is a small value, it has to be compared to the diamond dosimeter capacity. Diamond has a low dielectric constant of 5.7, its active contacts behave as a parallel-plate capacitor with typical areas of about 0.2 cm^2 positioned at a distance of 0.05 cm. This leads to geometrical capacities of the order of some pF. This has to be considered. The unique solution is minimizing the cable length (down to ten centimetres) when it is possible, especially during the frequency-dependent analysis.

After the ultrasonic bonding process, the two parts of the enclosure fit together and a biphasic epoxy resin can be injected inside. Epotek 301® has been used, a radiation and temperature resistant resin, characterized by a slow arrangement time (1 day at room temperature) useful not to induce stresses inside the enclosure. It is optically transparent up to UV radiation with a nominal electrical bulk resistivity of 5×10^{13} Ω·cm. This value appeared at a first sight not sufficiently high if compared to the resistivities of diamond films. But experimental measurements on a cubic centimetre sample of resin made to solidify according to standard arrangement has given us a bulk resistivity >10^{15} Ω·cm. A further confirmation comes from the comparison of dosimeter dark current-to-voltage characteristics before and after the encapsulation, that differ of values minor than the instrumental uncertainty.

Fig. 3. 15 shows one of the first versions of dosimeters housing before the final encapsulation and once encapsulated. The last process is the coating of the detector head with a black paint to avoid any possible interaction with visible light.
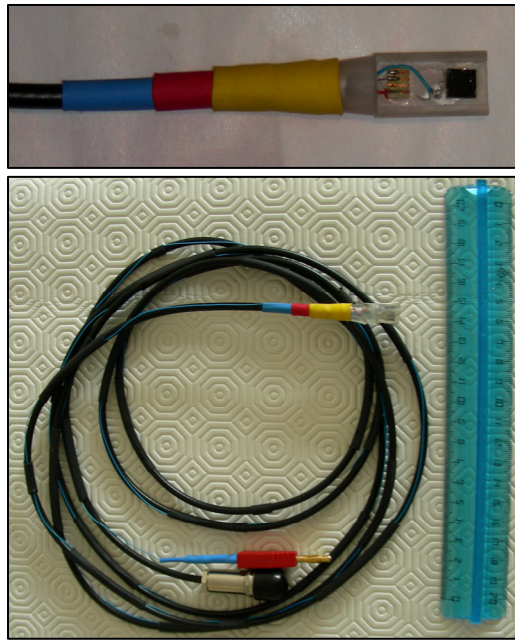
Fig. 3. 15. Example of a dosimeter mounted on the enclosure and once encapsulated.

References.

1. Lee, S.T. and Y. Lifshitz, *The road to diamond wafers.* Nature, 2003. **424**: p. 500-501.
2. Pernegger, H., et al., *Charge-carrier properties in synthetic single-crystal diamond measured with the transient-current technique.* Journal of Applied Physics, 2005. **97**(7): p. 073704.
3. Galbiati, A., et al., *Performance of Monocrystalline Diamond Radiation Detectors Fabricated Using TiW, Cr/Au and a Novel Ohmic DLC/Pt/Au Electrical Contact.* IEEE Transactions on Nuclear Science, 2009. **56**(4): p. 1863-1864.
4. Duenas, J.A. and I. Martel, *Timing properties of thin SC-CVD diamond detectors*, 2009.
5. Isberg, J., et al., *High Carrier Mobility in Single-Crystal Plasma-Deposited Diamond.* Science, 2002. **297**(5587): p. 1670-1672.
6. Werner, M., *Diamond metallization for device applications.* Semiconductor Science and Technology, 2003. **18**: p. S41-S46.
7. Werner, M., *Ohmic contacts*, in *Wiley Encyclopedia of Electrical and Electronics Engineering*, J.G. Webster, Editor 1999 Wiley: New York. p. 112.
8. Mead, C.A. and W.G. Spitzer, *Fermi Level Position at Metal-Semiconductor Interfaces.* Physical Review, 1964. **134**(3A): p. A713-A716.
9. van der Weide, J. and R.J. Nemanich, *Angle resolved photoemission of diamond (111) and (100) surfaces; negative electron affinity and band structure measurements.* Journal of Vacuum Science & Technology B: Microelectronics and Nanometer Structures, 1994. **12**(4): p. 2475-2479.
10. Baumann, P.K. and R.J. Nemanich, *Electron affinity and Schottky barrier height of metal–diamond (100), (111), and (110) interfaces.* Journal of Applied Physics, 1998. **83**(4): p. 2072-2082.

11. Baumann, P.K. and R.J. Nemanich, *Characterization of cobalt-diamond (100) interfaces: electron affinity and Schottky barrier.* Applied Surface Science, 1996. **104/105**: p. 267-273.

12. Kawarada, H., *Hydrogen-terminated diamond surfaces and interfaces.* Surface Science Reports, 1996. **26**: p. 205-259.

13. Kasu, M., et al., *Diamond RF FETs and other approaches to electronics.* physica status solidi (c), 2008. **5**(9): p. 3165-3168.

14. Werner, M., et al., *Charge transport in heavily B-doped polycrystalline diamond films.* Applied Physics Letters, 1994. **65**: p. 595-597.

15. Hewett, C.A. and J.R. Zeidler, *Issues in diamond device fabrication.* Diamond and Related Materials, 1992. **1**: p. 688.

16. Tachibana, T., B.E. Williams, and J.T. Glass, *Correlation of the electrical properties of metal contact on diamond films with the chemical nature of the metal-diamond interface. I. Gold contacts: A non-carbide-forming metal.* Physical Review B, 1992. **45**(20): p. 11968-11974.

17. Werner, M., et al., *Electrical characterization of Al/Si ohmic contacts to heavily boron doped polycrystalline diamond films.* Journal of Applied Physics, 1996. **79**: p. 2535.

18. Koide, Y., *Metal–diamond semiconductor interface and photodiode application.* Applied Surface Science, 2008. **254**(19): p. 6268-6272.

19. Galbiati, A., *Contacts on diamond*, D.D. Ltd., Editor 2010: Great Britain.

20. Trucchi, D.M., et al., *Very Fast and Priming-less Single-Crystal Diamond X-ray Dosimeters.* IEEE Electron Device Letters, Submitted.

21. Ueda, K., et al., *Diamond FET Using High-Quality Polycrystalline Diamond With f_T of 45 GHz and f_{max} of 120 GHz.* IEEE Electron Device Letters, 2006. **27**(7): p. 570-572.

22. Conte, G., et al., *Temporal response of CVD diamond detectors to modulated low energy X-ray beams.* physica status solidi (a), 2004. **201**(2): p. 249-252.

23. Ascarelli, P., et al., *CVD diamond dosimetric response evaluated by X-ray absorbers method.* Diamond and Related Materials, 2003. **12**(3-7): p. 691-695.

24. Fidanzio, A., et al., *Photon and electron beam dosimetry with a CVD diamond detector.* Nuclear Instruments and Methods in Physics Research Section A: Accelerators, Spectrometers, Detectors and Associated Equipment, 2004. **524**(1-3): p. 115-123.

25. Górka, B., et al., *Influence of electrodes on the photon energy deposition in CVD-diamond dosimeters studied with the Monte Carlo code PENELOPE.* Physics in Medicine and Biology, 2006. **51**(15): p. 3607-3623.

26. Gorka, B., *Development of tissue-equivalent CVD-diamond radiation detectors with small interface effects*, in *Karolinska Institutet*2008, Stockholm University: Stockholm.

Chapter 4.

X-Ray Experimental Setup

In order to completely analyze the dosimeters' performance, an x-ray characterization setup was assembled. The x-ray photo-detection setup was designed to allow measurements under continuous (DC) and modulated radiation (AC) exposition. In this way it is possible to derive the current flowing into the devices, the total current under irradiation and the net photo-generated current, at the variation of modulation frequency, bias voltage and radiation dose-rate. The x-ray beam can be filtered by a primary and/or a variable thickness secondary filter (Fig. 4. 1).

The beam impinges orthogonally on the device. The detector is biased by a voltage generator: in case of continuous excitation, the dark and photo-generated current are measured by a pico-ammeter, while in modulated excitation, the net current signal is amplified and converted in a voltage signal by a current-voltage converter and sent to a lock-in amplifier, which compares the signal of interest with the reference one generated by the chopper controller.

The modulated electronic chain implies, with respect to continuous irradiation conditions, the advantage of:

- High SNR discrimination of signal,
- Independence of device leakage current for a broad current range (up to 0.1 mA).

This means that, under this operative condition, we can both evaluate the devices behaviour in DC irradiation (small modulation frequencies) and devices performance for AC applications.

All the setup is controlled by a computer via GPIB and RS-232 buses which has the function of collecting data and controlling the electronic instruments. A ionization chamber designed and calibrated for photons < 100 keV was recently introduced within the setup. The aim is to continuously monitor the source intensity, to compare the device under test performance with the dosimetric benchmark detector and to perform absolute dose measurements.

Cu or Mo
X-ray Tube
(Kα at 8.06 / 17 keV)

Ni / Zr Filter
Monochromatic
enhancement

Absorbers
(Al, Ni, Cr, Cu)

X-Ray mechanical
chopper

Motion
Controller

DUT

Ionization
Chamber
NE2536/3C

Analog 0-10 V

TTL

DAQ

I-V Pre-Amplifier
Signal Recovery 181 or 5182

$10^4 \div 10^9$
V/A

DC Signal

AC Signal
(Signal Module &
Phase)

Modulated
Irradiation
(AC)

Reference Signal
(frequency f)

Current Signal
$(10^{-12}\text{-}10^{-7}$ A)

Continuous
Irradiation
(DC)

Nanovoltmeter
Keithley 2182A

Lock-in Amplifier
Signal Recovery 7265 DSP

Voltage Source + Pico-ammeter
Keithley 6517A or Keithley 487

Electrometer
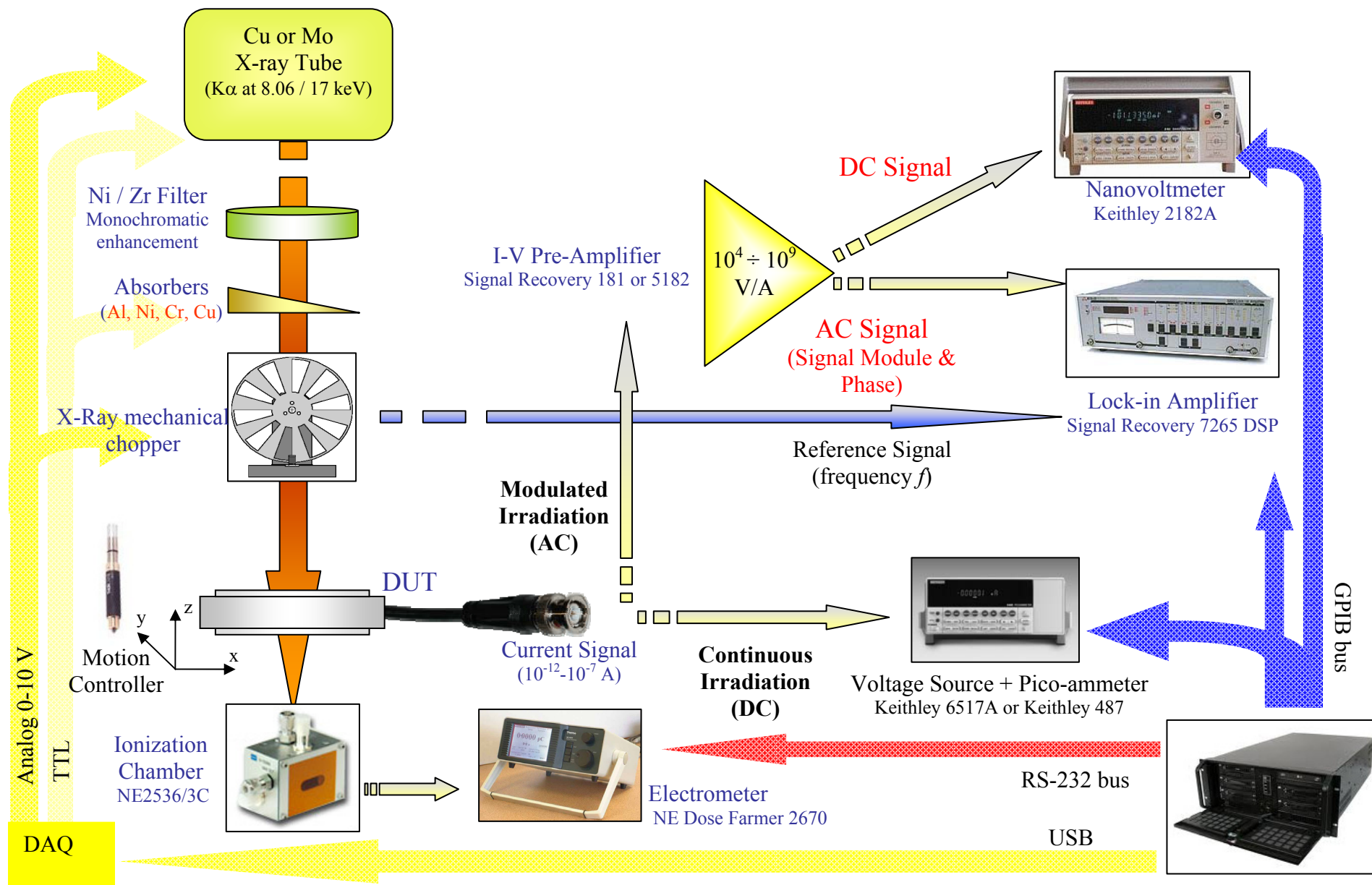NE Dose Farmer 2670

RS-232 bus

USB

GPIB bus

Fig. 4. 1. Schematic drawing of the x-ray photoconductivity setup.

4.1 Sources and filtering.

The radiation sources employed to characterize the dosimeters performance are a broad focus liquid-cooled copper tube, able to be supplied up to 2.7 kW power (details are shown in Fig. 4.1), and an air-cooled molybdenum one, characterized by a maximum power of 60 W. Apart from the intensity of the produced radiation, the main difference is in the spectral energy of emitted characteristic lines (Kα at 8.05 keV and Kβ at 8.90 keV for copper, Kα at 17.48 keV and Kβ at 19.61 keV for molybdenum). The continuous spectrum is established by the acceleration voltage V_{acc} which is fixed to the standard value of 40 kV for Cu tube and 45 kV for Mo tube.
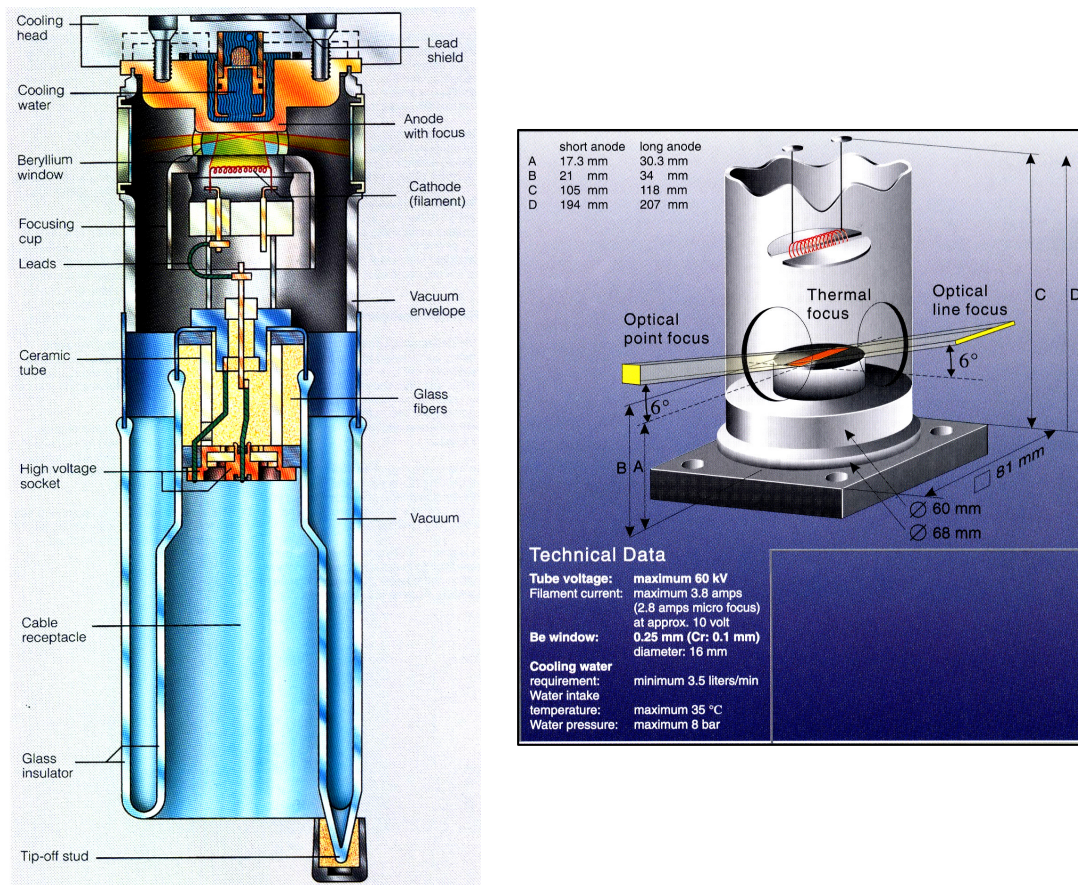

Fig. 4. 2. Drawing showing the technical details of the Cu tube used in the experimental setup.

The radiation emitted by the tubes can be absorbed by a primary filter consisting in a 15 ~ 25 μm thick nickel or zirconium thin-sheet with the aim of eliminating the Kβ line of copper and molybdenum, respectively. The resulting x-ray energy spectrums are composed essentially by the characteristic Kα line of the target material and of a very small part of Bremsstrahlung spectrum, in order to obtain a quasi monochromatic radiation. The radiation is then forced to pass through a

stainless steel collimator that establishes the x-ray beam exit spot size (the hole diameter can vary from 0.2 to 0.75 mm as a function of the specific collimator).

A secondary filter made of a pure material can be used for a controlled attenuation of the x-ray beam intensity and energy content as a function of its thickness. This technique is called the absorber method and was fruitfully employed in the past to characterize polycrystalline diamond detectors [1]. The filter used is a metal sheet (usually aluminium, nickel, chrome or copper) which has a well-known and tabulated absorption curve as well as a low absorption coefficient, in order to have a wide dynamic in thickness. This allows us to dispose of a large range of thicknesses.

Fig. **4. 3** reports synthetically the spectral content of the x-radiation impinging perpendicularly on the detector under test. The tube voltage establishes the energy spectrum, while emission current can be changed to obtain a variation of the radiation intensity and consequently of the dose-rate. Usually a variation of the x-ray tube current induces approximately a proportional to a variation of the dose-rate. Successively, primary filter and secondary one, establishing a precise thickness, can be applied.

The tubes power supplier is controlled by a Data Acquisition system (DAQ), which provides 0-10 V range analog signals for setting accelerating voltage and current, as well as it accepts digital and analog signals for monitoring the operative parameters of the tubes.

Different thickness filters are mounted on a wheel, whose rotation is provided by the motion of a stepper motor that in turn is controlled by a simple home-made bipolar drive circuit (based on L297 control logic chip and L298 power driver) that receives digital TTL signal as clock and direction inputs (it is controlled by a PC parallel port and/or by a data acquisition system).

4.2 Absolute dose-rate measurement.

The control of the radiation dose-rate DR is operated by a control of the x-ray tube current. A calibration relating x-ray acceleration current and dose-rate is necessary to perform accurate dosimetric measurements. The task to measure the absolute value of DR is assigned to the parallel-plate ionization chamber NE 2536/3C, which has a sensitive volume of 0.3 cm^3 and represents the reference detector for x-ray photons with energy up to 100 keV (for details see [2]). The ionization chamber is biased at 200V by the electrometer NE Dose Farmer 2670 that measures its current signal. The electrometer can then display the signal as a dose-rate or, integrating data with time, as

an absolute dose. The absolute dose-rate measurement section of the x-ray experimental setup is completely controlled by PC through a RS-232 port.
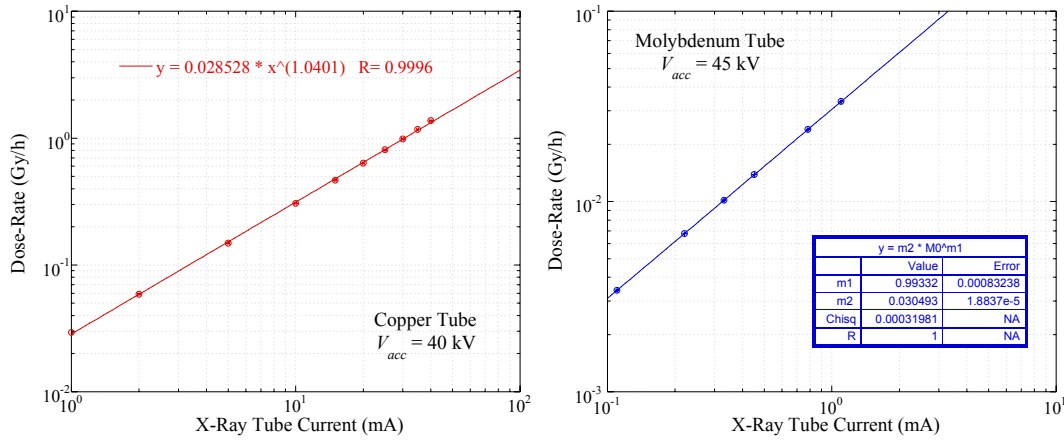

Fig. 4. 3. Calibration curves for copper (left) and molybdenum (right) tube.

Fig. 4.5 reports the calibration curves for the copper and molybdenum tubes used in this study for standard acceleration voltages and measured at the plane of the detector to be tested. The x-ray tube currents are a function of maximum supplied power, thus for the Cu-target tube can be varied up to 65 mA resulting in emitted radiation dose-rate up to 2 Gy/h, for the Mo-target one up to 1.3 mA with a maximum dose-rate of about 5×10^{-2} Gy/h.

4.3. Device-under-test motion system and centring.

The ionization chamber and the sample holder of the device-under-test (DUT) are axially constrained by a mechanical mounting. This means that their sensitive volume axially coincide. The beam centring procedure for x-rays is obviously more difficult than illuminating with visible radiation. For this reason, the DUT and ionization chamber are mounted on a motion controlled stage capable of moving them along the x-y-z axes with respect to the fixed beam position. Motion is assigned to micrometer resolution stepper motors (motion resolution is 40 nm/step) with a position feedback coming from optical encoders. The system is then controlled by PC via a proprietary National Instruments card containing the logic circuit and power drivers.

A specific home-made software has been developed that, once established the distance of the test plane from the x-ray beam collimator (z axis), performs a raster along the x-y axes with a defined

spatial resolution and collect the ionization chamber output signal to find the position that maximizes its intensity. The DUT will be mounted successively according to the beam centring position.

4.4 DC irradiation.

The x-ray beam produced by the vacuum tube, with possible spectral modifications operated by the primary and/or secondary filters, impinges on the DUT, which is connected by a series connection to a voltage source and to an ammeter (Fig. XXX). Under standard operations, bias conditions and current signal measurement are assigned to the pico-ammeter/voltage source Keithley 487, capable of a bias voltage in the range ±500 V, or to the electrometer Keithley 6517A, capable of supplying a bias voltage of ±1000 V. The maximum voltage to apply is the main discriminating element at the basis of the instrument choice for the specific measurement.
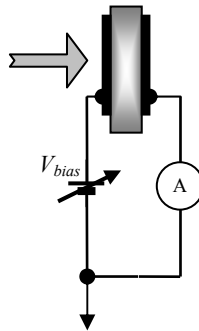

Fig. 4. 4

As ammeters, the two instruments differ in a larger resolution at very low currents (< 200 pA) and a general higher measurement accuracy of the model 6517A (see Table, where the accuracy is defined as a percentage of the reading plus a fixed uncertainty). The measurement uncertainty has been considered in each reading by a home-made software capable of remotely control the instruments through a GPIB bus.

Measuring Range	Resolution Keithley 487	Accuracy Keithley 487	Resolution Keithley 6517A	Accuracy Keithley 6517A
20 pA			100 aA	±(1% + 300 aA)
200 pA			1 fA	±(1% + 5 fA)
2 nA	10 fA	±(0.3% + 500 fA)	10 fA	±(0.2% + 300 fA)
20 nA	100 fA	±(0.2% + 3 pA)	100 fA	±(0.2% + 500 fA)
200 nA	1 pA	±(0.15% + 20 pA)	1 pA	±(0.2% + 5 pA)

2 μA	10 pA	±(0.15% + 200 pA)	10 pA	±(0.1% + 100 pA)
20 μA	100 pA	±(0.1% + 2 nA)	100 pA	±(0.1% + 500 pA)
200 μA	1 nA	±(0.1% + 20 nA)	1 nA	±(0.1% + 5 nA)
2 mA	10 nA	±(0.1% + 200 nA)	10 nA	±(0.1% + 100 nA)
20 mA			100 nA	±(0.1% + 500 nA)

Table 4. I

Voltage Range	Resolution Keithley 487	Accuracy Keithley 487	Resolution Keithley 6517A	Accuracy Keithley 6517A
±50 V	10 mV	±(0.1% + 4 mV)		
±500 V	100 mV	±(0.15% + 40 mV)		
±100 V			5 mV	±(0.15% + 10 mV)
±1000 V			50 mV	±(0.15% + 100 mV)

Table 4. II

Furthermore, signal transient measurements have risen the necessity to develop a very fast DC recording software that employs the internal memory of the instruments to temporarily store the readings, which successively are transferred altogether via GPIB bus under a cluster form. The fastest sampling rate is about 8 ms, corresponding to 125 readings/s for a resolution of 4½ digits.

4.5 AC irradiation.

The necessities related to the modulated (AC) dosimetric measurements can be synthetically described by:

- Exploiting the advantage of high signal-to-noise ratio (SNR) measurements typical of modulated irradiation measurements in conditions close to DC conditions (small modulation frequencies). In fact, independently on the detector leakage current, it is possible to mimic, under high-fidelity conditions, the behaviour of the device under radiotherapy standard conditions,

- Development during the last years of modulated sources for radiotherapy techniques (Intensity-Modulated Radiation Therapy, IMRT), which need detectors characterized by linear response at the variation of modulation frequency,

- Performing a transient analysis of detectors' response times.

- Signal phase analysis that allows the application of the Oheda's model [3] for evaluating the density of the states inside the diamond energy bandgap.

Besides the use of a lock-in amplifier, designed to accurately measure the modulated signal's module and phase, the measurement employs a high gain amplifier with the functionality of a current-to-voltage converter with characteristics of:

- Up to 10^9 V/A low-noise amplification,
- Ability to discriminate and to separate DC from AC signal.

4.5.1 X-ray shutter and mechanical chopper.

The x-ray beam can be modulated with a constant nominal frequency f of 4 Hz to 4 kHz by a mechanical stainless steel chopper. With its 2 mm thick wheel, modified for x-rays, the precision modulator acts as a high-pass filter for the photon energy, cutting-off the range under examination from about 8 to 45 keV (Fig. 4. 5). The modification of the wheel mass to completely absorb x-rays reduces the frequency range from about 2 to 800 Hz, which is our operative range.
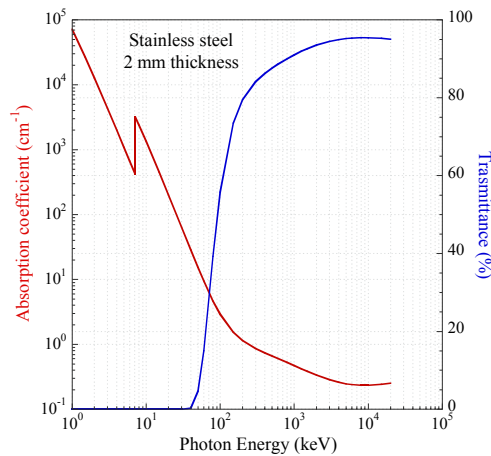
Fig. 4. 5

Photo transistors mounted on the chopper optically measures the modulation frequency by transferring their signal to the chopper controller. This latter can be manually controlled or remotely controlled by a voltage ranging from 0 to 10 V, which is proportional to the induced frequency. The analog signal controlling the chopper controller is provided by a DAQ connected to the PC. The controller sends a square-wave signal to the lock-in amplifier as a reference signal.

A 2 mm thick lead shutter is used to completely block the x-radiation both for safety operations and for performing signal transient analysis in case of on-off and /or off-on beam transitions. The

shutter transit time is about 0.5 ms, a value generally smaller than the dosimeters' rise and fall time. But, in case of comparable or even minor signal time, it will have to be take into consideration that the perturbation is not an ideal step function. The shutter control is provided by a relay operated by a TTL signal generated by a digital output DAQ module.

4.5.2 AC signal preamplifier.

The AC signal preamplifier has the task of amplifying the signal up to 109 times and of converting the current signal provided by the detector into a voltage signal, that is less sensitive to noise. The voltage signal is then sent to the input of a lock-in amplifier. Recent lock-in amplifiers are equipped by an internal, but more noisy, preamplifier in order to accept not only voltage signals, but current signals, too. Our choice has been to use two separate instruments to obtain the best performance from each one.
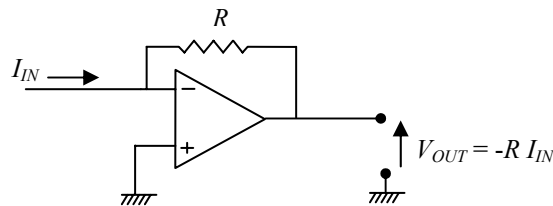

Fig. 4. 6.vuvtyd

The preamplifier is basically a simple trans-impedance amplifier, which basic circuit is described in Fig. 4. 6 by a simple inverting operational amplifier that accepts an input current and gives an amplified output voltage. This is an extremely simplified model, but for our discussion is sufficient to explain its operative functions. Two preamplifiers have been experimentally used: the Signal Recovery model 181 and the model 5182. The first is less noisy (see

Table 4. III) and allows a higher maximum gain than the model 5182 (10^9 V/A against 10^8 V/A). The model 181 has been chosen for normal characterizations. For high leakage current samples, the model 5182 has been used since it presents the additional DC output, which could be useful to monitor the detectors dark current. The limited bandwidth of high amplification factors is not a problem for our measurements, since, as previously described, is in turn limited to a maximum frequency of 800 Hz. On the contrary, it is related to the advantage of a low frequency low-pass filter that cuts possible higher frequency noise off.

Sensitivity (A/V)	Signal Recovery 181			Signal Recovery 5182		
	Bandwidth (kHz)	Input Impedance @ 100 Hz (Ω)	Noise current (fA/√Hz)	Bandwidth (kHz)	Input Impedance @ 100 Hz (Ω)	Noise current (fA/√Hz)
10^{-4}	200	<0.2	10^3			
10^{-5}	200	1.5	3×10^2	10^3	0.02	10^4
10^{-6}	100	10	10^2	5×10^2	0.2	5×10^3
10^{-7}	50	10^2	30	10^2	<10	135
10^{-8}	10	10^3	10	10	$<10^2$	45
10^{-8} low noise				2	$<10^3$	15
10^{-9}	1	10^4	3			

Table 4. III

4.5.3 Lock-in amplifier.

The lock-in amplifier is the key-instrument to perform accurate modulated measurements. By means of a signal modulation at a known frequency, the lock-in amplifier allows the measurement of signals characterized by a module less than the noise level and far minor than a DC measurement. The technique allows the determination of the only photocurrent and a valuable estimation of the kinetic detector behaviour in terms of response times.

The operative function of lock-in amplifier is related to the assumption that the noise module depends on the bandwidth of the measurement system: since this dependence for all electronic amplifiers at low frequencies f is of the type f^{-1}, the lock-in amplifies the signal only in a very narrow band around the modulation frequency.

Fig. 4. 7 shows a schematic drawing of the functional diagram of the lock-in amplifier. It can be divided into the reference and input signal channels. Reference signal passes through a discriminator and into a phase-locked-loop (PLL), which is able to lock the phase of the input signal and follow its possible variations. The phase dynamic locking is fundamental since phase fluctuation induces variation of output signal module. The signal passed through the PLL is then dephased of $\pi/2$ to obtain the discussed signal components. Signal to be measured passes through sharp notch filters working at 50 and 100 Hz that can be successively activated to cut-off the electric network noise. It is then amplified and compared to reference dephased signals.
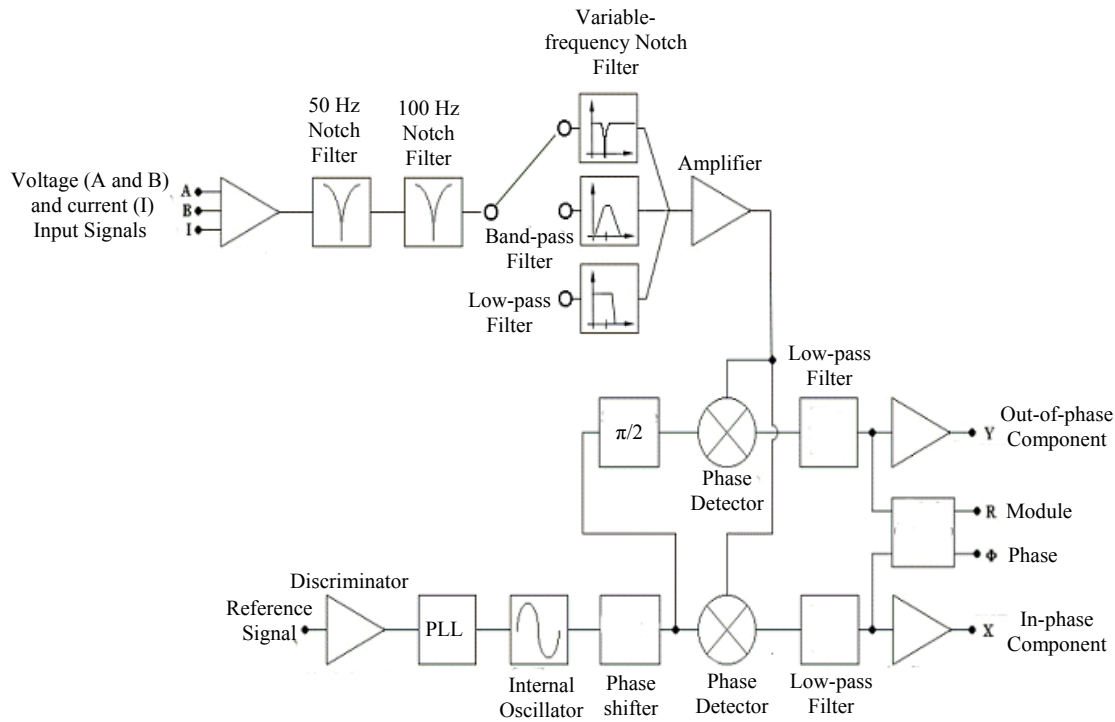
Fig. 4. 7. Operative diagram of a lock-in amplifier.

At this point, the amplifiers locks the modulation frequency by a heterodyne demodulation. Remembering that the time product between two sinusoidal signals of frequency f_1 and f_2 is a signal composed by two harmonics of sum frequency $(f_1 + f_2)$ and difference $(f_1 - f_2)$, the lock-in amplifiers input signals are the reference and the one to be measured. Considering two signal with equal frequency, we obtain a doubled frequency signal and a DC component depending on the phase delay between the signals. The output signal module depends on its phase shift to the reference one φ. It is necessary to dephase the reference phase of the known quantity φ, in ordre to maximize the output module, or measure the output signal at two phases with difference of $\pi/2$ (in-phase and out-of-phase components).

After that signal passes through the final low-pass filter that transform the signals into DC ones. Its task is decisive, since it has to have a very narrow-band and has to be very sharp (20 or 40 dB/dec) since, acting on the DC, it could introduce low-frequency noise (noise amplitude is of the type f^{-1}).

Some words have to be spent about the dynamic reserve, defined as the ratio between signal amplitude at modulation frequency and noise amplitude at different frequencies without saturating the input amplifier. We use as lock-in amplifier the Signal Recovery model 7265DSP that has a

dynamic reserve of 100 dB, namely it allows to discover signals of interest 10^{-5} times smaller than the noise amplitude.

References.

1. Ascarelli, P., et al., *CVD diamond dosimetric response evaluated by X-ray absorbers method.* Diamond and Related Materials, 2003. **12**(3-7): p. 691-695.
2. Albuquerque, M.P.P. and L.V.E. Caldas, *New Iionization Chambers For Beta And X-Radiation.* Nuclear Instruments and Methods in Physics Research A, 1989. **280**: p. 310-313.
3. Oheda, H., *Phase-shift analysis of modulated photocurrent: its application to the determination of the energetic distribution of gap states.* Journal of Applied Physics, 1981. **52**(11): p. 6693-6700.

Chapter 5.

Evaluation of Dosimeters Performance

The present Chapter deals with the experimental results obtained by the developed x-ray dosimeters. Starting from the characterizations before the irradiation, a compared analysis between optical-grade and electronic-grade based dosimeters has been continuously performed. Together to a discussion about the pre-activation, dosimeters DC performances have been compared in terms of sensitivity, signal-to-leakage ratio, linearity with radiation dose-rate. Transient evaluation and modulated irradiation have been fundamental tools to evaluate dosimeters' dynamic response.

5.1. Pre-irradiation characterization.

A pre-characterization of developed dosimeters was performed to analyze in depth their electronic properties and the possible influence of electrically active defects, that could play a key role in the detection of x-radiation. This qualification phase is based on the use of two techniques: analysis of current-to-voltage characteristics to determine the charge transport mechanism and evaluate the metal contacts' behaviour, and spectral photoconductivity method to excite and individuate possible defect states energetically positioned in the diamond energy bandgap.

5.1.1 Electric resistivity and leakage current.

Electrical contacts on diamond films have been developed as described in Paragraph 3.3.3, therefore:

- optical-grade (OG) films present annealed titanium contacts;
- electronic-grade (EG) films present a diamond-like-carbon(DLC)/platinum/gold multilayered contacts.

The ohmic behaviour of all the contacts is confirmed by the linear current-to-voltage (I-V) characteristics measured on the sandwich-configuration samples. In Fig. 5. 1, two typical examples of I-V characteristics are shown for each type of diamond film. Remembering that

- the leakage current density J_d is defined as the leakage current I_d per unit of transversal surface to current flow direction ($J_d = I_d / A$),
- the applied electric field E is the ratio between the bias voltage and the distance between the electrodes (in our case the film thickness d),
- that current density and electric field are related, under ohmic conditions, by the equation

$$J_d = \sigma E \,, \tag{5.1}$$

where σ is the material conductivity, which is the reciprocal quantity of resistivity ρ,

we observe that electronic grade samples show values of current density far smaller that those of optical-grade films.
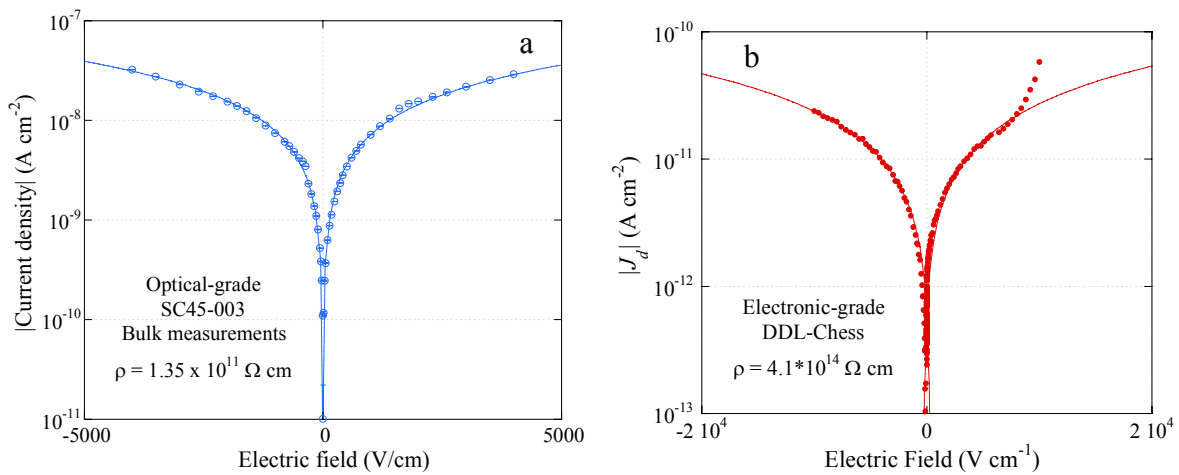

Fig. 5. 1. Typical J-E characteristics of a) optical-grade and b) electronic-grade films.

This is related to a sensible difference in the mean electrical resistivity among all the analyzed samples: $(5.0 \pm 1.5) \times 10^{14}$ $\Omega \cdot cm$ against $(1.5 \pm 0.5) \times 10^{11}$ $\Omega \cdot cm$, which is about a factor of 3000. In radiation detectors, the leakage (or dark) current has a negative role, since it affects the photogenerated signal by partially hiding it. Since the signal of interest is evaluated by performing a differential analysis and the signal uncertainty level depends on the amplitude of the element to subtract, the ideal detector should have a zero leakage. Under this point of view, EG diamond films have to be considered almost intrinsic crystals and have to be preferred to OG ones. But the electrical resistivity is not the only parameter to consider.

On the other hand, some EG films have a sharp increase in current at high bias voltages V_{bias} (> 350 V, corresponding to electric fields of 7×10^3 V/cm), probably due to the reaching of conditions of space-charge limited transport (Fig. 5. 1b). Under such conditions, the current is proportional to V_{bias}^{n}. If $n = 2$ we find the Mott-Gourney law [1], which can be considered as a first-order approximation for this kind of transport [2]. The minimum bias voltage inducing space-charge limited transport varies slightly from sample to sample, but its value is very well reproducible in the same film. Since the described condition occurs asymmetrically with respect to bias voltage, we believe that some uncontrolled parameters during the contacts deposition process and/or defects present in the DLC layer could be responsible of it.

5.1.2 Spectral photoconductivity measurements.

Spectral photoconductivity technique is a useful tool for semiconductors to perform an analysis of the distribution of density of states within the energy bandgap. A monochromatic radiation, whose wavelength can be changed from visible to UV, is modulated by a chopper and impinges on the sample and excites all the possible transition between occupied states by carriers to free states able to accept them.

Such transitions can be of three types depending on the incident photon energy:

1. from valence band extended states to conduction band extended states,
2. from valence band extended states to localized defect states in the bandgap,
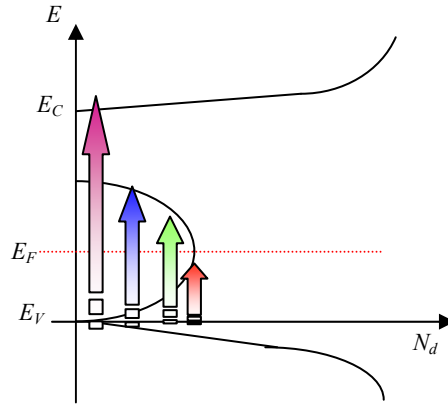3. from localized defect states in the bandgap to extended states in conduction band.

Fig. 5. 2. Sketch of the action of monochromatic radiation that is able
to excite electronic transitions as a function of its wavelength.

The described mechanisms imply the final presence of a free carrier in conduction or valence band that can drift towards the respective electrode. Transitions from localized defect states to other defect states do not contribute to the conduction, since no charge carrier (hole or electron) can be collected in valence or conduction band. Fig. 5. 2 reports a simplified sketch of the excitation mechanisms at variable wavelength in a defected semiconductor in which the valence band maximum energy is indicated as E_V, the minim energy of conduction band as E_C, Fermi level as E_F, the density of states is N_d.

By measuring the photocurrent at the variation of radiation wavelength, it is possible to evaluate the intensity of the jointed effect of all the described transitions, thus obtaining the so-called joint density of states, as well as to measure the semiconductor bandgap.

A useful physical quantity in spectral photoconductivity is the quantum efficiency η, that is independent of the impinging radiation beam intensity and is defined as

$$\eta(hv) = \frac{I_{ph}(hv)}{P_{opt}(hv)} \frac{hv}{q} , \qquad (5.2)$$

where I_{ph} is the photocurrent, q the elementary charge, P_{opt} and the hv the radiation power and energy, respectively. Quantum efficiency represents the fraction of generated charge carriers respect to the number of photons impinging on the material and is proportional to the material absorption coefficient. Quantum efficiency is also proportional to the convolution function between the density of states initially occupied by carriers g_V and free states g_C weighted by the transition matrix $R(hv)$:

$$f(hv) \propto hv R^2(hv) \int_{E_F}^{\infty} g_V(E - hv) g_C(E) dE . \qquad (5.3)$$

The function $f(hv)$ is exactly the joint density of the states. A semiconductor as our diamond films probably present energetically shallow and deep-states in the bandgap which control the

Fermi level. Possible deformation of the carbon atom bonds and phonon interactions could induce the formation of an Urbach tail just close to valence band, which depends on quantum efficiency according to the exponential relation $\eta \propto \exp((h\nu - E_G)/E_0)$, being E_G the energy bandgap and E_U the Urbach energy which represents the Urbach tail width. The described picture of states inside the bandgap by simulation is shown in **Fig. 5. 3**.
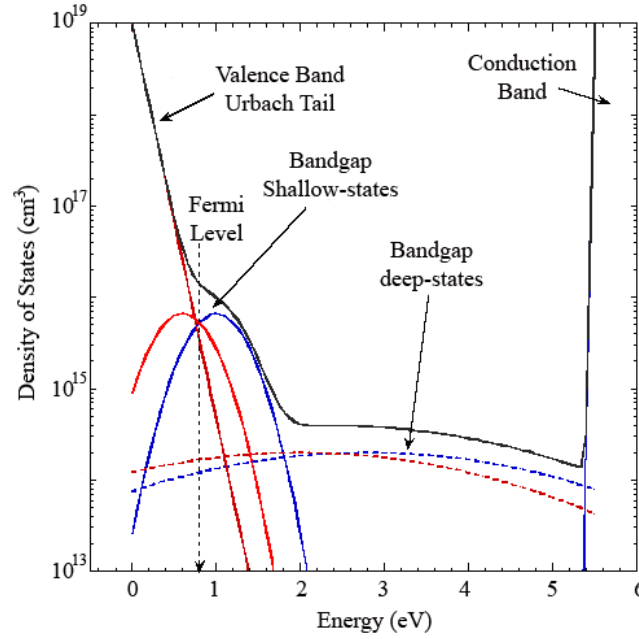

Fig. 5. 3

Spectra obtained with our OG and EG samples furnish clear evidences (**Fig. 5. 4**). Both materials point out a quantum efficiency maximum in correspondence of the bandgap energy (5.5 eV). The maximum value is 1 for EG films, is about 0.2 for OG ones. It means that for an over-bandgap radiation, reasonably supposing comparable absorption coefficients, not all the photogenerated charges in OG films succeed in reaching the electrodes. This is an indication of the presence of trap defect states.

At photon energies larger than bandgap, η decreases owing to surface recombination. Surface recombination occurs because the penetration length of radiation inside diamond is minor than 1 μm for $h\nu > 5.5$ eV, thus a large charge density with a predominant electron-hole scattering is obtained. This hampers charge carriers to be collected by the electrodes and reduces photocurrent.

If, instead of a sandwich structure which force a type of photogenerated carrier to travel across all the film thickness, it is produced a planar structure with contacts disposed on the illuminated film surface, surface recombination effect reduces (**Fig. 5. 4**a). This can be explained by

considering the disposition of the electric field lines, which more efficiently enable carriers to move towards the electrodes.

EG samples suffer slightly less than OG ones from surface recombination, since the quantum efficiency reduction from 5.5 to 6.0 eV is meanly equal to about 1 decade against the 1.5 – 2 decades typical of OG samples. This consideration can be explained that also surface defect states contribute to the trapping of charges and is confirmed by the slight difference in quantum efficiency provided by the two film surfaces in planar configuration.

Both EG and OG films present an Urbach tail characterized by an Urbach energy of (40 ± 12) meV and (97 ± 15) meV, respectively. This is an indication of less deformed lattice bonds and minor interaction with crystal phonons. Urbach tail is not the only contribution in the zone close to bandgap energy, but it is present another small contribution that could be caused by shallow traps.
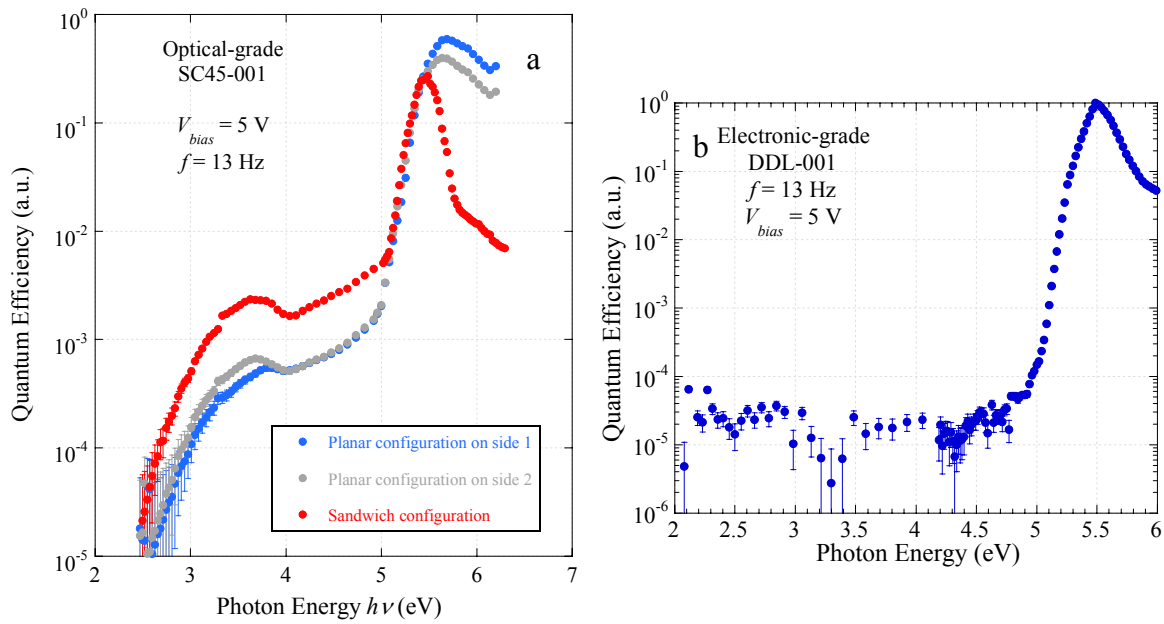

Fig. 5. 4. Typical photoconductivity spectra of a) OG samples for sandwich and planar configuration on both film surfaces and b) EG samples.

Inspecting inside the bandgap, it is apparent that OG films show a broad defect level centred at photon energy of about 3.8 eV. Remembering that nitrogen substitutional atoms in diamond contribute to a defect energy level of 1.7 eV from the bottom of the conduction band (Paragraph 2.3) and that OG samples have a nominal N concentration <1 ppm (about 2×10^{17} cm^{-3}, see Paragraph 3.1) it is very probable that this peak (positioned at energy $E_G - 3.8\,eV = 1.7\,eV$) is related to the excitation of substitutional nitrogen. On the contrary, EG films point out a negligible presence of deep-traps within the CVD diamond energy bandgap, with flat under-bandgap spectra,

as shown in **Fig. 5. 4**b. Furthermore, a discrimination ratio of 5 decades between UV photon energy at bandgap to visible light can be evaluated. All these evidence are coherent with nitrogen and boron concentrations of about 9×10^{14} cm^{-3} and 2×10^{14} cm^{-3}, respectively.

Spectral photoconductivity technique fortifies a picture of defected OG films presenting deep-traps and of EG films apparently lacking of defects in the bandgap. Both show phonon interactions caused by crystal lattice distortions evidenced by the Urbach tail and may suffer from the action of shallow-traps.

5.2 Priming process.

The necessity of a *priming* or activation process connected to the use of diamond dosimeters is mainly determined by the need of obtaining reproducible stationary conditions for the provided signal. Priming is observed during the early stages of exposure and is attributed to trapping of charges within the diamond sensor. The reasons related to the necessity of the priming process can be attributed to the diamond defects that are energetically positioned as deep traps in the band-gap. They have to be electrically filled by photo-generated charge carriers to reach a condition of passivation. Owing to their high energetic difference from the Fermi level, conduction band minimum and valence band maximum, their rate of thermal ionization is low and they remain passivated for long periods of time. Polycrystalline CVD diamonds kept in the dark have been observed to remain primed for months, while exposure to room light ionizes the traps, resulting in a rapid de-priming [3] [4].

A diamond dosimeter has to be pre-irradiated before first operation and then kept in the dark to preserve its electronic stability and to get a stable current response during successive operations. All diamond detectors for ionizing radiation developed up to now suffer of priming, including the commercially available natural diamond ones [5]. In contrast to this, the only article demonstrating the non-necessity of priming has been reported for a natural diamond dosimeter [6], but this has been an exception probably caused by the non perfectly equal properties of geological stones, as declared by the same authors.

The main effects produced by priming on the performance of diamond detectors are:
- a collection efficiency enhancement (increase of charge carriers mobility-lifetime product) that causes an increase of the photocurrent. It means that photo-generated charges travel an

increased drift distance and a larger amount of them succeed in reaching the electrodes. The primary effect of priming can be evaluated as positive for detector performance.

- A concomitant stabilization of the dark current, generally at higher values than the un-primed condition. This unavoidable and negative effect can be explained by considering that charges trapped by priming process can contribute to the leakage transport by voltage-induced thermionic emission and hopping [7, 8].

The dose needed to complete the priming process is defined as priming dose. After a typical priming dose of about 10 – 50 Gy (depending on the diamond deep-traps defect density), a stabilization of the photo-response is achieved.
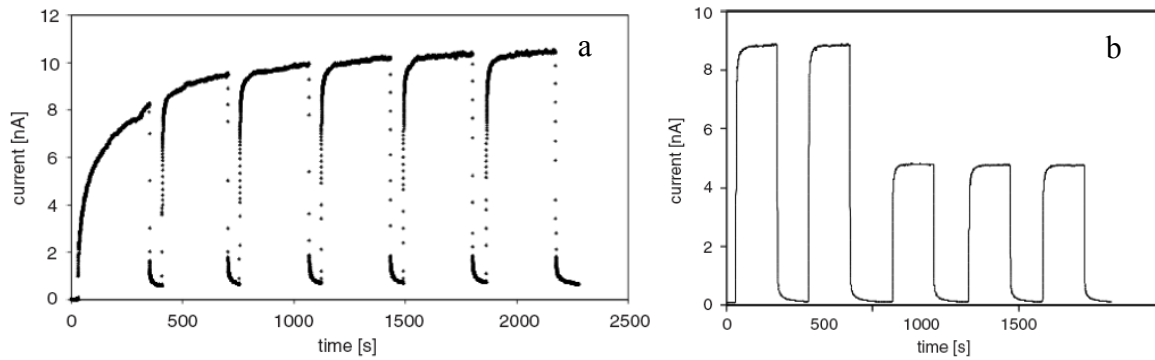
Fig. 5. 5. Photocurrent provided by a dosimeter a) during the priming process and b) once priming is completed [5].

In our characterization setup, the activation process consists of a prolonged irradiation of the device under the unfiltered x-ray beam in order to increase the radiation dose-rate and consequently to decrease the activation time.

5.2.1 Priming process in optical-grade samples.

Dosimeters developed starting from optical-grade single-crystal diamond are affected by priming effect. **Fig. 5. 6** clearly shows that, during priming process performed under a modulated radiation dose-rate of 0.5 Gy/h, the signal increases from the time of the shutter opening until it saturates after about 4 hours, corresponding to a priming dose of about 2 Gy. According to this value, the deep defects in the bandgap are active, but their density is not so high if compared to those in literature [5].

For OG-based dosimeters, the signal has a mean increase of 7 - 8 times during the priming process, while dark I-V characteristics generally seem not to be affected by the pre-irradiation. An interesting notation can be done on the qualitative evolution of the signal phase, which decreases until it presents a minimum value of -59.3 degrees. This minimum corresponds to a signal amplitude flex. After that the phase increases up to saturating. The correlation of this mechanism to physical reasons is at present under study and will be clarified in the future.
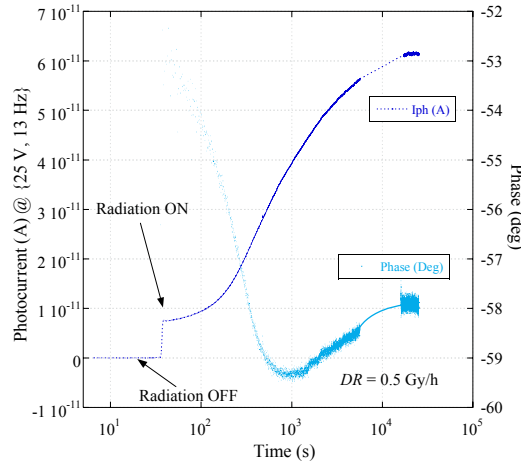
Fig. 5. 6

Once priming has been completed, the dosimeter shows a fast response (in the range of tenths of seconds, see Paragraph 3.4.4) to variations of irradiation intensity, reproducible and stable with time.
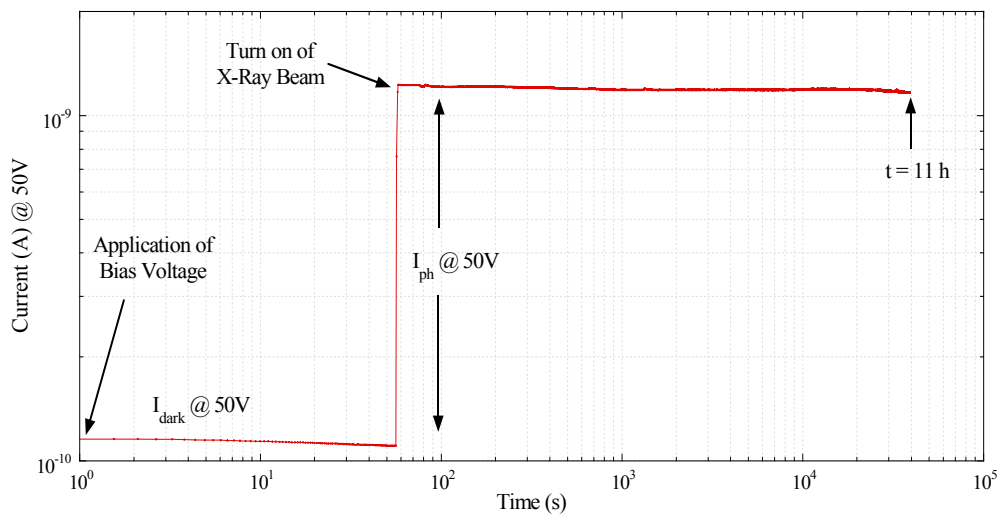

Fig. 5. 7

5.2.2 Priming process in electronic-grade samples.

The main novelty related to the development of electronic-grade diamond dosimeters is that they do not suffer from priming. This is an enormous advantage since under operative conditions, the necessary prolonged activating irradiation can be avoided and the detectors are immediately ready to monitor high-energy ionizing beams.

Fig. 5. 8 demonstrates the stability of the AC photo-signal amplitude (I_{ph-ac}) and phase during the priming process under condition of slow x-ray beam modulation, able to mimic DC conditions. Similarly to OG samples, the I_d-V_{bias} characteristics do not change after priming process (not shown).

These results confirm the very low electrically-active defect density of the films and represent a very important innovation goal of this thesis.
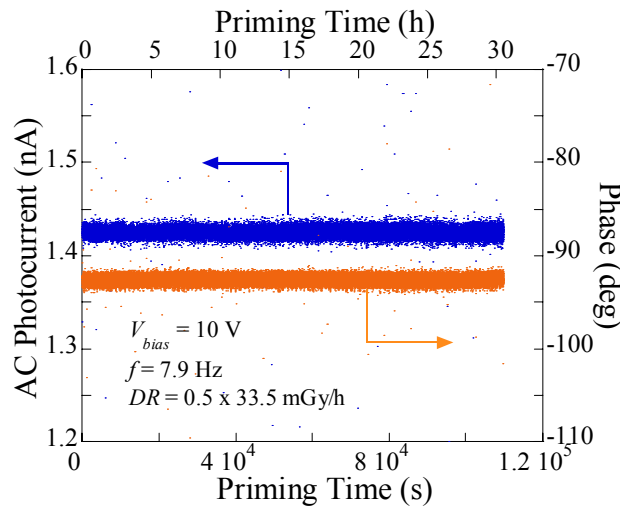

Fig. 5. 8

5.3 Photo-detection model.

The model we propose is based on the charge induction process: a semiconductor, subjected to an excitation process which creates excess charge carriers and subjected to the application of an external electric field, produces a current pulse proportional to the path of charges induced towards the electrodes.
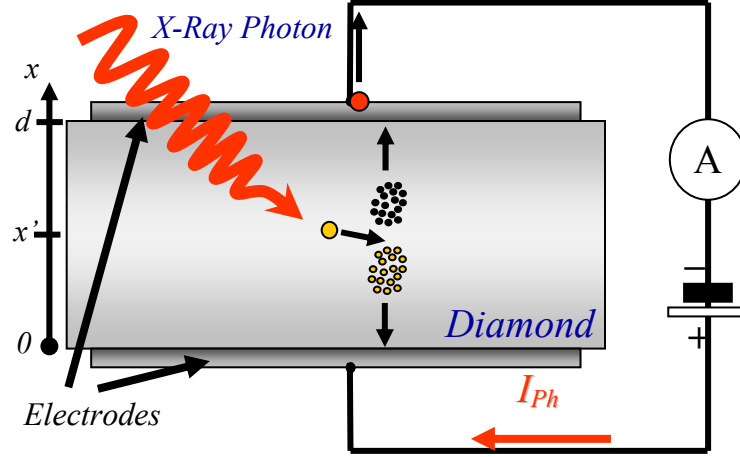

Fig. 5. 9. Schematic summarizing the mechanism involved in of the photodetection model. An x-ray photon impinging on the detector is absorbed. By photoelectrical effect (in our case for x-ray photon energy <50 keV) it produces a very hot electron that in turn produces a swarm of electrons (yellow) and holes (black) meanly at half crystal thickness. The produced charge carriers are attracted by the respective electrode and their motion produces a current pulse that can be measured by the ammeter situated in series with the bias generator.

Furthermore, a device, made of a high electric resistivity semiconductor, structured in a *sandwich* configuration with thickness d, acts as a parallel plate capacitor with a parallel large resistance, whose value is decreased during irradiation. If the excitation is a ionising radiation producing $Q_{ionised}$ excess carriers uniformly in the semiconductor (like an x-ray beam), we define $Q_{collected} = Q_{collected}^n + Q_{collected}^p$ as the excess charges effectively collected to the electrodes. It can be defined a collection efficiency for such a device[9]:

$$\eta_C^{n,p} = \frac{Q_{collected}^{n,p}}{Q_{ionised}} = \frac{L_C}{d}[1 - \exp(-\frac{d}{L_C})] \tag{5.4}$$

where $L_C(V) = \mu \tau V_{bias} / d$ is defined as the collection length for electrons and holes, being V_{bias} the bias voltage, μ and τ mobility and lifetime of the charge carriers, respectively. The collection efficiency defined in (5.4) is the Hecht's equation [10], frequently used for describing photo-conduction phenomena in semiconductors. Several shortcomings may be enumerated in the use of

the Hecht relation. One significant shortcoming is the inherent assumption that the amplitude of the signal generated is proportional to the induced charge in the detector. In addition, uniform electric field and charge trapping in the diamond crystal lattice are assumed in the Hecht's formulation.

The induced total photocurrent density is expressed as

$$J_{Ph}(V) = qG_0 d \eta_c(V) \tag{5.5}$$

where G_0 is the generation rate, namely the volume concentration of generated carriers per unit time, that is proportional to the radiation dose-rate. The photocurrent expression (5.5), largely influenced by the L_C / d ratio, can be simplified for the two limiting cases, as:

$$J_{Ph}(V) = qG_0 \mu\tau V, \quad L_c < d \tag{5.6}$$

$$J_{Ph}(V) = qG_0 d / 2, \quad L_c >> d . \tag{5.7}$$

The ideal dosimeter has to assure the linearity between the physical observable, the signal generated by the radiation and the quantity to be measured, namely the exposure absorbed dose-rate, which is the absorbed energy per unit time and unit mass and is proportional to G_0. Due to the process of carrier generation, we suppose that the absorption of the radiation dose can be totally ascribed to the photoelectric effect, with a mechanism consisting in a sudden elastic transfer of energy from photon to the material and successive cascade transfers up to the generation of low energy carriers (Fig. 10). In such a way, the condition of linear response is reduced to the proportionality between the recorded signal and G_0.

Apparently, Eq. (5.6) could only show a limited range of a linear behaviour of the response, because it is well-known that, for a distribution of trap levels in the energy gap and for high generation conditions, carrier mobility or lifetime may be function[11] of G_0: as a consequence the photocurrent cannot be considered in the whole range proportional to the radiation absorbed dose-rate. On the other hand, the conditions evidenced by Eq. (5.7) seem to be the only one able to guarantee a linear relationship, defining the collection length much greater than d as the optimal working condition for a detector capable of linear response. Practically, once fixed the material properties modifying the deposition parameters, the only variable parameter able to induce an increase of the collection length in order to ensure the linearity is the increasing of bias voltage. Moreover for transversal working devices, the design of thin thickness implies two advantages: the application, at a fixed voltage, of a higher electric field and the minimization of the contact distance, both factors that concordantly contribute to reach the condition $L_C >> d$.

It is very interesting to note that the detector emulates the working mechanisms of a parallel plate ionisation chamber, since the applied voltage influences the collection efficiency of the excess charges and consequently the response signal. In fact, both for the described detector and for the

ionisation chamber, at low voltage, the excess charges can recombine and cannot reach the electrodes, while at sufficiently high voltages, the excess carriers gain a considerable drift velocity, succeeding in reaching the electrode. The ionisation chamber works in that region, a region that ensures a unitary collection efficiency, when the signal saturates and it does not depend anymore on the applied voltage, condition necessary and sufficient for a linear response.

5.4 Characterization by continuous irradiation (DC).

The characterization of a detectors performance under continuous irradiation conditions (DC) is particularly important since it represents the standard operative mode in several medical applications. It is divided into the analysis of photocurrent dependence on bias voltage, on leakage current and on radiation dose-rate. A brief transient analysis closes the paragraph.

5.4.1 Photocurrent and signal-to-leakage ratio.

Dark current to bias voltage characteristic curves of the studied samples have been examined in paragraph 5.1.1. The DC net photocurrent I_{ph-dc} results from the difference between the total current measured under irradiation I_{x-ray} and the dark current I_d:

$$I_{ph}(V_{bias},\, DR) = I_{x-ray}(V_{bias},\, DR) - I_d(V_{bias}).$$

(5.8)

In Fig. 5. 10a the total current under irradiation and the dark one are shown as a function of the bias voltage (they refer to a OG sample). Applying Eq. (5.8), the net photocurrent I_{ph-dc} can be derived and it is shown in Fig. 5. 10b. Net photocurrent may have a slight asymmetrical divergence as a function of bias voltage sign, which is indicative of small geometrical differences in the contacts and/or small differences in their contact resistance.
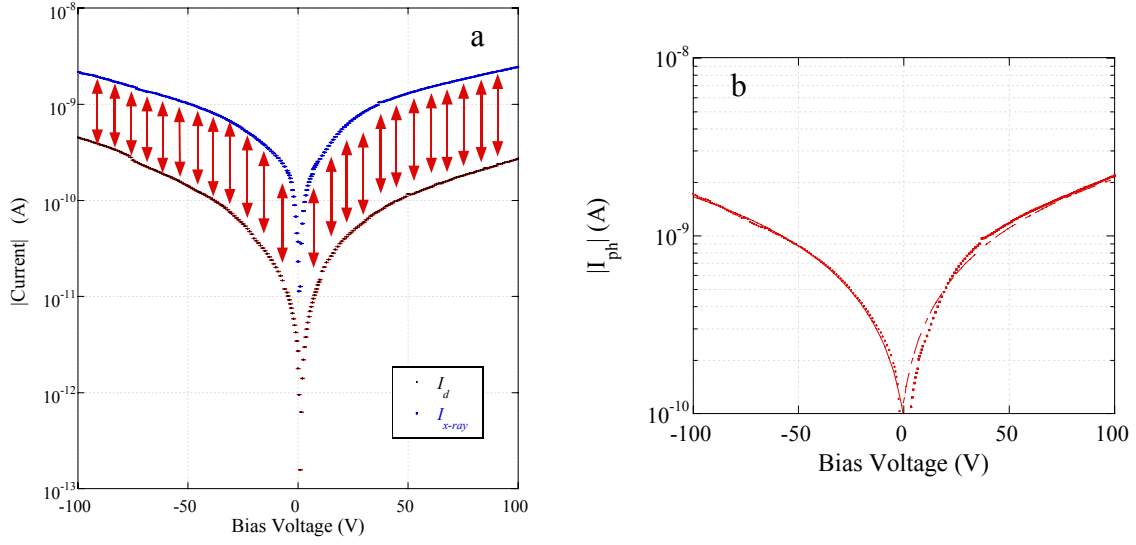
Fig. 5. 10

An important parameter to evaluate the detector capability to discriminate the signal from the "noise" leakage is the signal-to-leakage ratio, defined as $|I_{ph}|/|I_d|$. **Fig. 5. 11**a shows a typical pattern of the $|I_{ph}|/|I_d|$ value on bias voltage. The maximum values of this ratio is obtained for a bias voltage of about 5 V (in the case shown, about 73 for a radiation dose-rate of 1.374 Gy/h, while this value is about 2.5 for a dose-rate of 0.029 Gy/h). Two trends are apparent: an increase of $|I_{ph}|/|I_d|$ from 0 to 5V, after that the signal-to-noise ratio decreases according to the phenomenological power low $|I_{ph}|/|I_d| \propto V_{bias}^{-\beta}$, where β is <1.
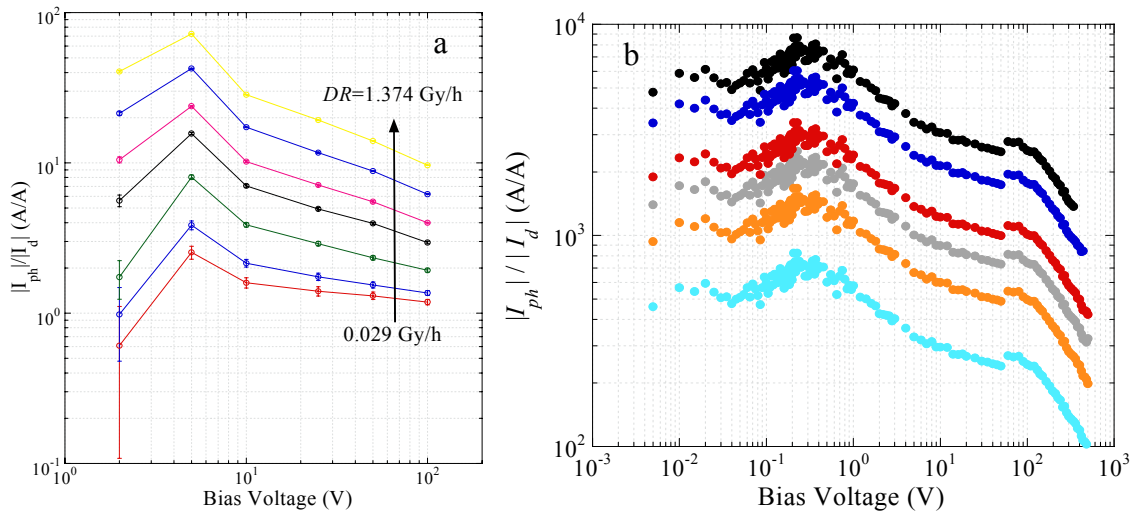

Fig. 5. 11

Electronic-grade samples (**Fig. 5. 11**b) show a far larger signal-to-noise ratio, almost 10^4 for a radiation dose-rate of 0.0335 Gy/h. They take advantage from a leakage current far lower than that of OG ones. But an additional reason is in the charge collection capability of the different samples, which is a function of the diamond film quality. All the curves shown in **Fig. 5. 11**b denote that maximum values are obtained for lower bias voltages than OG samples (between 0.3 and 0.4 V), after that a power law decrease describes the trend up to 100 V. For $V_{bias} > 100$ V, we assist to a sharper decrease of $|I_{ph}|/|I_d|$ values due to the concomitant tendency to a saturation of the photocurrent facing an ohmic increase of the dark current.

In **Fig. 5. 12** the $I_{ph}(V_{bias}, DR)$ for an EG dosimeter are reported. The curves agrees with Hecht model and are thus fitted by Eq. (5.4). The value of the $\mu\tau$ product can be evaluated as a fit parameter. It has been found that for EG samples, this value is about 3×10^{-5} cm^2/V, while for OG samples has been estimated of one order of magnitude less.
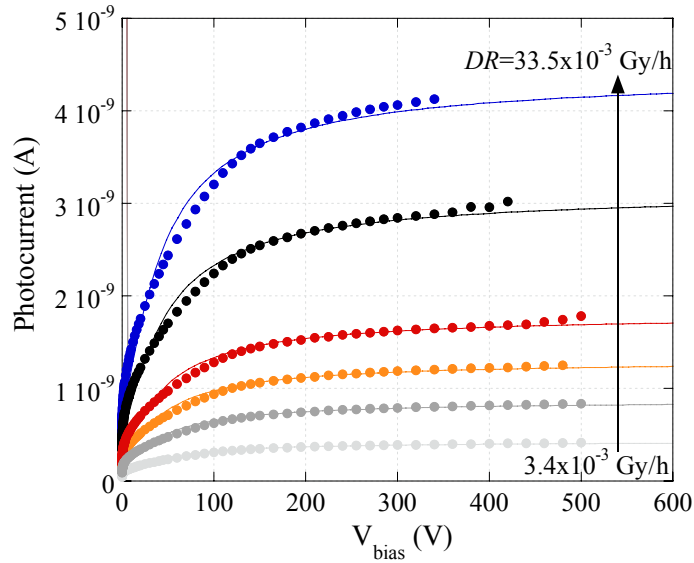

Fig. 5. 12

5.4.2 Signal stability and fluctuations.

The signal provided by both the two types of x-ray dosimeters is very stable with time, as also shown in **Fig. 5. 7** and **Fig. 5. 8**. Possible large fluctuations can occur, but they are due to source intensity fluctuations, which are properly recorded together with the related signal.

The signal reproducibility is very high. The signal fluctuations, defined as the variation of readings ΔI_{ph} accumulated in time and during multiple experiments, performed under the same conditions, with respect to the mean photocurrent value I_{ph}. **Fig. 5. 13** shows the percent value $\Delta I_{ph}/I_{ph}$ as a function of bias voltage and radiation dose-rate, which influence the signal intensity. Although we are not able to find a defined trend, it is possible to qualitatively observe that the signal fluctuations are always below 0.5% and are a decreasing function of bias voltage and DR. This appears clear, since they induce an increase of the signal, by reducing the related uncertainty.

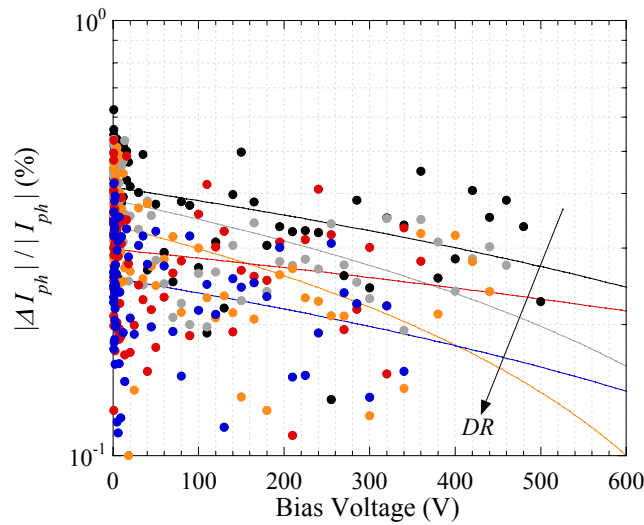**Fig. 5. 13** refers to EG samples, but the intensity of the fluctuations is comparable to OG samples.

Fig. 5. 13

5.4.3 Dosimetric evaluation.

The dosimetric characterization is performed under continuous x-ray irradiation by varying the radiation dose-rate *DR* and the bias voltage applied to the detector. Fowler's model [12] predicts that the dose-rate linearity for insulating materials is affected by charge trapping centers. He stated the dose rate linearity as

$$\sigma \propto DR^{\Delta}, \qquad (5.9)$$

where σ is the electric conductivity of the solid-state detector at the radiation dose-rate *DR* and Δ is the linearity coefficient, generally ranging from 0.5 to 1.5. An ideal dosimeter is characterized by the condition $\Delta = 1$ with a defined uncertainty of 1%. According to this model, $\Delta = 0.5$ for pure material with no traps or when the excitation rate is so high that trap concentration becomes negligible with respect to the photogenerated charge carriers. If all the traps have the same capture cross section, $0.5 < \Delta \leq 1$. A uniform and quasi-uniform trap distribution over a range of depths in the bandgap leads to $\Delta \cong 1$. If traps are present with different cross sections, it may exceed 1. The presence of trapping centers also reduces the lifetime of charge carriers by the ratio of the number of trapped electrons to the free carrier density. To investigate this, the value of Δ can be found from the gradient of a log-log plot of the I_{ph-dc} (*DR*) experimental data, according to the following relation derived from Fowler's one:
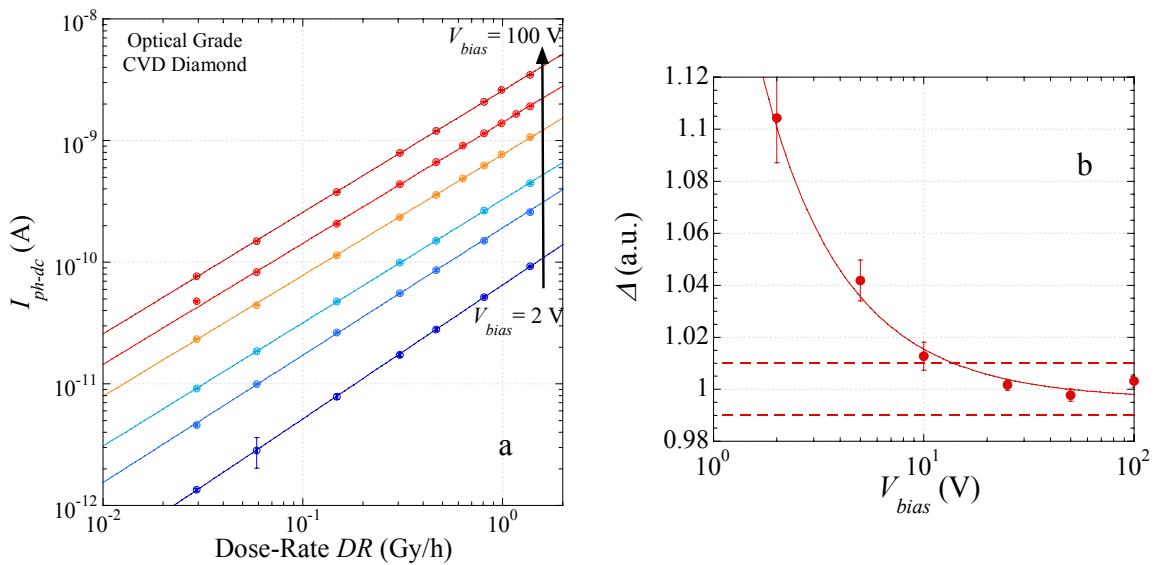
$$I_{ph-dc} \propto DR^{\Delta}. \qquad (5.10)$$

Fig. 5. 14

Optical-grade dosimeters.

OG dosimeters present a well-defined dose-rate linearity operative region. As discussed, this condition paradoxically is not obvious by using single-crystal films. In fact, $\Delta = 0.5$ is the expected value for an intrinsic pure photoconductor, without electronic states acting as recombination centers (bimolecular regime), while $\Delta = 1$ indicates the presence of states inside the forbidden band-gap acting as recombination centers (monomolecular regime). The specific films contain a defect density characterized by a broad energy level situated at 1.7 eV under the conduction band minimum, that was evidenced by spectral photoconductivity measurements, and may have fast shallow traps. Such traps are defined fast since their energetic distance from the diamond bands is comparable to the thermal energy kT. Therefore, they are able to trap charge carriers and release them by thermionic emission with a high frequency.

Fig. 5. 14a shows the signal dependency on *DR* as a function of bias voltage. The patterns are coherent with Eq. (5.10). Fig. 5. 14b shows the values of Δ, derived as a fit parameter, as a function of bias voltage. The linearity region is defined by $\Delta=1 \pm 1\%$. At low V_{Bias} the dosimeter response is over-linear. This behavior was observed in materials characterized by presence of traps with different cross sections. Increasing V_{Bias}, the dosimeter signal satisfies the dose linearity condition ($V_{Bias} > 10$ V), reaching $\Delta = (1.0017 \pm 0.0011)$ for $V_{Bias} = 25$ V (with a corresponding electric field of 500 V/cm). Even at higher V_{Bias} than 25 V, the signal remains abundantly within the required dosimetry range and the dosimeter behaves like a ionization chamber. In this case, the phenomenological relation of the $\Delta(V_{Bias})$ function seems to be $\Delta = \alpha V_{bias} / \left(\beta + V_{bias} \right)$, where α and β are constants.
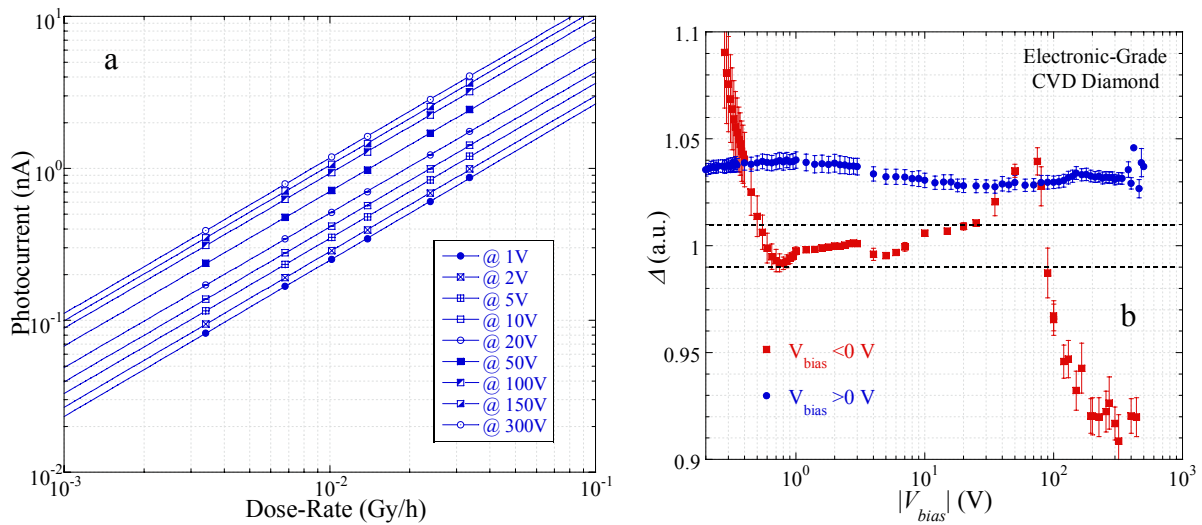

Fig. 5. 15

Electronic-grade samples.

The developed dosimeters show an approximately constant Δ = 1.02 ± 0.01 over the explored positive voltage range (**Fig. 5. 15**). In fact, at negative voltages the dosimeter provides a slightly over-linear response to radiation dose-rate (Δ ranges from 1.025 to 1.040). For negative voltages the signal is directly proportional to *DR* in the range $0.5 \leq V_{bias} \leq 20$ V and thus the detector acts as an ideal dosimeter.

In this voltage range the signal-to-leakage ratio is almost constant (about 3.0×10^3 at *DR*≈0.033 Gy/h), coherent with an ohmic dependence both of $I_{ph\text{-}dc}$ and I_d. For $V_{bias} < -20$ V the dosimeter is not linear (an over- to sub-linear transition usually takes place at about 90V).

Concluding, EG dosimeters provide a response perfectly proportional to the radiation dose-rate only in a limited operative region.

5.4.4 Transient DC analysis in optical-grade samples.

In Fig. 5. 16 it is shown the signal transient, induced by irradiating an OG sample according to a step-function (off-on) dose-rate variation. In Fig. 5. 17a signal rising time τ as a function of V_{Bias} is reported. Two different operative regions, related to two different mechanisms, are evident. By increasing V_{Bias} the device gets faster up to voltages of 10 – 15 V. This is an expected behavior since the bias voltage favors the drift of photo-generated charge carriers towards the electrodes by enhancing their velocity. In such region the signal rise-time can be described as

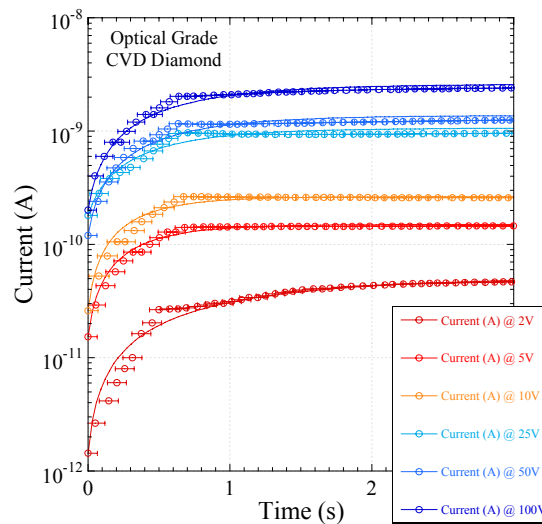$$\tau_{rt} \propto \tau_{Drift} = d^2/(\mu V). \tag{5.11}$$

Fig. 5. 16. Time-dependent signal evolution after a off-on radiation transition at different bias voltages.

For higher voltages, the device response becomes slower although the charge carriers velocity is expected to increase. It can be explained by supposing the formation of space charge regions, possibly caused by trapping performed by the deep defects present in OG samples. Space charge effects are favored by an increase of bias voltage, thus the Mott-Gurney model could be useful to explain the patterns trend. However, it is not able to fit sufficiently well the experimental curves.
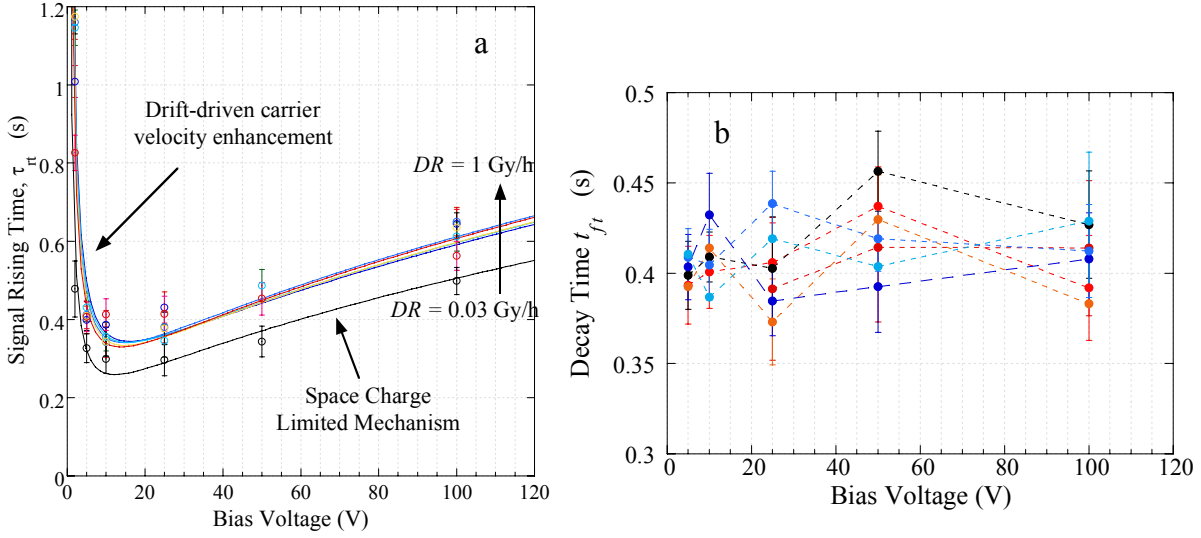

Fig. 5. 17. Signal a) rise-time and b) fall-time as a function of bias voltage.

The experimental patterns are thus fitted according to the linear superposition of Eq. (5.11) for low voltage and a phenomenological function of the type $\propto V_{bias}^{\gamma}$, where $\gamma < 1$ and has to be correlated in the future to a physical meaning. The τ_{rt} minimum value is around 285 ms for V_{Bias} in the range (10, 25) V, where the charge carriers are sufficiently fast and the charging effects are negligible. It is worth notice that the radiation switch-on is not ideal, since it is obtained by the activation of a mechanical shutter, characterized by a finite switching time (not measured). In other words, the excitation could be more similar to a trapezoidal function than a *rect* one. Consequently, the τ_{rt} values may be underestimated.

The signal decay time was measured by analyzing the on-off radiation transition. It represents an indication of how fast the device is able to return to the initial pre-irradiation conditions. It was observed that the τ_{ft} assumes a mean value of (0.41 ± 0.04) s, independently of bias voltage and of radiation dose-rate. The clear and reproducible trend of the signal rise-time on bias voltage is not repeated by the signal fall-time (Fig. 5. 17b).

Fig. 5. 18 points out the τ dependency on dose-rate. Signal rising time is a feeble increasing function of *DR* and, specifically, can be fitted by the power function $\tau \propto DR^{\alpha}$, with $\alpha << 1$ (close to 0.1).
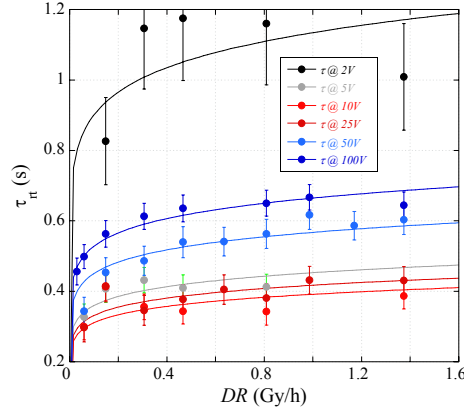

Fig. 5. 18

5.5 Specific Sensitivity.

We define the specific sensitivity δ as the ratio between photocurrent and *DR* per unit active volume *V*. Specific sensitivity is a very significant parameter that takes into account the capability of the dosimeter to generate a signal if irradiated by a defined x-ray dose-rate, fixed its active volume.

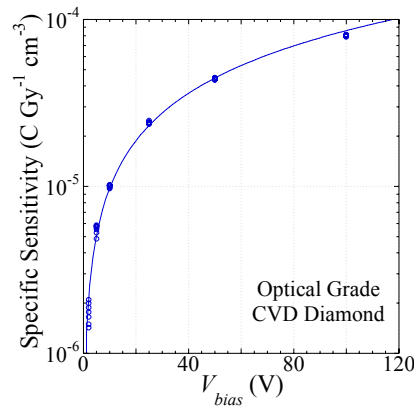OG dosimeters show specific sensitivity values of about 0.1 mC·Gy^{-1}·cm^{-3} at 100 V (Fig. 5. 19).

Fig. 5. 19

On the other hand, Fig. 5. 19 reports a study of the specific detector sensitivity as a function of V_{bias} under DC and AC irradiation for EG dosimeters. The DC specific sensitivity at 100 V is about

40 mC·Gy^{-1}·cm^{-3}, about 400 times that provided by OG dosimeters. At 400 V sensitivity is equal to (55.94 ± 0.21) mC·Gy^{-1}·cm^{-3}, corresponding to a far larger value than those obtained with radiotherapy sources [13], due to the prevalence of photoelectric effect for the charge production. DC sensitivity is slightly higher than the AC ones. To evaluate if this variation is due to a different collection efficiency of charge carriers, the patterns were fitted with an expression derived from Hecht's formula:

$$\delta \propto \frac{\mu\tau V_{bias}}{d^2}[1-\exp(-\frac{d^2}{\mu\tau V_{bias}})]$$ (5.12)

that gives an estimation of the charge carriers' mobility-lifetime product ($\mu\tau_{dc}$ and $\mu\tau_{ac}$, respectively).
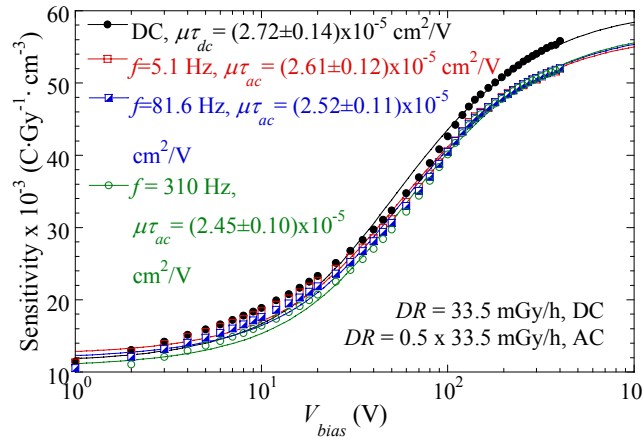

Fig. 5. 20. AC and DC sensitivity versus the applied bias.
Continuous curves refer to the fitting results with (5.12).

The estimated value of $\mu\tau_{dc}$ is (2.72 ± 0.14) × 10^{-5} cm^2/V, whereas $\mu\tau_{ac}$ is lesser than $\mu\tau_{dc}$, with a weak decreasing dependence on f (from (2.62 ± 0.12) × 10^{-5} to (2.45 ± 0.10) × 10^{-5} cm^2/V, at 5 and 300 Hz, respectively). This variation can be explained by a decrease in charge carriers' lifetime caused by the presence of shallow traps. Moreover Hecht's model significantly fits experimental data at high voltages, but it is not completely satisfactory to explain the detectors behavior at low voltages [8]. It is necessary a deeper analysis of the signal dependence on frequency.

5.6. Characterization by modulated irradiation (AC).

Modulated irradiation characterization has been performed by measuring the signal as a function of bias voltage, radiation dose-rate and modulation frequency f to extract the amount as high as possible of information about the dosimeters performance.

Fig. 5. 21 reports a typical $|I_{ph-ac}(V_{bias}, f)|$ characteristic under irradiation and the corresponding phase. Usually an increase of frequency induces a reduction of the signal module and phase owing to the limitation of detectors response capability. Such I-V characteristics are generally slightly asymmetrical coherently with the photocurrent signal obtained by DC irradiation conditions.
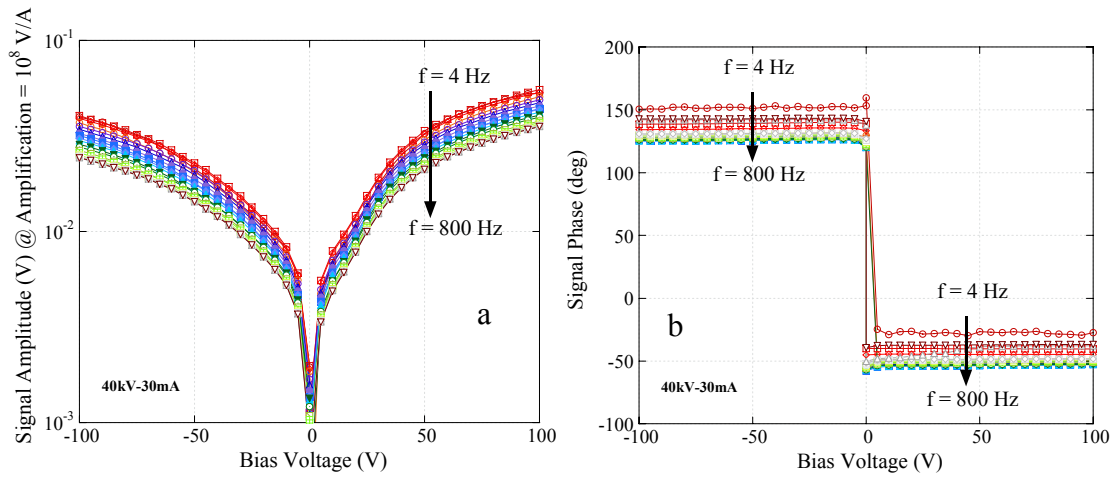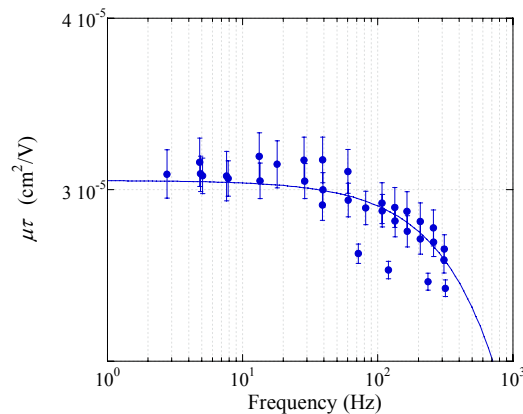
Fig. 5. 21

Fig. 5. 22

As described also in Paragraph 5.5, by applying Eq. (5.5) on $|I_{ph-ac}(V_{bias}, f)|$ it is possible to obtain the trend of the $\mu\tau$ product as a function of modulation frequency, shown in Fig. 5. 22. The

trend is linearly decreasing with frequency and it is compatible with the picture of shallow traps present within the crystal reducing the carriers lifetime as frequency increases [14]. The next paragraph will analyze in depth the effect of shallow traps on the signal dependence on frequency.

5.6.1 Frequency dependent signal.

Fig. 5. 23a reports a typical Bode plot of the normalized photocurrent as a function of V_{bias} at fixed dose-rate. The photocurrent trends are compatible with the presence of traps. We can distinguish three different regimes: at the lowest frequencies, signal is constant; at intermediate f the normalized photocurrents decrease according to a fast decay, possibly controlled by band-to-band recombination mechanisms and depending only on the lifetime of majority carriers; at highest f, it is apparent a slower decay, that can be attributed to a concurrent thermal emission of trapped charge carriers towards extended states.

These mechanisms are common to OG and EG dosimeters, with a difference in the behaviour driven by bias voltage.
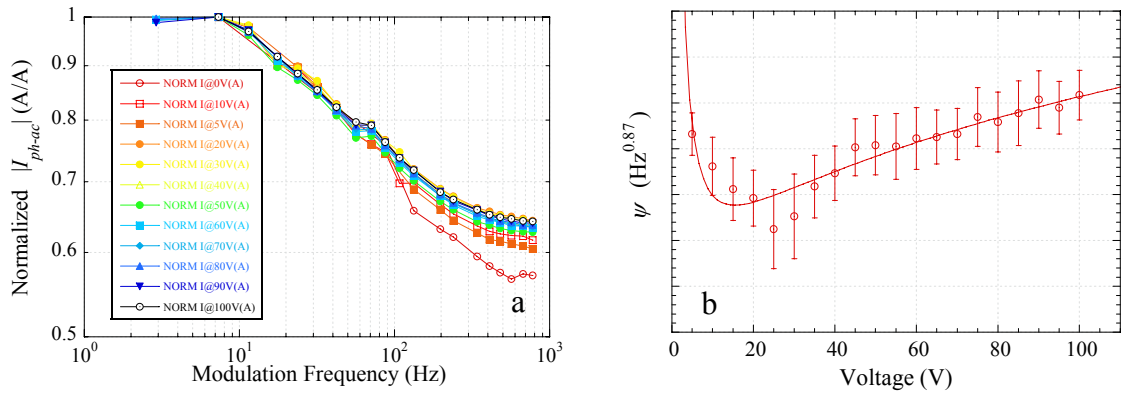

Fig. 5. 23

In OG samples, the signal is constant up to 10 Hz. After that, a dispersive regime arises. The intermediate frequency signal-dependence can be fitted with a function of the type $\propto \psi f^{-\alpha}$, where α is found to be constant and equal to 0.130 ± 0.005. Analyzing the values of ψ as a function of bias voltage, it is interesting to note that we obtain the trend depicted in Fig. 5. 23b, that gives similar qualitative indications compared to signal rise-time obtained by DC transient characterization (Fig. 5. 17b). The described parallel behaviour is currently under study.
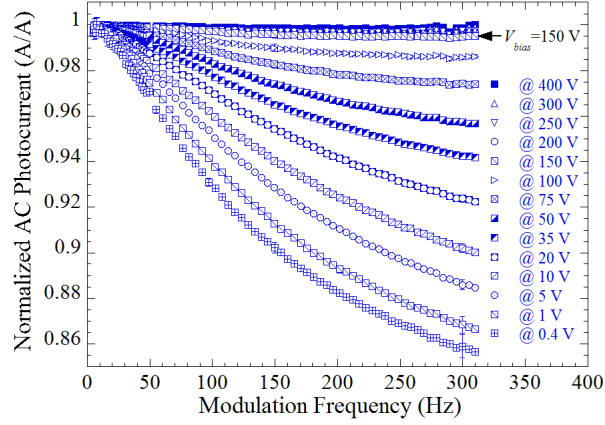
Fig. 5. 24. Normalized AC photocurrent frequency-dependence
as a function of the bias voltage for an EG dosimeter.

EG samples behaviour on frequency is quite similar to OG dosimeters, but with some differences regarding the effect of bias voltage. As shown in Fig. 5. 24, an increase of bias voltage progressively reduces the band-to-band recombination, possibly favouring fast thermal emission. This corresponds to a shifting of the limit between the two dispersive mechanisms to lower frequencies, until reaching a flat curve for $V_{bias} \geq 150$ V (electric field $\geq 3 \times 10^3$ V/cm). We hypothesize that some defect states in the DLC layer can account for this behaviour. Conversely, the injecting properties of the DLC layer seem to avoid space-charge effects affecting diamond devices, as the flat $I_{ph\text{-}ac}$ (f) curves up to 315 Hz demonstrate. They are indicative of millisecond-range response times (or less), confirmed by DC fast signal recording measurements of signal 10%-90% rise and fall times which were found smaller than the sampling rate ($\sim$ 8 ms) [8].

5.6.2 Signal phase shift analysis.

The signal phase shift under modulated irradiation can be used to obtain information from localized states in the bandgap of a semiconductor. The model that we intend to apply is based on the assumption that modulation frequency is able to probe trap defect states characterized by re-emission times comparable to f^1. This probing method can be used to obtain the distribution of the density of states of semiconductors presenting shallow traps. This method is the Oheda's model [15] and in this paragraph will be explained its application on signal module and phase provided by OG samples. A basic requirement of this model is that the excitation has to induce band-to-band carriers transitions, that can be after trapped. X-radiation satisfies such condition.
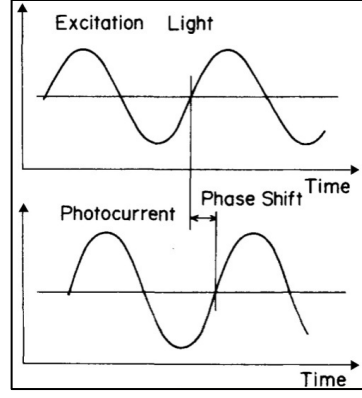
Fig. 5. 25

In the high-frequency regime, where photocurrent is mainly determined by the interaction of free carriers with localized states situated at the energy level $E\omega$, for which, as discussed, the emission time equals the period of the signal, Oheda's theory gives the following expression

$$N_t(E_\omega) = \frac{\mu}{v\sigma} \frac{2q}{\pi kT} \phi_{ac} \frac{F\,A}{I_{ph-ac}} \sin(\varphi),$$ (5.13)

where φ is the phase shift, ϕ_{ac} the modulated radiation flux, q is the elementary charge, μ the mobility, kT the thermal energy, F the electric field, A the area of the contacts, v and σ the saturation velocity and capture cross-section of carriers, respectively. Eq. (5.13) enables to obtain the density of defect states $N_t(E\omega)$ over the valence band maximum. The model assumes that

$$E - E_V = kT \ln(v_0 / \varpi)$$ (5.14)

being v_0 the attempt to escape frequency and E_V the valence band edge [16]. We do not know the absolute value of all the parameters playing a role, but we know that v_0 can be assumed equal to 10^{12} Hz and μ to 2×10^{-3} cm^2/(Vs) and we can evaluate a distribution proportional to $N_t(E\omega)$. The result is shown in

Fig. 5. 26. It is interesting to notice that the different curves, coming from the application of (5.13) to signal measured under conditions of different applied electric field, superpose each other.
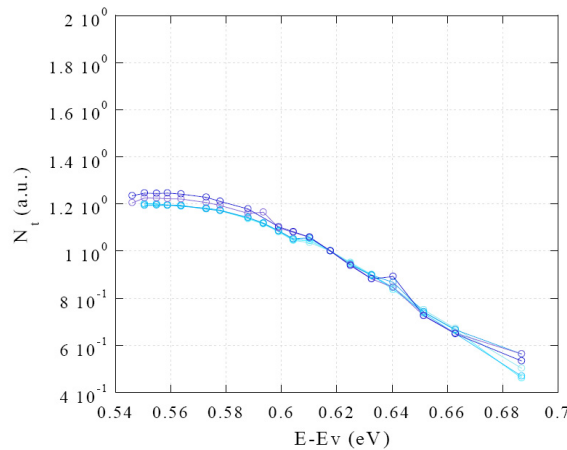

Fig. 5. 26

References.

1.	Sze, S.M., *Physics of Semiconductor Devices*. 2nd ed1981, New York: J.Wiley & Sons.
2.	G., C., et al., *Dielectric relaxation and space charge limited transport in polycrystalline CVD diamond* Diamond and Related Materials, 2005. **14**(3-7): p. 570-574.
3.	Kagan, H., *Recent advances in diamond detector development*. Nuclear Instruments and Methods in Physics Research Section A: Accelerators, Spectrometers, Detectors and Associated Equipment, 2005. **541**(1-2): p. 221-227.
4.	Rossi, M.C., et al., *Radiation-induced modification of trap occupancy in polycrystalline diamond detectors*. Diamond and Related Materials, 2003. **12**(3-7): p. 696-700.
5.	Bruzzi, M., *Diamond Radiation Sensors for Radiotherapy*, in *CVD Diamond for Electronic Devices and Sensors*, R.S. Sussman, Editor 2009, John Wiley & Sons Ltd.: London. p. 185-206.
6.	De Angelis, C., et al., *An investigation of the operating characteristics of two PTW diamond detectors in photon and electron beams*. Medical Physics, 2002. **29**(2): p. 248-254.
7.	Conte, G., et al., *Grain boundary transport in x-ray irradiated polycrystalline diamond*. Journal of Applied Physics, 2003. **93**(10): p. 6078.
8.	Trucchi, D.M., et al., *Very Fast and Priming-less Single-Crystal Diamond X-ray Dosimeters*. IEEE Electron Device Letters, Submitted.
9.	Zhao, S., *Characterization of the Electrical Properties of Polycrystalline Diamond Films*, 1994, The Ohio State University. p. 36-42 and Appendix B.
10.	Hecht, K., Zeitschrift Fur Phys., 1932. **77**: p. 235.
11.	Pan, L.S., et al., *Carrier Density Dependent Photoconductivity in Diamond*. Applied Physics Letters, 1990. **57**(6): p. 623-625.
12.	Fowler, J.F. and F.H. Attix, *Solid state electrical conductivity dosimeters*, in *Radiation dosimetry 2nd Edition*, F.H. Attix and W.C. Roesch, Editors. 1966, Academic Press: New York.
13.	Galbiati, A., et al., *Performance of Monocrystalline Diamond Radiation Detectors Fabricated Using TiW, Cr/Au and a Novel Ohmic DLC/Pt/Au Electrical Contact*. IEEE Transactions on Nuclear Science, 2009. **56**(4): p. 1863-1864.
14.	Kaplan, R., *Photoconductivity in a-SeTe*. Journal of Physics: Condensed Matter, 1995. **7**: p. 6847-6852.
15.	Oheda, H., *Phase-shift analysis of modulated photocurrent: its application to the determination of the energetic distribution of gap states*. Journal of Applied Physics, 1981. **52**(11): p. 6693-6700.
16.	Conte, G., et al., *Temporal response of CVD diamond detectors to modulated low energy X-ray beams*. physica status solidi (a), 2004. **201**(2): p. 249-252.

Conclusions

The developed single-crystal diamond x-ray dosimeters provide remarkable performances as radiation-sensitive devices. Referring to the requirements necessary for an ideal radiation dosimeter to be employed for medical applications, described at the beginning of this thesis, diamond dosimeters are intrinsically radiation damage resistant and tissue-equivalent. But tissue equivalency has to be guaranteed by the other dosimeter components: metal contacts, bonding wires, cables and detector enclosure. With the aim of perturbing as less as possible the correct response of the devices, a large effort has been devoted to the device structure design and selection of the most proper materials. The use of low-atomic-number metals, micrometer-size bonding wires, low-absorption-coefficient plastic materials and resins gives a clear evidence of the activity performed before and after dosimeters fabrication phase.

Ideal dosimeters have to provide a reproducible and stable response. The developed detectors show signal fluctuations less than 0.5%, signal reproducibility and stability. Moreover, the response generated by optical-grade dosimeters under irradiation is linear to x-ray dose-rate in a very large operative region. This region, individuated by the applied bias voltage, is more limited for electronic-grade samples. Moreover, dose-rate linearity implies linearity with dose, since the accumulated dose can be found by integrating the signal in time.

The dosimeters response is independent of photon energy of the impinging radiation, since comparable results have been observed by changing the spectral content of the source (i.e. by changing vacuum tube and/or by applying primary filters). Specific sensitivity values as high as 50 $mC \cdot Gy^{-1} \cdot cm^{-3}$ have been demonstrated by electronic-grade samples, which are further representative of their performance competitiveness.

Diamond dosimeters have a small size of some millimetres of lateral dimensions and half a millimetre of thickness. They are small if compared to ionization chambers. But in the future, taking advantage of the semiconductor technology and of their physical properties homogeneity, spatially-resolved detectors can be realized, arranged for example according to micrometer-size dots metallization.

Finally, we have to underline the remarkable transient performances of electronic-grade dosimeters, able to vary their response in concomitance of an irradiation intensity variation with times in the millisecond range. The dosimeters developed comply almost all the requirements with which this thesis has started.

Moreover, the comparative analysis among the different sample sets (electronic and optical-grade diamond films) has allowed a clarification of their physical properties that play a key-role in radiation detection. Although optical-grade dosimeters have some advantages as the cost and a wider response linearity to x-ray dose-rate, the electronic-grade dosimeters have demonstrated their superiority in terms of sensitivity, signal-to-leakage ratio, response promptness. Their cost of about 1 k€/film is practically the largest cost in fabricating dosimeters. Although the electronic-grade film cost is far larger than optical-grade one, it is smaller than comparable reference detectors for medical applications (both ionization chambers and silicon photodiodes have an approximate cost of 2 - 3 k€/piece). The natural diamond competitor is more expensive, being sold at about 5 k€/piece. This fortifies the conviction that the developed electronic-grade diamond x-ray dosimeters could be commercially competitive in a very near future.

List of Publications on ISI Journals

1. D.M. Trucchi, P. Allegrini, P. Calvani, A. Galbiati, K. Oliver, and G. Conte, "Very Fast and Priming-less Single-Crystal Diamond X-ray Dosimeters", submitted to IEEE Electron Device Letters.

2. S. Spadaro, D. M. Trucchi, G. Conte, M. Pimpinella, A. S. Guerra and R. F. Laitano, Sensors and Actuators A: Physical (2010).

3. P. Calvani, A. Corsaro, M. Girolami, F. Sinisi, D. M. Trucchi, M. C. Rossi, G. Conte, S. Carta, E. Giovine and S. Lavanga, Diamond and Related Materials **18** (5-8), 786-788 (2009).

4. B. Gorka, B. Nilsson, R. Svensson, A. Brahme, P. Ascarelli, D. Trucchi, G. Conte and R. Kalish, Physica Medica **24** (3), 159-168 (2008).

Other Publications during the PhD Thesis

5. D. M. Trucchi, E. Cappelli and P. Ascarelli, in *Sensors and Microsystems - Proceedings of the 13th Italian Conference*, edited by C. D. Natale, A. D'Amico, E. Martinelli and R. Paolesse (World Scientific, Rome, Italy, 2009), pp. 459-463.

6. D. M. Trucchi, A. Zanza, A. Bellucci, V. Marotta and S. Orlando, Thin Solid Films **518** (16), 4738-4742 (2010).

7. J. Alvarez Ruiz, A. Casu, M. Coreno, M. de Simone, L. M. Hoyos Campo, A. M. Juarez-Reyes, A. Kivimäki, S. Orlando, M. Sanz, C. Spezzani and D. M. Trucchi, Nuclear Instruments and Methods in Physics Research Section B: Beam Interactions with Materials and Atoms **268** (3-4), 425-429 (2010).

8. E. Cappelli, S. Orlando, D. M. Trucchi, A. Bellucci, V. Valentini, A. Mezzi and S. Kaciulis, Applied Surface Science (2010).

9. E. Cappelli, D. M. Trucchi, S. Kaciulis, S. Orlando, A. Zanza and A. Mezzi, Thin Solid Films (2011).

10. D. Caschera, P. Cossari, F. Federici, S. Kaciulis, A. Mezzi, G. Padeletti and D. Trucchi, Thin Solid Films (2011).